DUDLEY
NAVAL POSTGRADUATE SCHOOL
MONTEREY, CALIFORNIA 93943

NAVAL POSTGRADUATE SCHOOL
Monterey, California

THESIS

DIAGNOSTIC VERIFICATION OF THE GLAS GENERAL CIRCULATION MODEL AS APPLIED TO A CASE OF EXTRATROPICAL MARITIME EXPLOSIVE CYCLOGENESIS

by

Kenneth A. Ebersole

December 1984

Thesis Advisor: Carlyle H. Wash

Approved for public release; distribution unlimited

T220201

UNCLASSIFIED

SECURITY CLASSIFICATION OF THIS PAGE (When Data Entered)

REPORT DOCUMENTATION PAGE		READ INSTRUCTIONS BEFORE COMPLETING FORM
1. REPORT NUMBER	2. GOVT ACCESSION NO.	3. RECIPIENT'S CATALOG NUMBER
4. TITLE (and Subtitle) Diagnostic Verification of the GLAS General Circulation Model as Applied to a Case of Extratropical Maritime Explosive Cyclogenesis		5. TYPE OF REPORT & PERIOD COVERED Master's Thesis December 1984
		6. PERFORMING ORG. REPORT NUMBER
7. AUTHOR(s) Kenneth A. Ebersole		8. CONTRACT OR GRANT NUMBER(s)
9. PERFORMING ORGANIZATION NAME AND ADDRESS Naval Postgraduate School Monterey, California 93943		10. PROGRAM ELEMENT, PROJECT, TASK AREA & WORK UNIT NUMBERS
11. CONTROLLING OFFICE NAME AND ADDRESS Naval Postgraduate School Monterey, California 93943		12. REPORT DATE December 1984
		13. NUMBER OF PAGES 112
14. MONITORING AGENCY NAME & ADDRESS(if different from Controlling Office)		15. SECURITY CLASS. (of this report) Unclassified
		15a. DECLASSIFICATION/DOWNGRADING SCHEDULE

16. DISTRIBUTION STATEMENT (of this Report)

Approved for public release; distribution unlimited

17. DISTRIBUTION STATEMENT (of the abstract entered in Block 20, if different from Report)

18. SUPPLEMENTARY NOTES

19. KEY WORDS (Continue on reverse side if necessary and identify by block number)

GLAS Model Verification, Quasi-Lagrangian Diagnostics, Explosive Maritime Cyclogenesis, FGGE Year, Mass Budget Analysis, Vorticity Budget Analysis, SAT/NOSAT Comparisons

20. ABSTRACT (Continue on reverse side if necessary and identify by block number)

The general circulation model from the Goddard Laboratory for Atmospheric Sciences (GLAS) is verified for a case of explosive extratropical cyclogenesis in the North Pacific. Model runs are initialized with GLAS analyses based on the First GARP Global Experiment (FGGE) Level III-b data. Mass and vorticity budget studies are performed on two separate sets of forecasts. One set (SAT) was initialized with all available FGGE data, while the

DD FORM 1 JAN 73 1473 EDITION OF 1 NOV 65 IS OBSOLETE S/N 0102-LF-014-6601

UNCLASSIFIED

SECURITY CLASSIFICATION OF THIS PAGE (When Data Entered)

#20 - ABSTRACT - (CONTINUED)

other (NOSAT) was initialized with all FGGE data except satellite data.

Explosive development occurs in conjunction with zonal mid-level flow and strong jet streak interaction. The inclusion of underestimated satellite winds in the SAT initial field weakened the intensity of the jet stream and adversely affected the forecasts. The NOSAT run indicated greater surface convergence, divergence aloft, vertical motion and PVA than the SAT run. The NOSAT prognoses developed and positioned the storm more accurately than the SAT prognoses.

Approved for public release; distribution unlimited.

Diagnostic Verification of the GLAS General Circulation Model as Applied to a Case of Extratropical Maritime Explosive Cyclogenesis

by

Kenneth A. Ebersole
Lieutenant Commander, United States Navy
B.S., United States Naval Academy, 1976

Submitted in partial fulfillment of the
requirements for the degree of

MASTER OF SCIENCE IN METEOROLOGY AND OCEANOGRAPHY

from the

NAVAL POSTGRADUATE SCHOOL

December 1984

DUDLEY KNOX LIBRARY
NAVAL POSTGRADUATE SCHOOL
MONTEREY, CALIFORNIA 93943

ABSTRACT

The general circulation model from the Goddard Laboratory for Atmospheric Sciences (GLAS) is verified for a case of explosive extratropical cyclogenesis in the North Pacific. Model runs are initialized with GLAS analyses based on the First GARP Global Experiment (FGGE) Level III-b data. Mass and vorticity budget studies are performed on two separate sets of forecasts. One set (SAT) was initialized with all available FGGE data, while the other (NOSAT) was initialized with all FGGE data except satellite data.

Explosive development occurs in conjunction with zonal mid-level flow and strong jet streak interaction. The inclusion of underestimated satellite winds in the SAT initial field weakened the intensity of the jet stream and adversely affected the forecasts. The NOSAT run indicated greater surface convergence, divergence aloft, vertical motion and PVA than the SAT run. The NOSAT prognoses developed and positioned the storm more accurately than the SAT prognoses.

DUDLEY KNOX LIBRARY
NAVAL POSTGRADUATE SCHOOL
MONTEREY, CALIFORNIA 93943

TABLE OF CONTENTS

I. INTRODUCTION ---------- 12

II. SYNOPTIC DISCUSSION ---------- 15

A. GENERAL ---------- 15

B. ANALYSIS INTERCOMPARISONS ---------- 15

C. GLAS PROGNOSES VERIFICATION ---------- 20

D. SUMMARY OF SAT/NOSAT DIFFERENCES ---------- 25

III. MASS BUDGET ANALYSIS ---------- 28

A. GENERAL ---------- 28

B. POTENTIAL TEMPERATURE AND STABILITY ANALYSIS - 29

C. VERTICAL MASS TRANSPORT ---------- 32

D. HORIZONTAL MASS FLUX ---------- 33

E. CONCLUSIONS ---------- 35

IV. VORTICITY BUDGET ANALYSIS ---------- 37

A. GENERAL ---------- 37

B. VORTICITY TENDENCIES ---------- 38

C. LATERAL TRANSPORT ---------- 40

D. LATERAL DIVERGENCE COMPONENT ---------- 41

E. LATERAL ADVECTION COMPONENT ---------- 42

F. VERTICAL REDISTRIBUTION ---------- 43

G. SOURCES AND SINKS ---------- 44

H. RESIDUALS ---------- 45

I. CONCLUSIONS ---------- 47

V. CONCLUSIONS AND RECOMMENDATIONS ---------- 49

APPENDIX A: FGGE DATA ---------- 52

APPENDIX B: TABLES ---------- 55

APPENDIX C: FIGURES ---------- 60

LIST OF REFERENCES ---------- 109

INITIAL DISTRIBUTION LIST ---------- 111

LIST OF TABLES

I. Generalized QLD Budget Equation in Isobaric Coordinates ---------- 55

II. QLD Mass Budget Equations in Isobaric Coordinates ---------- 57

III. QLD Circulation Budget Equations in Isobaric Coordinates ---------- 58

LIST OF FIGURES

1. Storm Track Positions and Central SLP at 12-h Synoptic Times ---------- 60

2. Synoptic Fields for GLAS Analysis at 00 GMT 12 January 1979 ---------- 61

3. As in Figure 2 except for GLAS Analysis 00 GMT 13 January ---------- 62

4. As in Figure 2 except for GLAS Analysis 00 GMT 14 January ---------- 63

5. As in Figure 2 except for GLAS Analysis 12 GMT 14 January ---------- 64

6. As in Figure 2 except for NOSAT Prognosis 00 GMT 13 January ---------- 65

7. As in Figure 2 except for GLAS Analysis 12 GMT 13 January ---------- 66

8. As in Figure 2 except for SAT Prognosis 12 GMT 13 January ---------- 67

9. As in Figure 2 except for NOSAT Prognosis 12 GMT 13 January ---------- 68

10. As in Figure 2 except for SAT Prognosis 00 GMT 14 January ---------- 69

11. As in Figure 2 except for NOSAT Prognosis 00 GMT 14 January ---------- 70

12. As in Figure 2 except for SAT Prognosis 12 GMT 14 January ---------- 71

13. As in Figure 2 except for NOSAT Prognosis 12 GMT 14 January ---------- 72

14. As in Figure 2 except for GLAS Analysis 12 GMT 14 January ---------- 73

15. As in Figure 2 except for SAT Prognosis 00 GMT 15 January ---------- 74

16. As in Figure 2 except for NOSAT Prognosis 00 GMT 15 January ---------- 75

17. As in Figure 2 except for GLAS Analysis 12 GMT 15 January ---------- 76

18. As in Figure 2 except for SAT Prognosis 12 GMT 15 January ---------- 77

19. As in Figure 2 except for NOSAT Prognosis 12 GMT 15 January ---------- 78

20. As in Figure 2 except for GLAS Analysis 00 GMT 16 January ---------- 79

21. As in Figure 2 except for SAT Prognosis 00 GMT 16 January ---------- 80

22. As in Figure 2 except for NOSAT Prognosis 00 GMT 16 January ---------- 81

23. NOSAT-SAT 250 mb Isotach Difference (Dashed) in m/s Superposed on Observed Wind Reports for 00 GMT 13 January ---------- 82

24. Analyses Grids Superposed over Radius 6 and 10 Degree Budget Volumes ---------- 83

25. Analyses Area-Averaged Potential Temperature Time Sections ---------- 84

26. Stability Index ---------- 85

27. Prognoses Area-Averaged Potential Temperature Time Sections ---------- 86

28. Analyses Kinematic Vertical Velocities ---------- 87

29. Prognoses Kinematic Vertical Velocities ---------- 88

30. Analyses Corrected Lateral Mass Transport Time Sections ---------- 89

31. Prognoses Corrected Lateral Mass Transport Time Sections ---------- 90

32. Analyses Area-Averaged Absolute Vorticity Vertical Time Sections ---------- 91

33. Prognoses Area-Averaged Absolute Vorticity Vertical Time Sections ---------- 92

34. Analyses Absolute Vorticity Vertical Time-Tendency Sections ---------- 93

35. Prognoses Absolute Vorticity Vertical Time-Tendency Sections ---------- 94

36. Analyses Lateral Vorticity Transport ---------- 95

37. Prognoses Lateral Vorticity Transport ---------- 96

38. Analyses Lateral Vorticity Divergence ---------- 97

39. Prognoses Lateral Vorticity Divergence ---------- 98

40. Analyses Lateral Vorticity Advection ---------- 99

41. Prognoses Lateral Vorticity Advection ---------- 100

42. Analyses Vertical Advection of Vorticity ---------- 101

43. Prognoses Vertical Advection of Vorticity ---------- 102

44. Analyses Tilting Term ---------- 103

45. Prognoses Tilting Term ---------- 104

46. Analyses Frictional Dissipation ---------- 105

47. Prognoses Frictional Dissipation ---------- 106

48. Analyses Budget Residuals ---------- 107

49. Prognoses Budget Residuals ---------- 108

ACKNOWLEDGEMENTS

Many thanks are extended to Jim Peak for his tireless aid with computer routines. The objective and critical review of this thesis by Dr. R. L. Elsberry is greatly appreciated. A special thank you to Dr. C.H. Wash for his extensive guidance, insight, and encouragement during this study. As with all I have done, grateful thanks go to my parents for their love and moral support. Finally, my thanks to Mark Twain who helped me keep my perspective when I recalled the quote: "I have never let my schooling interfere with my education."

I. INTRODUCTION

Current numerical models have difficulty forecasting cases of rapidly developing extratropical maritime cyclones. Explosive cyclogenesis has been characterized by Sanders and Gyakum (1980) as a central surface pressure fall of at least 1 mb/h for 24 h (normalized with respect to 60 degrees latitude). These systems present considerable potential danger to shipping and fixed ocean platforms. The combined effects of high winds, heavy seas and reduced visibility developing over short time periods have caused substantial property damage, injury and loss of life. The loss of the Russian trawler Metrostoy [Mariner's Weather Log, 1979] and the sinking of the oil rig Ocean Ranger [Lemoyne, 1982] are dramatic examples of the destructive nature of such rapidly developing systems.

Major sources of error in numerical models include data gaps or errors, poor initialization, truncation errors and inaccurate model physics [Haltiner and Williams, 1980]. While all four error sources are potentially important in modeling explosive maritime cyclones, the limited amount of data available over the ocean certainly is one of the most significant. Satellite systems have helped to fill gaps, and the impact of these data on forecasts is a major thrust of current research. Additionally, the temporal and spatial

scales of these systems are smaller than the scales for which some of the models were designed, which results in poor resolution of storm features. The comparison of two analyses of different resolution can illustrate the importance of analyses differences. Finally, the role of convective processes in the development of explosive maritime cyclones is considerable. Errors in convective cumulus parameterization in a model will adversely affect a forecast.

This study will concentrate on a case of explosive maritime cyclogenesis over the North Pacific during the period of 13-16 January 1979. Calland (1983) used analyses by the European Center for Medium-range Weather Forecasts (ECMWF) based on data collected during the First GARP (Global Atmospheric Research Program) Global Experiment (FGGE) to investigate this system. Other analyses available during the FGGE period include the Geophysics Fluid Dynamics Laboratory (GFDL) analyses and the Goddard Laboratory for Atmospheric Sciences (GLAS) analyses. In this thesis, the GLAS analysis with its different resolution and initialization scheme will be examined. Additionally, two GLAS model forecasts will be verified. One set (SAT) of prognoses was initialized with all available FGGE data, while the other (NOSAT) was initialized with all FGGE data except satellite data. The main objectives of this thesis are:

- Diagnostic study of a case of explosive maritime cyclogenesis using GLAS analyses;
- Diagnostic verification of a global forecast model for a case of explosive maritime cyclogenesis;

- Assessment of the impact of satellite data on the model performance.

The diagnostic approach in this thesis is similar to that of Calland (1983). GLAS analyses and model prognoses are used to examine mass and circulation (vorticity) budgets for the system. Quasi-Lagrangian diagnostics (QLD) as developed by Johnson and Downey (1975) are used to conduct the budget studies. The budget volume is defined by a cylindrical coordinate system which is centered on the cyclone surface center at each time. The advantage of this technique is that it focuses on those processes related directly to cyclone development. Verification of the GLAS prognoses is achieved by comparing both the basic fields and budget statistics to those from the GLAS and ECMWF analyses.

Appendix A is a discussion of the FGGE level II-b and level III-b data. Chapter II describes the results of the synoptic diagnostic studies performed on the GLAS analyses and model predictions and compares them with the results of Calland (1983). Chapters III and IV explore the results of the cyclone mass and vorticity budget studies with comparison to Calland (1983). Chapter V summarizes the thesis conclusions and includes recommendations for future studies.

II. SYNOPTIC DISCUSSION

A. GENERAL

Two FGGE analyses and two prognoses are compared for the 13-16 January 1979 North Pacific storm. The two analyses are made by the ECMWF and by the GLAS. Both analyses are based on FGGE level II-b data. The two GLAS prognoses are from a GLAS analysis which included all available FGGE data (SAT) and from a separate analysis that excluded satellite data (NOSAT). Intercomparison of the GLAS and ECMWF analyses will illustrate the impact of differences due to horizontal resolution and different objective analysis schemes in portraying explosive maritime systems. The comparison of the two GLAS prognoses with each analysis produces a qualitative evaluation of model performance with different data sets. Finally, intercomparison of the SAT and NOSAT prognoses assesses the importance of satellite data in producing a better forecast. The evaluation will focus on the surface, 500 mb and 250 mb features.

B. ANALYSIS INTERCOMPARISONS

While both the ECMWF and GLAS analyses are based on FGGE level II-b data, substantial differences exist between the schemes used to produce the level III-b analyses. The ECMWF data assimilation system is a three-dimensional, multivariate, optimal interpolation scheme using a nonlinear normal-mode

initialization. A 15-level model with horizontal resolution of 1.875 degrees of latitude and longitude is used in the update cycle.

The GLAS objective analysis uses a modified Cressman (successive correction) scheme based on a method by Bergthorsson and Doos (1955). The assimilation/forecast model consists of nine vertical levels in sigma coordinates with a uniform non-staggered grid (4 degrees latitude by 5 degrees longitude). Details of the GLAS FGGE level III-b analysis can be found in Appendix A.

The storm tracks for the GLAS analysis, SAT and NOSAT prognoses are depicted in Fig. 1. Figures appear in Appendix C. The reader should consult Calland (1983) to observe similar figures for the ECMWF analysis, as they will not be repeated in this thesis. Figure numbers ascribed to the ECMWF analysis in the foregoing discussion refer to the figures in Calland (1983). A comparison of the central surface pressures of the two analyses reveals agreement to within 1 mb with the exception of 12 GMT 14 January when the ECMWF analysis is 4 mb deeper than the GLAS analysis. Storm positions of the two analyses are consistent throughout the 72-h period, so only the storm track from the GLAS analyses is shown in Fig. 1.

At 00 GMT 12 January atmospheric conditions southeast of Japan are favorable for frontogenesis. The GLAS analysis sea-level pressure (SLP) (Fig. 2c) contains a broad trough

extending northeast-southwest (vicinity of 35 N, 150 E) within a checkerboard pattern of strong cyclone and anticyclone features. The major circulation centers include the Siberian high near 55 N, 100 E (off the chart), a filling low (952 mb) at 53 N, 170 E, a large maritime high (1030 mb) centered over the north-central Pacific (vicinity of 30 N, 178 W), and Typhoon Alice at 14 N, 138 E. The ECMWF surface analysis (Fig. 4c, Calland) indicates similar features. This circulation funnels cold, polar continental air southward over the northwestern Pacific toward the northward flowing warm, moist tropical air, which enhances the polar front southeast of Japan.

By 00 GMT 13 January, a closed surface circulation is observed in both analyses (Fig. 3c and Fig. 7c, Calland). The positions and intensities of the central surface pressure in the two analyses are in close agreement. Likewise, the thermal fields over the cyclone are similar. Both analyses indicate a shallow 500 mb trough west of the surface low at about 135 E. The ECMWF vorticity field (Fig. 7b, Calland) shows a maximum associated with the trough as expected. However, the GLAS vorticity field (Fig. 3b) has a smaller maximum. Throughout the life of the cyclone, the horizontal resolution of the GLAS 500 mb vorticity analyses appear to produce excessive smoothing with more symmetrical maxima than those seen in the ECMWF analysis. The consequences of this difference are explored in the discussion of the vorticity

budget results. The two 250 analyses are similar, and both indicate a jet streak poleward and somewhat west of the surface low.

At 00 GMT 14 January, there are virtually no differences between the analyses in the position and intensity of the central surface pressure. The GLAS analysis thickness ridge (Fig. 4c) remains stronger than on the ECMWF analysis (Fig. 10c, Calland). The 500 mb analyses are similar, although the GLAS analysis (Fig. 4b) has not resolved the vorticity maximum migrating toward the system. The positive vorticity advection is well represented on the ECMWF analysis (Fig. 10b, Calland). At 250 mb, the jet maxima is now positioned to the southwest of the surface low in both analyses, which creates favorable conditions for strong upper-level divergence and explosive development.

By 12 GMT 14 January, a larger difference in the two surface pressure analyses is present. The ECMWF analysis (Fig. 16c, Calland) places the central pressure at 965 mb, and the GLAS analysis (Fig. 5c) has 969 mb. This is the first period of rapid deepening of the system, and the GLAS analysis presumably suffers from limited data near the storm center and an inability to describe the central feature with the coarse resolution. Examination of the level II-b data available to the GLAS analysis reveals that there are only two surface pressure reports (ship) within 5 degrees latitude of the storm center. A 500 mb trough just to the west

of the surface center is similarly represented in the two analyses (Figs. 5b and 16b, Calland), which indicates the self-development of the storm during the prior 12 h. Cyclonic flow in the middle troposphere GLAS vorticity field (Fig. 5b) indicates a maximum over the surface low, as does the ECMWF analysis (Fig. 16b, Calland). Due to coarser resolution, the GLAS vorticity maxima are not as large, and are generally more circular than those in the ECMWF analysis. The jet axis is now well south of the surface low, and the upper-air flow is similar in both analyses.

Between 00 GMT 15 January and 16 January, the cyclone is in the occlusion phase of development. The fields of the two analyses are similar with the exception of the vorticity maxima already described.

The overall comparison of the GLAS and ECMWF analyses shows close agreement. The translation of the storm is very similar throughout the three-day period and, with minor exceptions, the intensities of the surface low centers are similar. The decreased resolution of the GLAS analysis is most evident in the vorticity field, where the maxima are either not resolved or oddly shaped. The upper troposphere winds are very similar throughout the period in the two analyses. In summary, the GLAS analysis performs well on this system considering its coarser resolution and less complex objective analysis scheme.

Another comparison of the ECMWF and GLAS analyses for January 1979 by Baker (1983) revealed generally close agreement.

The positions of the low centers were very similar. The major difference in that comparison was that the ECMWF analysis depicted a central surface pressure 5 mb lower than the GLAS analysis on 19 January. This difference was attributed to the coarser grid used by the GLAS model.

C. GLAS PROGNOSES VERIFICATION

The GLAS prognoses with all available data (SAT) and the GLAS prognosis with all except satellite data (NOSAT) are verified using the GLAS analyses discussed above. Central surface pressure in 12-h increments and the storm tracks appear in Fig. 1. It was expected that the SAT prognoses would outperform the NOSAT prognoses. As can be seen in Fig. 1, this is not necessarily true. The storm track in the SAT prognosis during the period of 13-16 January is considerably farther from the analysis track than the NOSAT prognosis. The SAT prognosis did forecast storm intensity more accurately than the NOSAT prognosis in the early periods, but after the 00 GMT 15 January the SAT prognoses are worse than NOSAT both in position and intensity.

The SAT prognosis starts with the GLAS analysis at 00 GMT 13 January (Fig. 3). Noteworthy differences in the initial analysis for the NOSAT model are seen in the 250 mb flow (Fig. 6a), as the removal of the satellite sounding and cloud-drift wind data has altered the intensity of the jet stream. The 250 mb jet streak at 140 E on the NOSAT initial analysis extends farther eastward than the SAT jet streak

(Fig. 3a), and winds east of the incipient region are 10-20 m/s larger in the NOSAT analysis.

After only 12 hours, noticeable differences develop among the SAT and NOSAT forecasts and the analysis. The surface pressure of the cyclone depicted in the SAT prognosis has been overdeepened by 3 mb. The storm has tracked more northeastward than eastward as on the analysis, and is 130 km away from the analysis center (Fig. 1). The NOSAT prognosis has likewise overdeepened the system by 4 mb. However, the position error of the NOSAT prognosis is less than 80 km. Consistent with the overdevelopment, the 1000-500 mb thickness ridge of both prognoses is greater than the analysis (Figs. 7c, 8c and 9c).

A large difference is observed at this time period in the 250 mb jet stream. The NOSAT prognosis 250 mb wind field (Fig. 9a) shows the 75 m/s jet streak extending farther eastward than on the analysis (Fig. 7a). Consequently, the surface low is already positioned under the front left quadrant of the jet streak. The SAT prognosis 250 mb winds (Fig. 8a) are 10-20% weaker than the analysis.

At 00 GMT 14 January, the storm in the SAT prognosis (Fig. 10c) has continued to overdevelop and is now 6 mb deeper than the analysis (Fig. 1). Movement during the period is similar to the previous period and the storm has a 370 km position error. The NOSAT prognosis (Fig. 11c) also overdevelops the system with a 14 mb difference in central surface pressure, but has only a 120 km position

error. The thermal ridges in each prognosis continue to be stronger than the analyses, which is consistent with the more advanced stage of development. Consistent with the thermal ridges, 500 mb flow above the surface low appears to be more cyclonic in the prognoses than in the analyses. However, 500 mb absolute vorticity differences at this time are minimal (Figs. 4b, 10b and 11b). Smaller magnitudes are still observed in the SAT jet stream velocity (Fig. 10a); however, the difference does not appear to be as great as in the previous period.

In the 12-h period ending 12 GMT 14 January, the three storm tracks are generally parallel with similar displacements (Fig. 1). Overdevelopment continues at a consistent rate and the SAT storm is 10 mb deeper than the analysis. Development in the NOSAT prognosis slows as the storm enters the occlusion phase. Nevertheless, the NOSAT surface central pressure is 16 mb deeper than the analysis. The SAT and NOSAT thickness fields and 500 mb flow (Figs. 12 and 13) continue to indicate a more advanced stage of development than in the analysis storm (Fig. 5).

The 500 mb analysis contains a short wave trough trailing behind the surface low and a thermal trough behind the short wave, which suggests continued development of the system (Fig. 5b). Both the SAT (Fig. 12b) and NOSAT prognoses (Fig. 13b) indicate a 500 mb trough situated over the surface low which signifies self-development

during the prior 12 h. Also, the SAT and NOSAT prognoses have similar thickness ridges (Figs. 12c and 13c). Each prognosis indicates a warm air sector wrapping around the system center, which is consistent with the onset of occlusion.

The 250 mb jet stream of the SAT prognosis (Fig. 12a) is now much more similar to the analysis (Fig. 5a) than in previous periods, particularly in the jet streak southwest of the storm. The NOSAT prognosis 250 mb flow (Fig. 13a) differs somewhat from the analysis (Fig. 5a). Flow is of similar mangitude but is less cyclonic over the surface center in the prognosis. As the storm continues to move northeastward, the influence of the jet on development is diminished considerably after this period.

The period ending at 00 GMT 15 January is noteworthy because the observed storm (Fig. 14) continues to develop rapidly, while in the SAT and NOSAT prognoses (Figs. 15 and 16) the storm proceeds into the occlusion phase. Observed development is so intense that the large differences between the prognoses and the analyzed surface pressure is diminished considerably. The analyzed storm center moves twice as far as in either prognosis and increases the distances between low centers to 692 km (SAT) and 563 km (NOSAT) (Fig. 1). The 500 mb analysis (Fig. 14b) shows greater cyclonic curvature than in the prognoses (Figs. 15b and 16b). A major reason for the difference in storm translation between the

analyses and the prognoses is due to the position of the surface low relative to the jet stream. The analyzed low remains centered on the jet axis, while the low positions depicted in the prognoses are north of the jet axis, out of the baroclinic zone and into the colder air.

By 12 GMT 15 January all three representations of the storm are in the occlusion phase of development. The SAT (Fig. 18c) and NOSAT (Fig. 19c) storms are 8 and 7 mb, respectively, deeper than in the analysis (Fig. 17c). The central surface pressure in the analysis remains nearly the same as in the preceding period, while the surface pressure has dropped 11 mb and 5 mb in the SAT (Fig. 18c) and NOSAT (Fig. 19c) prognoses. This is unexpected inasmuch as the storm in both prognoses had occluded earlier than in the analysis. Closed circulations are observed at 500 mb in all three representations. The relative stages of occlusion are evident in the areal extent of the closed circulation, as the center in the analysis (Fig. 17b) is smaller than in either of the prognosis 500 mb centers (Figs. 18b and 19b). Highly cyclonic flow is even seen to a great extent at 250 mb in each prognosis (Figs. 18a and 19a).

By 00 GMT 16 January, the storm in both of the prognoses and in the analysis has begun filling. The analyzed storm is now over the Alaskan coast, and the biggest difference between the analysis and the prognoses is in the thickness fields (Figs. 20c, 21c and 22c). Warm air does not wrap

around the analysis storm as in the two prognoses. Apart from the position of the surface centers (Fig. 1), no other significant differences are noted for this final analysis period.

D. SUMMARY OF SAT/NOSAT DIFFERENCES

In the early stages of development, the principal difference observed between the two prognoses is the weaker jet stream winds in the SAT prognosis. One effect is to translate the system less accurately (Figs. 8a and 9a). The level II-b cloud-drift winds computed by the Meteorological Satellite Center (MSC) in Japan were found to contain substantial errors due to invalid altitude assignments [McPherson, 1984]. Upper-level winds were corrected at GLAS prior to assimilation of the level III-b data (see Appendix A). Nevertheless, errors in the corrected cloud-drift winds were large enough to decrease the jet intensity and to cause the SAT prognosis to translate the storm more slowly than the NOSAT prognosis. A difference plot (NOSAT-SAT) of jet stream winds at 00 GMT 13 January is depicted in Fig. 23. The largest difference between the two prognoses (20 m/s) coincides with several cloud-drift wind reports that are approximately 25 m/s (50 kt) slower than surrounding aircraft reports. Once the system moves north of the jet axis (about 12 GMT 14 January), the SAT prognosis translates the storm at much the same rate as the NOSAT (Fig. 1). This is

consistent with the observation that the large differences in the 250 mb flow are limited primarily to the jet stream.

For the majority of the 72-h period, the two prognoses develop the storm similarly in terms of intensity. Over-development of the storm is forecast during the first 36 h, especially in the NOSAT prognosis. In the latter stages of development and occlusion, the positions in the two prognoses become closer, but the intensities vary considerably as the SAT prognosis deepens appreciably while NOSAT deepening slows between 00-12 GMT 15 January. Meanwhile, the analyzed storm continues to deepen and translate well to the northeast of both prognoses (Fig. 1).

In summary, both prognoses initially overdevelop an already rapidly developing system. Because of this initial overdevelopment, both prognoses occlude too soon and stall over the Aleutian Island chain. The inital impression is that the presence or omission of upper tropospheric satellite winds does have a considerable effect on model performance. The fact that neither prognosis accurately forecasts the storm, however, indicates that the presence or absence of satellite data is not the sole contributor to the forecast errors.

The performance of operational forecast models in this case was quite different than that of the GLAS FGGE prognoses. Prognoses from the Fleet Numerical Oceanography Center (FNOC) underdeveloped the storm, rather than overdeveloping it like the GLAS model. Position errors for the FNOC

prognoses in the early periods were as large as 900 km. The GLAS FGGE prognoses performed well in comparison with the FNOC prognoses, particularly in the first 48 h. The impact of the comprehensive FGGE data was positive in the forecasting of this storm.

III. MASS BUDGET ANALYSIS

A. GENERAL

One of the key observations in the synoptic discussion (Chapter II) is the largely zonal mid-tropospheric flow over the incipient region in the early stages of development. Without a mid-level trough to explain cyclogenesis, other forcing mechanisms must be explored. Because of the large baroclinity over the incipient region, destabilization of the surface layer may explain the early stages of storm development. Additionally, evaluation of the horizontal and vertical mass circulation can substantiate the qualitative observations made in Chapter II, since storm intensity and pressure tendencies are directly related to the mass flux into and out of the budget volume.

This chapter quantitatively evaluates the destabilization and horizontal and vertical mass transport within the budget volume. The generalized quasi-Lagrangian budget equation and the QLD mass budget equation are included as Tables I and II. Initially, budget results were analyzed for two budget volumes: one with a 6 degree radius (666 km) and one with a 10 degree radius (1111 km). The purpose of studying the two volumes is to investigate the large-scale storm circulation and mass transport (radius 10) and the more intense processes closer to the storm center (radius 6)

[Calland, 1983]. The grid-size difference between the GLAS and ECMWF analyses is depicted in Fig. 24. The radius 6 budget results for the GLAS 4 × 5 degree grid contain many inconsistencies due to the grid size. Consequently, this study will focus on the radius 10 budget results for both the mass and vorticity study. As in the previous chapter, four data sets are examined. The GLAS analysis is first compared with the ECMWF analysis as described by Calland (1983), and then the GLAS analysis is used as a basis for comparison of the SAT and NOSAT storms.

B. POTENTIAL TEMPERATURE AND STABILITY ANALYSIS

As discussed in Chapter II, the storm development occurred within a large-scale flow of polar continental air around an intense Siberian high that extended over the warmer west North Pacific. These conditions produce a destabilization of the boundary layer over the incipient storm region, which is a key element in maritime cyclogenesis as described by Roman (1981) and Sandgathe (1981). The amount of destabilization in the surface layer depends on both latent and sensible heat flux from the ocean, which in turn is largely dependent on air-sea temperature difference.

Comparison of the radius 10 ECMWF analysis area-averaged potential temperature (Fig. 25b) with that of the GLAS analysis (Fig. 25a) reveals that mid-tropospheric temperatures of the ECMWF analysis are generally several degrees higher than the GLAS analysis. Over the 72-h period, 500 mb temperatures

of the ECMWF analysis decrease from 311 K to 294 K and in the GLAS analysis from 309 K to 294 K. The ECMWF analysis at 1412 indicates more rapid cooling in the 775 and 600 mb layers than in the GLAS analysis, which enhances destabilization. In the final periods, weaker advection of cold air into the surface layer of the GLAS analysis volume contributes to its destabilization. While the ECMWF analysis has a warmer surface layer in the first 48 h, during occlusion cold air is advected into the volume at a greater rate, and by 1600 the surface layer of the ECMWF analysis is cooler than in the GLAS analysis.

Static stability values similar to those defined by Sandgathe (1981) as:

$$\sigma = -\alpha \frac{1}{\theta} \frac{\partial \theta}{\partial p}$$

will be used within the 1000-500 mb layer. The specific volume of the layer is assumed constant with time. The potential temperature fields indicate rather uniform structure for the lower troposphere through time, so the stability index can be simplified as $-\frac{\partial \theta}{\partial p}$.

The static stability trends for the GLAS and ECMWF analyses are shown in Fig. 26. Both analyses show a destabilization of the layer for 36 h followed by an increase in stability after 1412. Because temperature differences between the two analyses are consistent throughout the lower troposphere

in the early periods, stability indices vary only slightly. The effect of the greater cooling between 500-800 mb in the ECMWF analysis (Fig. 25b) at 1412 is reflected in the slightly lower stability index. Similarly, the higher stability of the ECMWF analysis in the final period is a direct reflection of the cold air advection into the surface layer observed in Fig. 25b.

Comparison of the SAT and NOSAT potential temperature fields (Fig. 27) with the GLAS analysis indicate several important differences. The storm representation in the SAT prognosis cools in the mid-troposphere between 1300 and 1312, although surface layer temperatures are similar to the GLAS analysis. The strong cooling at 600 mb (500-700 mb layer) is responsible for the rapid decrease in stability for the SAT storm at 1312 (Fig. 26). Mid-tropospheric temperatures in the SAT and NOSAT prognoses remain lower than in the GLAS analysis throughout the storm and the stability likewise remains low. Low stability values computed for the NOSAT prognosis result from a combination of slightly lower mid-tropospheric temperatures and slightly higher surface layer temperatures as compared with the GLAS analysis. The low stability found in the early periods of both prognoses may contribute to convective processes in the early periods, which would help explain the overdevelopment in the first 24 h of both prognoses.

Low stability is not the only factor contributing to the rapid deepening in the prognoses. The NOSAT storm at 00 GMT

14 January is 8 mb deeper than the SAT storm in spite of the lower stability for the SAT storm. Throughout the storm, both prognoses indicate lower stability (1 K/100 mb) than the analyses. In the early periods, this is due primarily to lower 500 mb temperatures, which is consistent with the respective storm tracks toward the cold air. In the later periods, this effect in combination with a warm surface layer tends to further destabilize the lower troposphere.

C. VERTICAL MASS TRANSPORT

The storm vertical mass transport is examined through vertical time sections of omega fields. For this study, omega is calculated using the kinematic method. The O'Brien (1970) correction scheme is utilized to correct for residual imbalances.

Time sections of area-averaged omega in the GLAS (Fig. 28a) and ECMWF analyses (Fig. 28b) each indicate mid-tropospheric maxima during the explosive phase of development, although there are some differences in magnitude. The GLAS analysis indicates a slightly larger vertical velocity maximum that lags by 12 h the ECMWF maximum. These time differences in maximum vertical motion are consistent with the central surface pressure of the ECMWF being 4 mb deeper than the GLAS analysis at 12 GMT 14 January. During the subsequent 12-h period, when vertical motion of the GLAS analysis was at a maximum, a 20 mb pressure fall was analyzed.

The omega time-sections for the SAT and NOSAT prognoses (Fig. 29) both indicate larger upward vertical motion during the early periods than in the analyses. The NOSAT prognosis shows stronger omega over a longer period of time, which is consistent with more rapid development (Fig. 1).

D. HORIZONTAL MASS FLUX

Vertical time sections of horizontal mass transport for the four data sets are depicted in Figs. 30 and 31. The GLAS analysis (Fig. 30a) has a two-layer regime of low-level mass influx associated with surface layer convergence and a layer of mass outflow associated with upper-level divergence. The surface layer convergence, while more intense than the upper-level divergence, is confined to a more shallow layer. The weaker, though more extensive, upper-level outflow region causes a net mass loss in the volume that is reflected in the falling surface pressures. As the circulation intensifies, the level of non-divergence (LND) rises to a higher level, and there is a thicker layer of mass influx.

The horizontal mass flux maxima of the GLAS analysis (Fig. 30a) and the ECMWF analysis (Fig. 30b) are consistent in magnitude for both surface convergence and upper-level divergence. The major difference is that the time of maximum lateral mass transport in the GLAS analysis lags by 12 h the ECMWF analysis.

The SAT and NOSAT horizontal mass flux fields are shown in Fig. 31. As in the analyses, the two-level inflow/outflow

regimes are present in both prognoses, and are consistent with their respective vertical motion fields. However, as the vertical motion fields suggest, the horizontal mass fluxes in the prognoses are clearly different from the analyses. The NOSAT prognosis (Fig. 31b) indicates large mass outflow (divergence) aloft in the early periods, which is consistent with more rapid deepening. During the most explosive phases of storm development, upper-level divergence in the analyses exceeds that of the NOSAT, although by 1500 the intensities of the analysis and NOSAT prognosis are similar. The SAT prognosis (Fig. 31a) horizontal mass transport is similar to that of the NOSAT prognosis, but magnitudes of transport are slightly smaller.

The LND of each prognosis is relatively constant throughout development, and is not gradually rising as in the analysis. This means that in the first 36 h the convergent layer was thicker in the prognoses (note position of LND at 1318 in each storm). Examination of the LND is a good indicator of each storm's stage of development. The analysis LND increases steadily over the 72-h period and appears to reach maturity at the final time period. The SAT storm LND rises to a maximum after 36 h, levels off and then decreases in the final two periods. The NOSAT LND reaches peak values even earlier than the SAT (24 h), although the rise and fall are less dramatic than in the other two representations. Coincident with the high LND of the NOSAT storm is the maximum

mass outflow in the upper troposphere. This is most likely the result of the NOSAT storm's different relationship to the jet streak discussed in Chapter II, and appears to be a major factor in explaining early development in the NOSAT prognoses.

E. CONCLUSIONS

The mass budget study provides explanation for some of the differences in development observed in Chapter II between the analyses and prognoses. The 12-h time lag in the GLAS analysis vertical motion and horizontal mass transport helps explain the different analyzed surface pressure in the two analyses at 12 GMT 14 January. Aside from this time difference, the mass budget results from the two analyses are consistent.

Prognostic mass budgets substantiate overdevelopment during the early periods with less intense mass transport and vertical motion during the most explosive stages of development. The NOSAT prognosis clearly has larger divergence aloft in the early periods than the SAT prognosis, which is consistent with more rapid development. The differences in upper-level flow between the prognoses are most likely due to the differences in jet stream intensity as discussed in Chapter II.

Static stability throughout all time periods is lower in the prognoses than in the analyses, and probably contributed to enhanced convective activity and the overdevelopment of

both prognoses. This is particularly true for the SAT prognosis. Upper-level divergence in the early periods was not as strong in the SAT prognosis as in the NOSAT prognosis, yet both the SAT and NOSAT prognoses overdeveloped the storm. The more rapid destabilization in the early periods of the SAT prognosis (Fig. 26) appears to contribute substantially to development.

IV. VORTICITY BUDGET ANALYSIS

A. GENERAL

The absolute vorticity budget results for the GLAS analysis, SAT prognosis and NOSAT prognosis are now presented. The sign convention is positive for processes producing vorticity increases in the budget volume (sources), and negative for vorticity decreases (sinks). As in the previous chapter, all budget figures are for the radius 10 budget volume.

The main emphasis of this chapter is a discussion of the absolute vorticity time tendency as a measure of storm development. The role of various forcing terms such as horizontal and vertical absolute vorticity transport, advection, generation and dissipation in storm dynamics is explored. The horizontal transport terms are separated into lateral divergence and lateral advection components to investigate their individual contribution to storm development. Vertical transport terms reflect vertical divergence and advection from omega values derived from the kinematic method. Table III of Appendix B provides an outline of the vorticity budget terms.

As in the previous chapter, budget results from four data sets are compared. The GLAS analysis is compared to the ECMWF analysis as discussed by Calland (1983), and both

analyses are used as a basis for comparison of the SAT and NOSAT prognoses.

B. VORTICITY TENDENCIES

The build-up of absolute vorticity for the cyclone in the GLAS analysis over the three-day period is shown in Fig. 32a. Absolute vorticity increases most notably occur between 1300 and 1500. This increase is the result of increased circulation of storm development plus the increased planetary vorticity as the storm tracks northward.

Comparing the GLAS analysis time section with that of the ECMWF analysis (Fig. 32b) reveals basically similar features. Slight differences in magnitude and/or time of events are observed due to the different resolution of the two analyses.

Vertical time sections of absolute vorticity for the SAT and NOSAT storms appear as Fig. 33. Both prognoses indicate an earlier increase in vorticity. In the final periods, the SAT prognoses contain relatively higher vorticity than the NOSAT prognoses. The decreased vorticity in the NOSAT prognoses during the final two periods is consistent with the earlier filling of the low in the NOSAT depiction of the storm.

Absolute vorticity time tendency, which is the first term in the vorticity budget equation (see Table III), is depicted for each of the four storms in Figs. 34 and 35. These displays are time derivatives of the fields depicted in Figs.

32 and 33. The GLAS analysis vorticity tendency (Fig. 34a) is largest in the upper levels for the initial periods, with smaller tendencies in the lower layers. The ECMWF analysis vorticity tendency (Fig. 34b) indicates a minimum in the mid-troposphere at 1318, which does not appear in the GLAS analysis. Calland (1983) attributes the presence of this minimum in the ECMWF vorticity tendency to analysis problems, so the GLAS analysis tendency is considered to be more accurate during this time period. At other time periods the two vorticity tendencies are generally consistent.

The SAT vorticity tendency (Fig. 35a) is generally similar to the GLAS analysis, except that the key features indicating certain stages of development clearly occur much earlier. SAT vorticity tendency is large in the upper layers at 1306, but soon after decreases rapidly to levels more consistent with the analyses. The initially large tendency in the jet region is most likely the model's response to the weaker winds east of the jet streak. As discussed in Chapter II, the magnitude of the SAT jet stream winds at 00 GMT 13 January was less than the NOSAT prognosis, but by 12 GMT 13 January the difference had diminished considerably (Figs. 8a and 9a). Therefore, the model's apparent response to the weaker jet winds was to increase vorticity and to strengthen the jet. The NOSAT vorticity tendency (Fig. 35b) does not indicate the strong initial tendency at the jet level due to its different jet winds, but does indicate stronger tendency aloft in the middle periods than the SAT prognosis. NOSAT

tendency in the lower layers at 1318 is consistent with the overdevelopment of the surface low.

C. LATERAL TRANSPORT OF ABSOLUTE VORTICITY

The lateral transport of absolute vorticity is one of the three major forcing terms in the budget equation (see Table III). The lateral transport term can be partitioned into components of lateral divergence and advection of vorticity.

The GLAS analysis total lateral vorticity transport time section (Fig. 36a) indicates strong transport into the volume at the upper levels during the initial period, as in the ECMWF analysis (Fig. 36b). As circulation becomes well established, a transport maxima develops in the surface layer that is consistent with horizontal mass transport and maximum vertical motion. Coincident with the surface maxima is a negative transport maxima aloft. Comparison with the ECMWF analysis reveals generally similar features except that the GLAS analysis contains a slightly larger inward transport maxima in the surface layer. Additionally, the GLAS analysis exhibits outward transport aloft in the later periods, while the ECMWF analysis contains small inward transport aloft.

Both the SAT (Fig. 37a) and the NOSAT lateral vorticity transport (Fig. 37b) more closely resemble the ECMWF analysis than the GLAS analysis in terms of structure and magnitude. The major differences between SAT and NOSAT lateral

transport are the stronger transport in the upper layers at 1306 for the SAT storm, which is consistent with the vorticity tendency term. Also, larger transport aloft exists in the SAT prognosis in the final periods.

D. LATERAL DIVERGENCE COMPONENT

The traditional way to partition lateral transport of absolute vorticity is in terms of lateral divergence and advection components through the use of vector identities (see Table III). The GLAS divergence component (Fig. 38a) is composed of a two-layer regime with positive vorticity production (convergence) in the surface layer and negative vorticity production (divergence) aloft. The surface layer convergence maximum occurs at 1418. The ECMWF analysis lateral divergence component (Fig. 38b) shows the same two-level regime as the GLAS analysis, except that maximum surface convergence is less intense and occurs over 12 h earlier. Upper-level divergence maxima in the two analyses are of similar magnitude and are nearly time consistent.

Both prognoses lateral divergence (Fig. 39) components indicate a rapid increase in divergence aloft in the early periods and achieve a maximum that exceeds the analyses. The magnitude of the surface convergence maxima in both prognoses is slightly less than in the analyses, but the maxima are elongated over time. This observation is consistent with the developmental trends seen in Fig. 1. Both prognoses deepen the storm rapidly from the outset and

continue at a steady rate until occlusion, rather than beginning slowly and then undergoing explosive development in the middle periods. The NOSAT lateral divergence (Fig. 39b) indicates larger divergence aloft than in the SAT storm (Fig. 39a) from the outset. This stronger surface convergence is consistent with the more intense development in the NOSAT prognosis.

E. LATERAL ADVECTION COMPONENT

The ECMWF vorticity advection component (Fig. 40b) exhibits a two-layer regime with negative vorticity advection (NVA) below 775 mb and positive vorticity advection (PVA) aloft. Calland (1983) attributes the strong NVA in the surface layer to an asymmetric east-west oriented vorticity maxima coupled to the strong cyclonic flow, which allows the advection of smaller vorticity values into the volume. GLAS analysis lateral vorticity advection also indicates a two-layer regime with NVA in the lower layers and PVA aloft (Fig. 40a). The GLAS analysis differs from the ECMWF analysis in having relatively weaker PVA aloft and a 24 h lag in maximum surface layer NVA. The weaker PVA maxima of the GLAS analysis is consistent with the weaker jet stream winds over the surface low at 00 GMT 14 January (Figs. 4a and 10a, Calland).

Strong upper-level PVA during the initial period accounts for the large lateral transport of vorticity in the SAT prognosis (Fig. 41a). The NOSAT lateral vorticity advection

indicates PVA maxima in excess of the SAT prognosis and is consistent with the ECMWF analysis. The combination of stronger upper-level vorticity divergence and stronger PVA is consistent with the more rapid deepening rate of the NOSAT prognosis compared to the SAT prognosis.

F. VERTICAL REDISTRIBUTION

The third major term in the vorticity budget equation (Table III) involves the vertical redistribution of vorticity from the lower layers to the middle and upper troposphere. The transfer of vorticity in the mid-troposphere intensifies mid-level circulation and amplifies the mid-level trough as the storm develops. The effect of the vertical transport in the vorticity budget is given by the divergence of the vertical transport. This term can be partitioned into a vertical divergence and an advection component. The vertical divergence component (not shown) is the negative of the lateral divergence term discussed in Section D and indicates large losses of vorticity in the surface layer and gains aloft.

The GLAS analysis vertical advection component (Fig. 42a) plays a small role in the vertical transport of vorticity. A maxima is observed in the mid-troposphere during the later periods when both surface layer vorticity and vertical motion are large. The ECMWF analysis vertical advection component (Fig. 42b) indicates a mid-level maxima similar to the GLAS analysis, although it occurs earlier. This is consistent

with the differences between the two analyses in the time of maximum vertical motion noted earlier.

The vertical advection components of both prognoses (Fig. 43) indicate mid-tropospheric maxima during the later periods. The maxima are of similar magnitude to the analyses and occur at about the same time as the GLAS analysis (Fig. 42a). The NOSAT maximum (Fig. 43b) is slightly larger than the SAT maximum (Fig. 43a) due to slightly larger vertical motion in the NOSAT prognosis (Fig. 29). The minor contribution of vertical advection to the total budget results is consistent with previous studies of DiMego and Bosart (1982) and Chen and Bosart (1979).

C. SOURCES AND SINKS

The final term in the vorticity budget equation (Table III) involves the collective input of absolute vorticity sources and sinks. Sources of vorticity are represented by the divergence and tilting terms, and frictional dissipation is a vorticity sink. This section will discuss the impact of these three components on each of the four storm representations.

The generation of vorticity by horizontal divergence is mathematically equivalent to the lateral divergence component of the lateral transport term discussed in Section C and shown in Figs. 38 and 39. Discussion of divergence as a source term will not be repeated here.

The tilting term is the result of vertical vorticity generated by the tilting of horizontally oriented vorticity

elements by a non-uniform vertical motion field. For this term to be sizable, strong vertical shear and a horizontally varying omega field are required. The tilting terms of the GLAS and ECMWF analysis (Fig. 44) are of opposite sign to their respective vertical advection terms, which indicates a small negative contribution in the mid-troposphere during the rapid development phase. Similar features are observed in the SAT and NOSAT prognoses (Fig. 45).

Frictional dissipation is assumed to occur only in the surface boundary layer and is parameterized using a stability dependent scheme [Johnson and Downey, 1976]. The frictional dissipation of the ECMWF analysis (Fig. 46b) at 1506 GMT is of similar magnitude to the low-level maximum in the lateral transport of vorticity (Fig. 36b), which suggests that frictional effects assume a large role in the dissipation of vorticity in the surface layer. The maximum frictional dissipation in the GLAS analysis (Fig. 46a) is slightly higher than that of the ECMWF analysis. Frictional dissipation in the SAT and NOSAT prognoses (Fig. 47) are also of similar magnitude to their respective lateral transport terms in the surface layers. Magnitudes of frictional dissipation in the three GLAS fields are in direct proportion to the magnitude of lateral mass transport in the surface layer and deepening rate in each depiction of the storm.

H. RESIDUALS

The residual in the vorticity budget contains the effects of the omitted processes plus the accumulated errors in the

calculation of the resolved terms. Inaccuracies in the vertical motion and horizontal wind fields contribute to the physical residual components, whereas spatial and temporal finite differencing and grid-point interpolation inaccuracies are causes for computational errors [Calland, 1983]. Positive residuals indicate that the observed vorticity increases at a point exceed those of the computed terms.

The vorticity budget residual of the GLAS analysis (Fig. 48a) indicates a sizable vorticity excess in the mid-troposphere and a vorticity deficit in the lower troposphere during the explosive phase of development. Similar residuals of a smaller magnitude are observed in the ECMWF analysis (Fig. 48b). Based on a term-by-term comparison of the two analyses, the larger positive residual at 450 mb in the GLAS analysis is apparently due to an excessive negative lateral divergence component. Similarly, the vorticity deficit in the lower layers of the GLAS analysis is due to an excessive positive contribution from the lateral divergence component.

Residual values for the SAT and NOSAT prognoses (Fig. 49) are generally low at all times. The largest residual occurs in the surface layer of the NOSAT prognosis during the early periods where observed vorticity tendency exceeds the sum of the budget terms. This residual is most likely due to the different representations of frictional dissipation in the model and budget computations. Similarly, different

representations of vertical motion in the model and budget computations contribute to the residual. As in the analyses, the largest residuals in the prognoses occurred during the most rapid development phase. For the prognoses, this occurred in the early time periods. Development in the prognoses was consistently strong in the first 48 h, as opposed to modest development followed by explosive development in the analyses. GLAS analysis residuals resulted from difficulties in the resolution of the rotational and divergent components during the explosive phase of development. The GLAS prognoses residuals resulted primarily from differences between the model and budget computational methods for friction and vertical velocity.

I. CONCLUSIONS

Comparison of the vorticity budget results of the GLAS and ECMWF analyses reveals several differences. As in the mass budget study, the GLAS analysis surface layer maxima of the various vorticity terms consistently lag by 12 h those of the ECMWF analysis. Secondly, the GLAS analysis lateral divergence of vorticity term is too large in the surface layer, and contributes to a negative budget residual. The large positive residual in the mid-troposphere of the GLAS analysis is most likely due to the 12 h time lag in the divergence of the vertical transport.

Vorticity budgets for the prognoses support earlier and more rapid development than in the analyses. The NOSAT

prognosis develops the storm more rapidly than the SAT prognosis primarily due to stronger divergent flow aloft. This effect is the direct result of a stronger jet stream in the initial NOSAT fields.

V. CONCLUSIONS AND RECOMMENDATIONS

A diagnostic verification of the GLAS analysis scheme and global forecast model was conducted for a North Pacific case of extratropical explosive cyclogenesis during 13-16 January 1979. Storm related mass and vorticity budgets were computed for the cyclone using the GLAS FGGE analyses and the SAT and NOSAT FGGE prognoses. Results were verified using budget results of the ECMWF FGGE analyses as described by Calland (1983).

The coarser grid and more simplified analysis scheme of the GLAS analyses compared favorably to the ECMWF analyses. Insufficient resolution during the period of maximum storm deepening caused the GLAS analysis to under-analyze storm intensity at 12 GMT 14 January. At all other times storm intensities and positions of the two analyses were very close.

GLAS prognoses initialized with FGGE data forecast the storm much more accurately than operational forecasts. The Navy operational forecast underdeveloped the storm, whereas the GLAS forecasts with FGGE data overdeveloped the storm and positioned it more accurately. In this case, the impact of the comprehensive FGGE data set on the forecasts was positive.

This case of explosive cyclogenesis was characterized by largely zonal mid-tropospheric flow and strong jet streak

interaction aloft that induced explosive development. The inclusion of underestimated cloud-drift winds in the FGGE data weakened the intensity of the jet in the SAT prognosis, and adversely affected the forecasts. Due to more intense jet stream winds, the NOSAT prognosis indicated greater surface convergence, greater divergence aloft, greater vertical motion and greater PVA than in the SAT prognosis. The NOSAT prognosis developed and positioned the storm more accurately than the SAT prognosis. The case evaluated in this study demonstrates that a larger data base like FGGE can improve a forecast. However, the SAT/NOSAT comparison suggests that more data may not always be better, and that data quality is equally as important as data quantity.

The approach taken in this thesis was to concentrate on a single system and perform an in-depth diagnostic study and describe the processes involved in explosive cyclogenesis. The conclusions reached in this thesis are for this single storm. It is recommended that future research examine other extratropical maritime explosive cyclones and specifically cases for which both SAT and NOSAT prognoses are available.

Without the FGGE, a study of this type would not have been possible. Data gaps have always made forecasting over ocean areas difficult. Satellite data in recent years have helped greatly in filling data gaps, and imagery has unquestionably aided the forecaster. It is not known if the errant jet stream cloud-drift winds seen in this study are unique

to this particular storm. It is recommended that the procedure for evaluating cloud-drift winds prior to data assimilation be reviewed.

APPENDIX A

FGGE DATA

The data collected during the first special observation period (SOP-1) of the Global Weather Experiment represented the most intensive effort ever attempted in atmospheric and oceanographic data collection. The experiment clearly demonstrated that state-of-the-art technology coupled with outstanding resource management can produce the higher quality data sets needed for the improved performance of numerical prediction models.

The GLAS objective analysis procedure is characterized by Baker (1983) as a modified Cressman scheme based on a method developed by Bergthorsson and Doos (1955). The GLAS assimilation/forecast model consists of nine vertical levels in sigma coordinates with a non-staggered horizontal resolution of 4 degrees latitude by 5 degrees longitude. All horizontal differences are computed with fourth order accuracy.

Substantial preparation of the FGGE level II-b data was performed by GLAS prior to implementing the objective analysis scheme. Of the changes made to the level II-b data, the most significant to the study of the North Pacific storm was the correction of the Japanese cloud-drift winds. The Japanese upper tropospheric cloud-drift winds were considerably

smaller in magnitude than surrounding rawinsonde and aircraft reports. This error was attributed to erroneous altitude assignment [McPherson, 1984]. Altitude errors were likewise observed in the Japanese lower tropospheric cloud-drift winds. The method used was to assign the wind altitude to the low cumulus cloud-top altitude as determined by brightness temperature. Studies determined that low-level cloud-drift winds are most accuarate at the cloud base, and not the cloud top [McPherson, 1984]. Consequently, all low level cloud-drift winds were reassigned by GLAS to the 900 mb level (the average cloud-base level over the ocean). Altitudes of cloud-drift winds between 400 mb and the tropopause were reassigned based on cloud-top brightness temperature [Baker, 1983].

The GLAS analysis first-guess is provided by the 6-h model prognosis at the model sigma levels and must be interpolated to the mandatory pressure levels. Observed data are then ingested and compared to the first-guess values. Data differing from the first-guess by a specified amount are flagged as suspect and then checked against surrounding data. If acceptance criteria are still not met, the data are rejected. The "good" data are then interpolated to the 4 degree by 5 degree grid using the Cressman scheme, which has been modified to consider data quality and variable data density. The u and v wind components, heights, and relative humidity are analyzed at the mandatory pressure levels, and

the surface pressure and surface temperature are reduced to sea level and analyzed.

APPENDIX B

TABLES

TABLE I

Generalized QLD Budget Equation in Isobaric Coordinates
(After Wash, 1978)

$$F = \int_{1000\ mb}^{100\ mb} \int_{0}^{\beta} \int_{0}^{2\pi} \frac{1}{g} f r^2 \sin \lambda \, d\alpha \, d\beta \, (-dp)$$

where F is the volume integral of the desired budget property f.

The budget equation is

$$\frac{\partial F}{\partial t} = LT(f) + VT(f) + S(f)$$

where the lateral transport is

$$LT(f) = \int_{1000\ mb}^{100\ mb} \int_{0}^{2\pi} \frac{1}{g} (\underset{\sim}{U}-\underset{\sim}{W})_{\beta} \, f \, r \sin \beta \, d\alpha (-dp) \Big|_{\beta}$$

and the vertical redistribution is

$$VT(f) = \int_{1000\ mb}^{100\ mb} \int_{0}^{\beta} \int_{0}^{2\pi} \frac{1}{g} (\omega f) \, r^2 \sin \beta \, d\alpha d\beta \, (-dp).$$

TABLE I (CONT.)

The source/sink term is

$$S(f) = \int_{1000\ mb}^{100\ mb} \int_{0}^{\beta} \int_{0}^{2\pi} \frac{1}{g} \frac{df}{dt} r^2 \sin \beta \, d\alpha \, d\beta \, (-dp) \, .$$

TABLE II

QLD Mass Budget Equations in Isobaric Coordinates
(After Wash, 1978)

The Definition

$$M = \int_{V_p} \frac{1}{g} r^2 \sin\beta \, d\alpha \, d\beta \, dp$$

where f = 1.

The Budget Equation

$$\frac{dM}{dt} = LT + VT ,$$

where

Lateral Transport

$$LT = - \int_{\eta_B}^{\eta_T} \int_0^{2\pi} \frac{1}{g}(U-W)_\beta \, r \sin\beta_B \, d\alpha \, dp \Big|_{\beta_B}$$

Vertical Transport

$$VT = \int_0^{\beta_B} \int_0^{2\pi} \frac{1}{g}(\omega-\omega_B) \, r^2 \sin\beta \, d\alpha \, d\beta \Big|_p$$

where

$$\omega = \frac{dp}{dt} , \qquad \omega_B = \frac{dp_B}{dt} .$$

TABLE III

QLD Circulation Budget Equations in Isobaric Coordinates
(After Wash, 1978)

Section A

$$C_a = \int_{1000\ mb}^{100\ mb} \int_0^{\beta} \int_0^{2\pi} \frac{1}{g} \zeta_a r^2 \sin\beta \, d\alpha \, d\beta \, (-dp)$$

where C_a is the absolute circulation and ζ_a is absolute vorticity. The budget equation is

$$\frac{\delta C_a}{\delta t} = LT(\zeta_a) + DVT(\zeta_a) + S(\zeta_a)$$

where the lateral transport is

$$LT(\zeta_a) = \int_{1000\ mb}^{100\ mb} \int_0^{\beta} \int_0^{2\pi} \frac{1}{g}(\underset{\sim}{U}-\underset{\sim}{W})_\beta \, \zeta_a \, r \sin\beta \, d\alpha (-dp)\Big|_\beta$$

and the divergence of the vertical transport is

$$DVT(\zeta_a) = \int_0^{\beta} \int_0^{2\pi} \frac{1}{g} \frac{\partial}{\partial p}(\omega \zeta_a) \, r^2 \sin\beta \, d\alpha \, d\beta \quad .$$

The source/sink term is

$$S(\zeta_a) = \int_{1000\ mb}^{100\ mb} \int_0^{\beta} \int_0^{2\pi} \frac{1}{g} \frac{d\zeta_a}{dt} r^2 \sin\beta \, d\alpha \, d\beta \, (-dp).$$

TABLE III (CONT.)

Section B

The partitioned form of the vorticity budget equation is

$$\frac{\delta(C_a)}{\partial t} = +LT\,(\zeta_a) + DVT\,(\zeta_a) + S\,(\zeta_a)$$

horizontal divergence	horizontal advection	vertical divergence	vertical advection	divergence term	tilting term	frictional dissipation

The above partitions make use of Stokes' theorem

$$\oint \zeta_a \underset{\sim}{U} \cdot \underset{\sim}{m}\, d\ell = \int\int_A \nabla \cdot \zeta_a \underset{\sim}{U}\, dA ,$$

and the division of total flux ($\underset{\sim}{U}\,\zeta_a$) into divergent and advective components,

$$\nabla \cdot \zeta_a \underset{\sim}{U} = \zeta_a\,(\nabla \cdot \underset{\sim}{U}) + \underset{\sim}{U} \cdot \nabla\, \zeta_a .$$

FIGURES

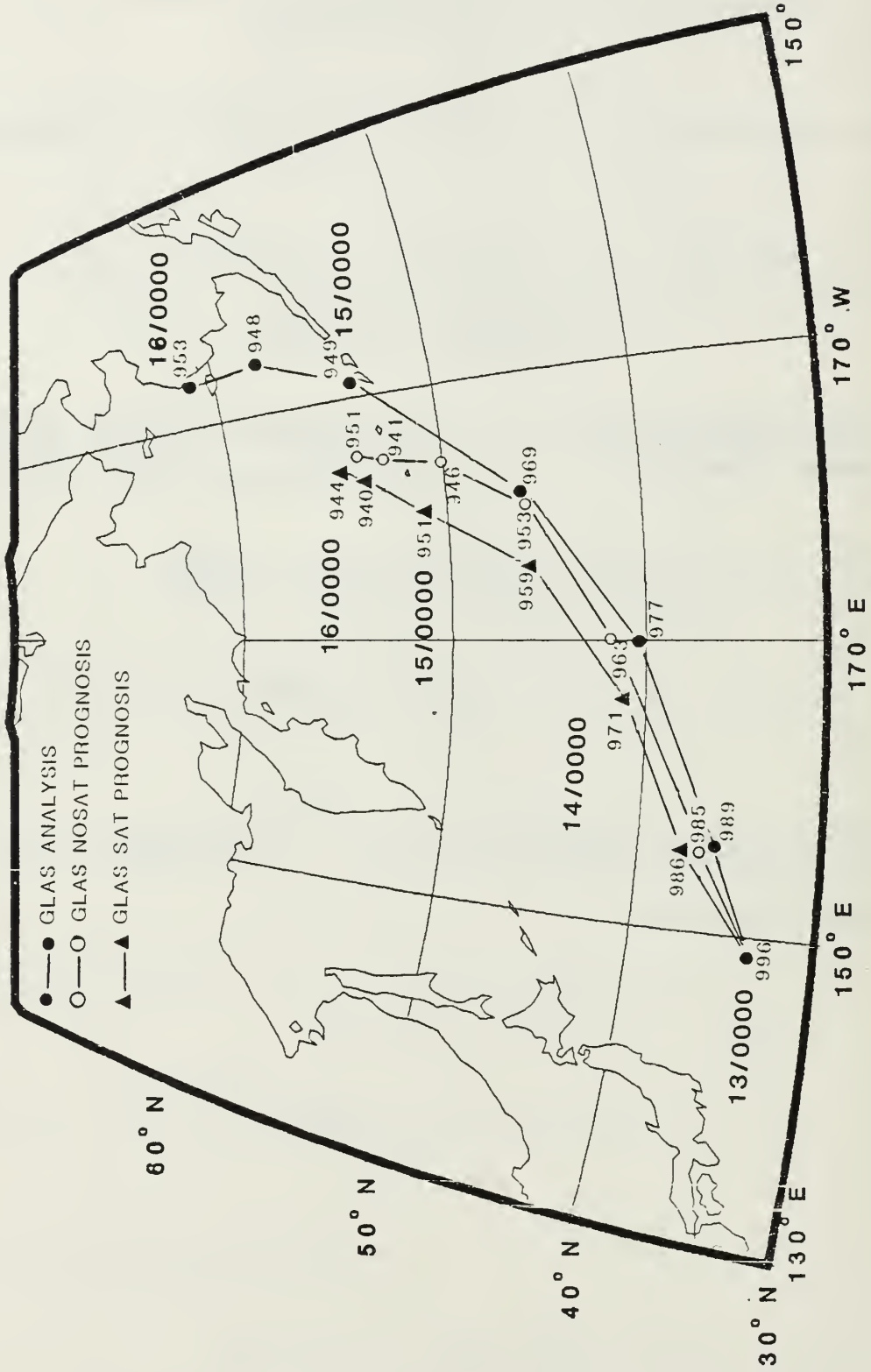

Figure 1. Storm Track Positions and Central SLP at 12-h Synoptic Times

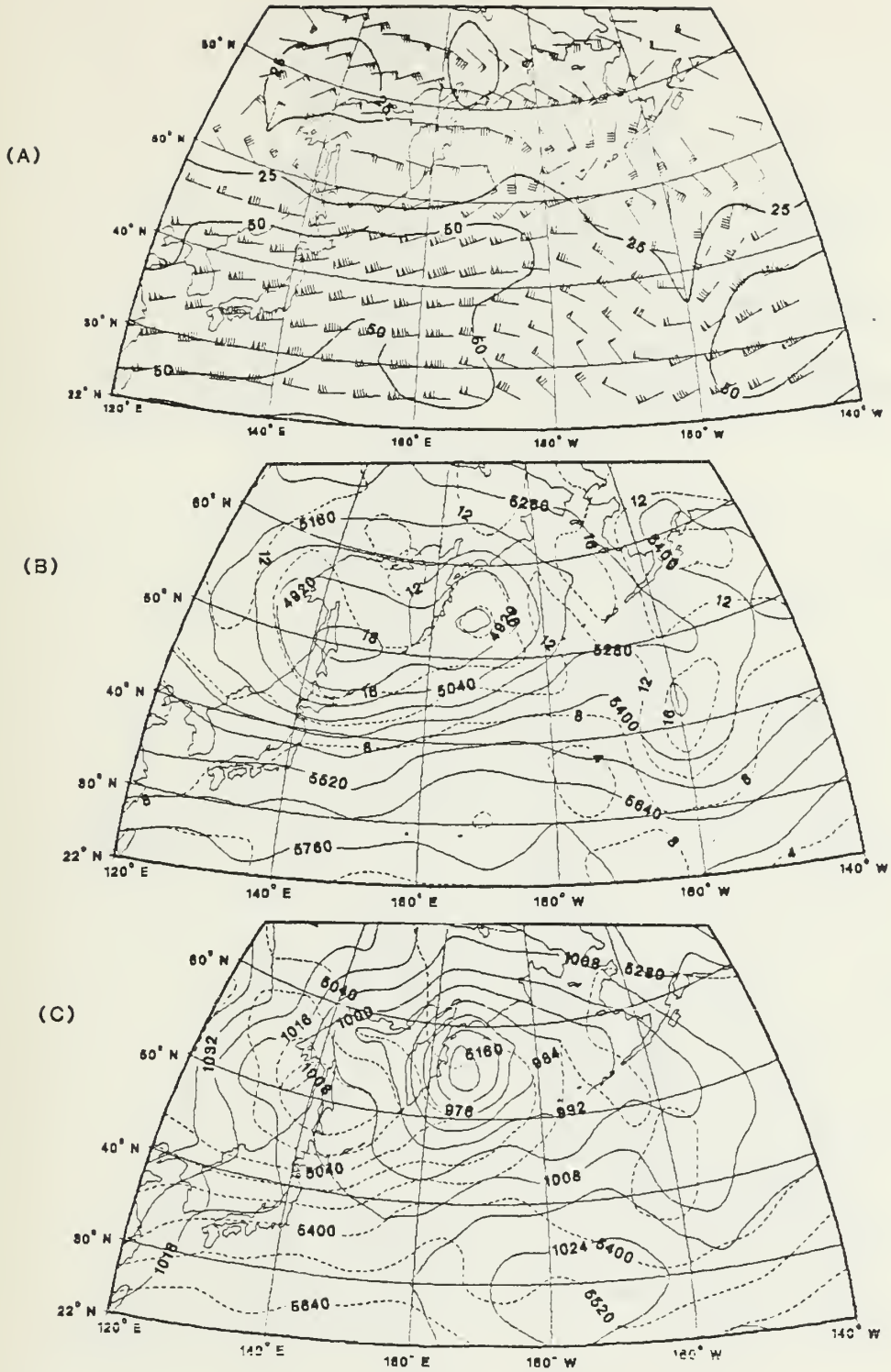

Figure 2. Synoptic Fields for GLAS Analysis at 0000 GMT 12 January 1979. (A) 250 mb winds/Isotachs (m/s). (B) 500 mb Absolute Vorticity (DASHED) X 10**5/sec and Heights (SOLID) in gpm. (C) Sea Level Pressure (SOLID) in mb and 1000-500 mb Thickness (DASHED) in gpm.

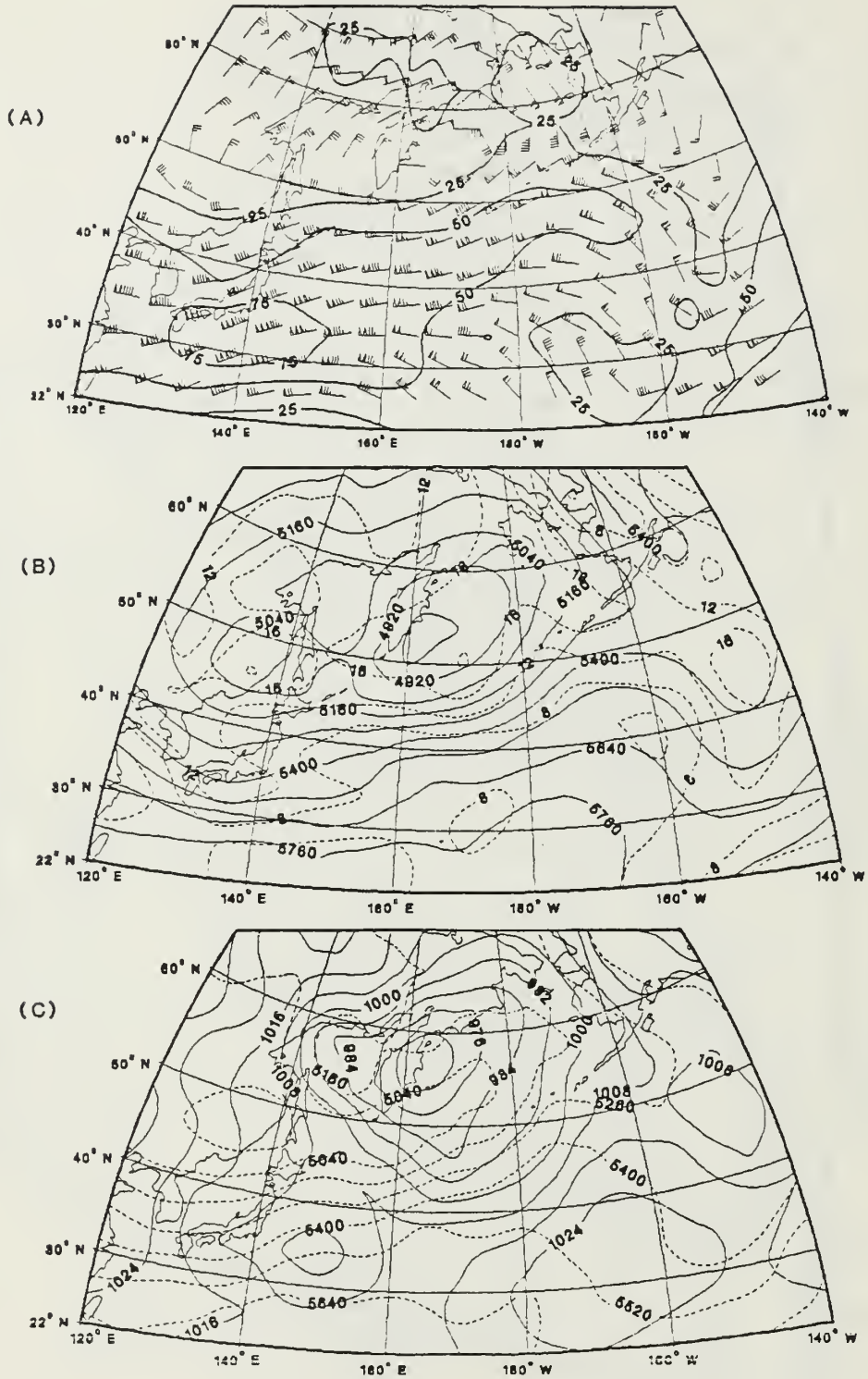

Figure 3. As in Figure 2 except for GLAS Analysis 0000 GMT 13 January

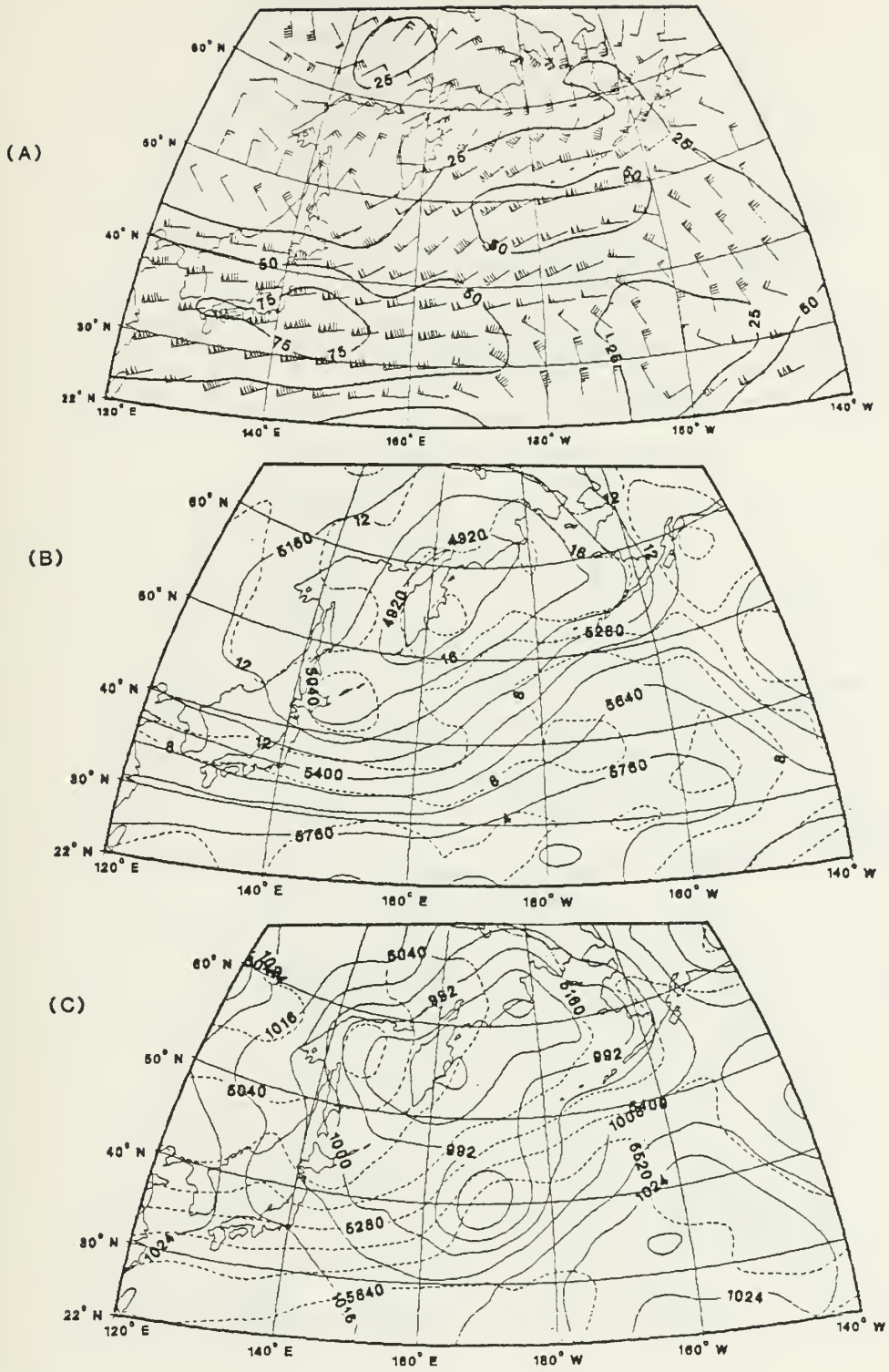

Figure 4. As in Figure 2 except for GLAS Analysis 0000 GMT 14 January

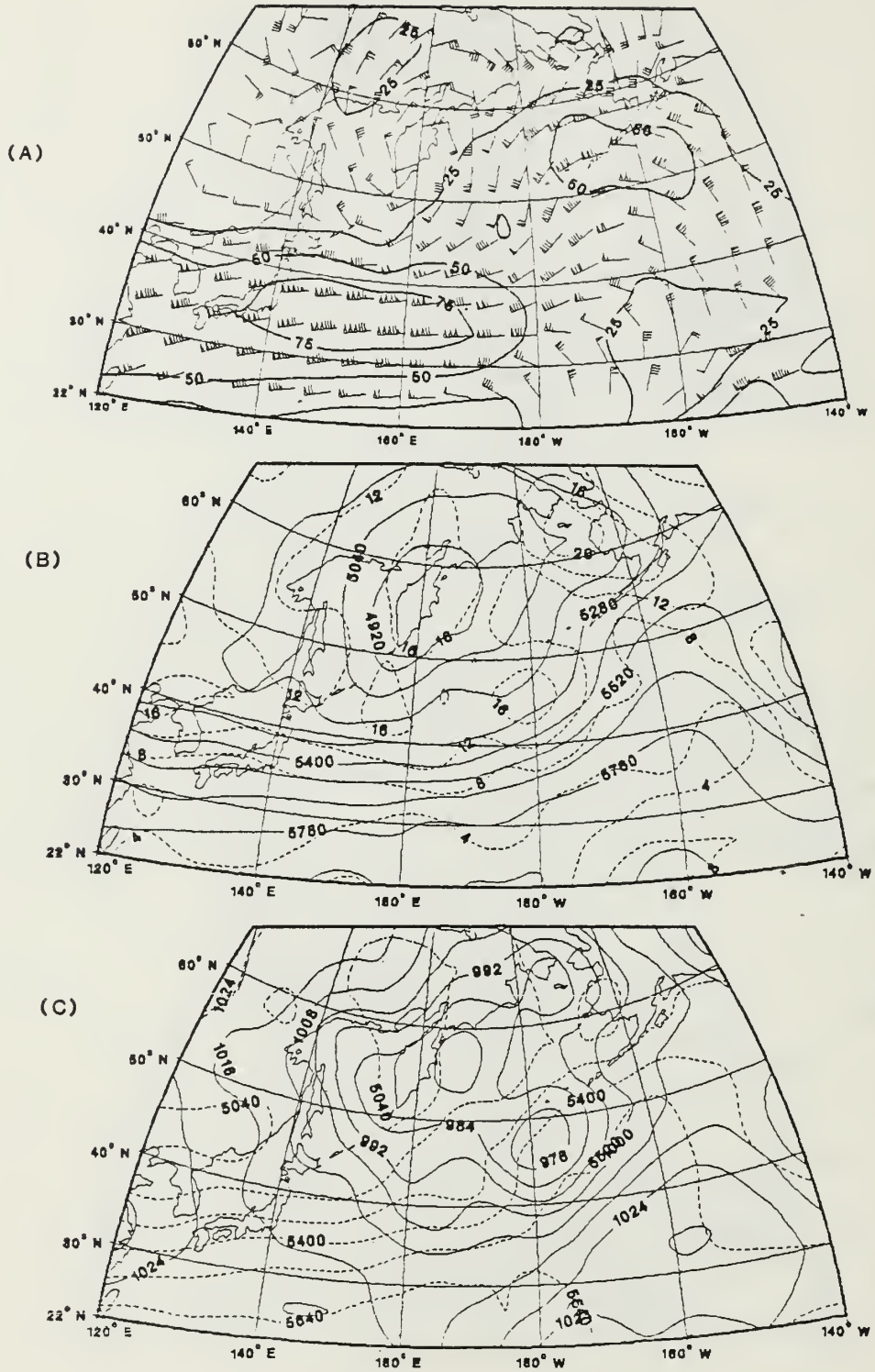

Figure 5. As in Figure 2 except for GLAS Analysis 1200 GMT 14 January

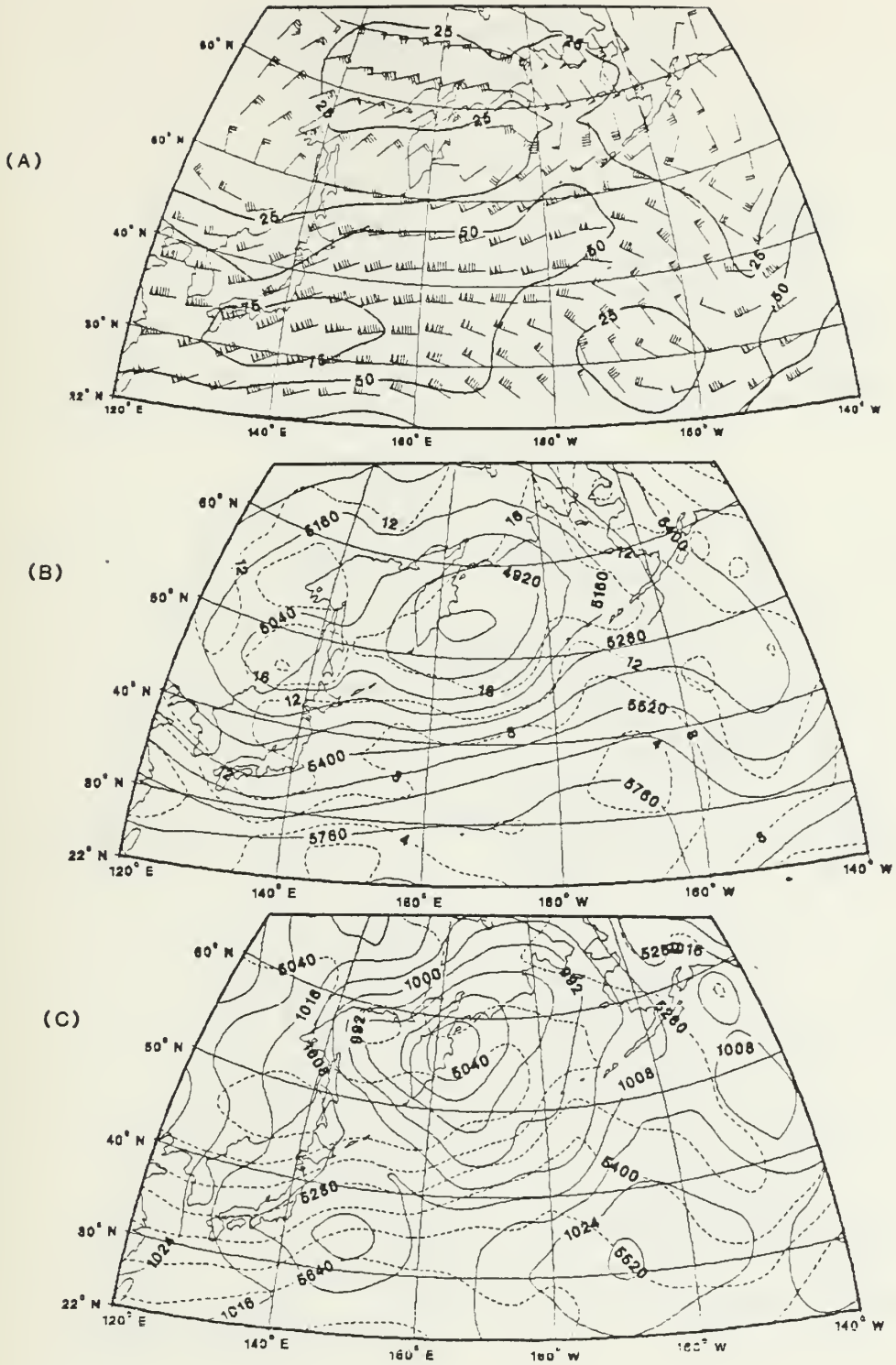

Figure 6. As in Figure 2 except for NOSAT Prognosis 0000 GMT 13 January

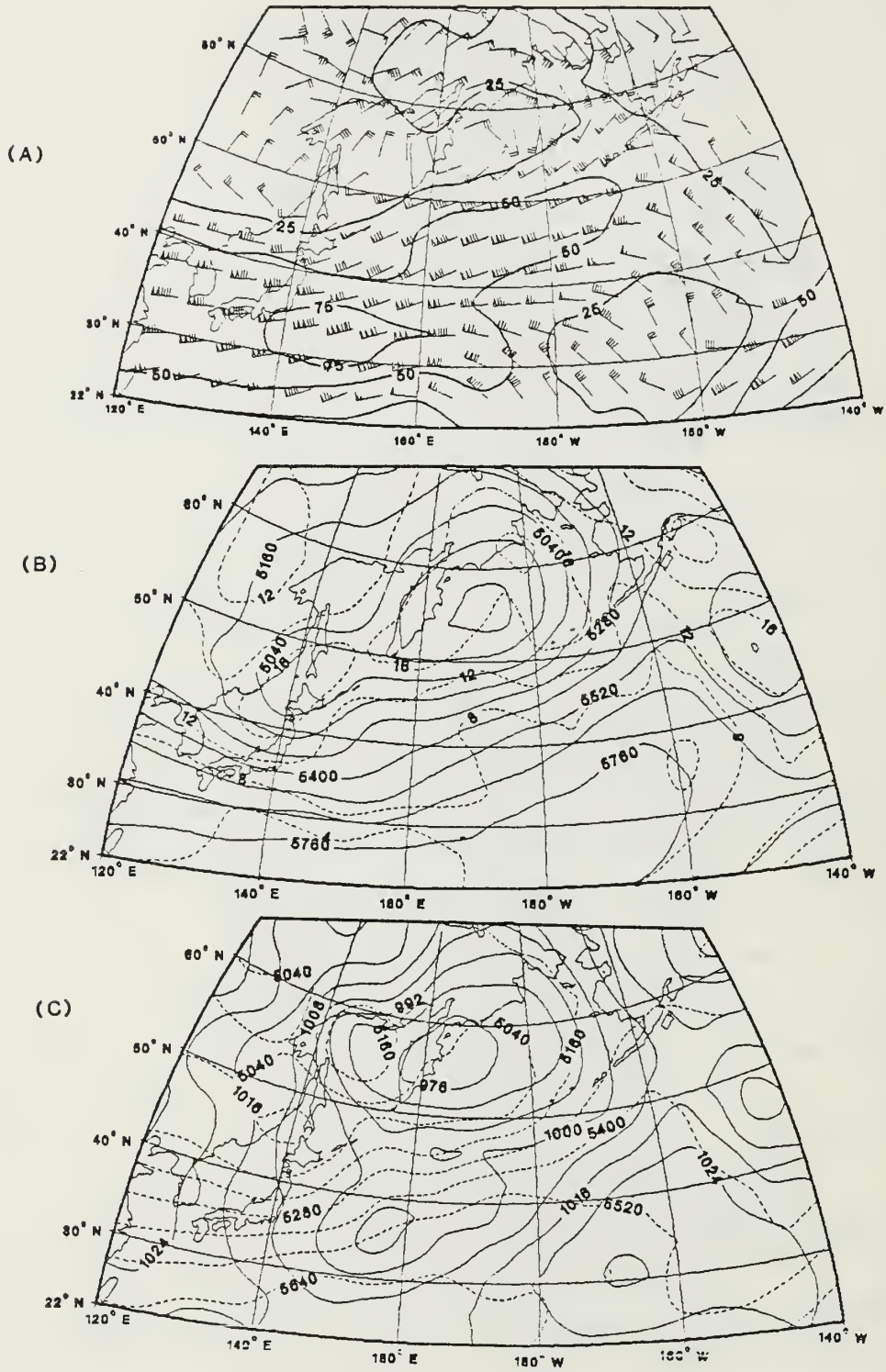

Figure 7. As in Figure 2 except for GLAS Analysis 1200 GMT 13 January

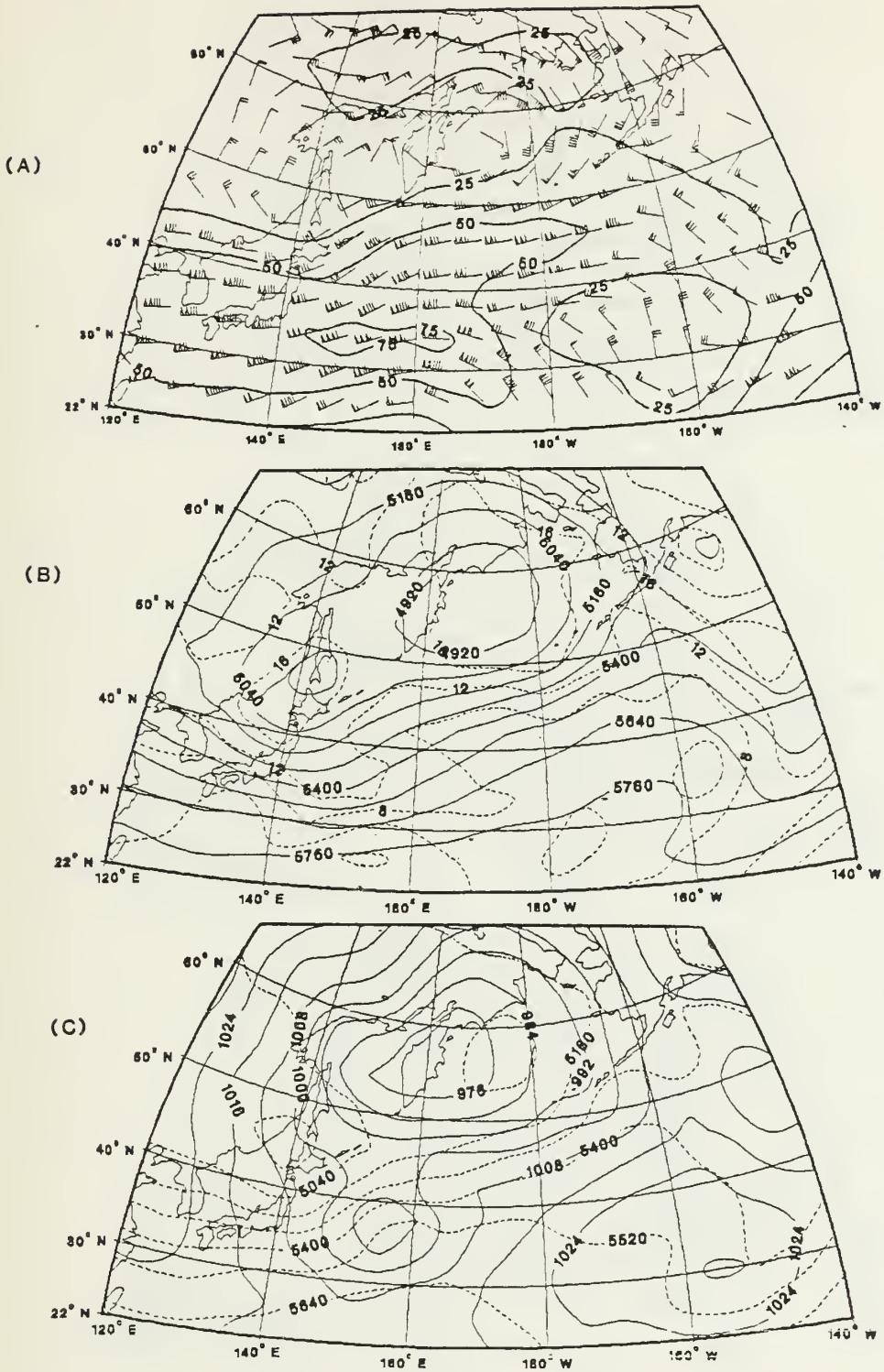

Figure 8. As in Figure 2 except for SAT Prognosis 1200 GMT 13 January

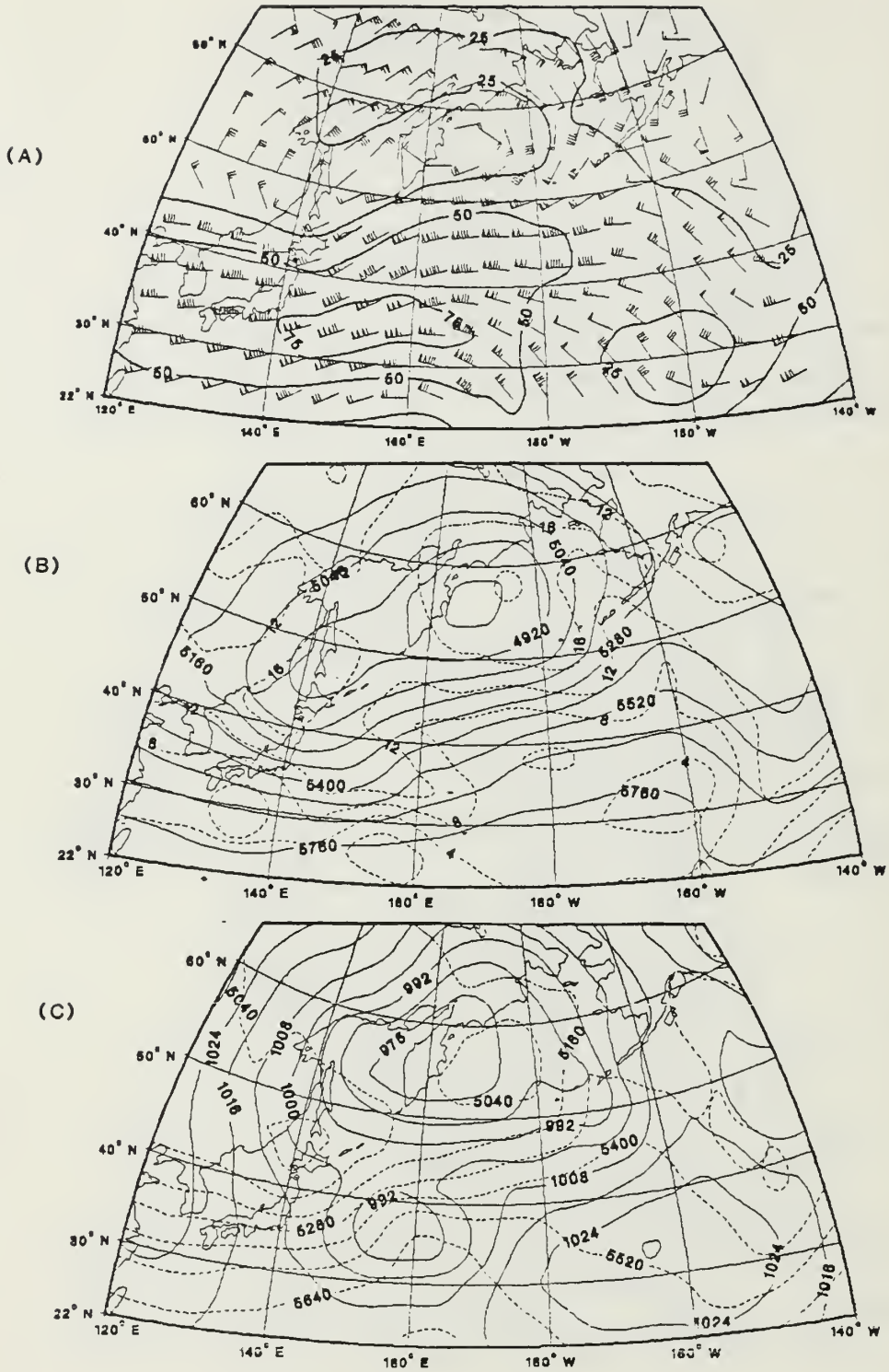

Figure 9. As in Figure 2 except for NOSAT Prognosis 1200 GMT 13 January

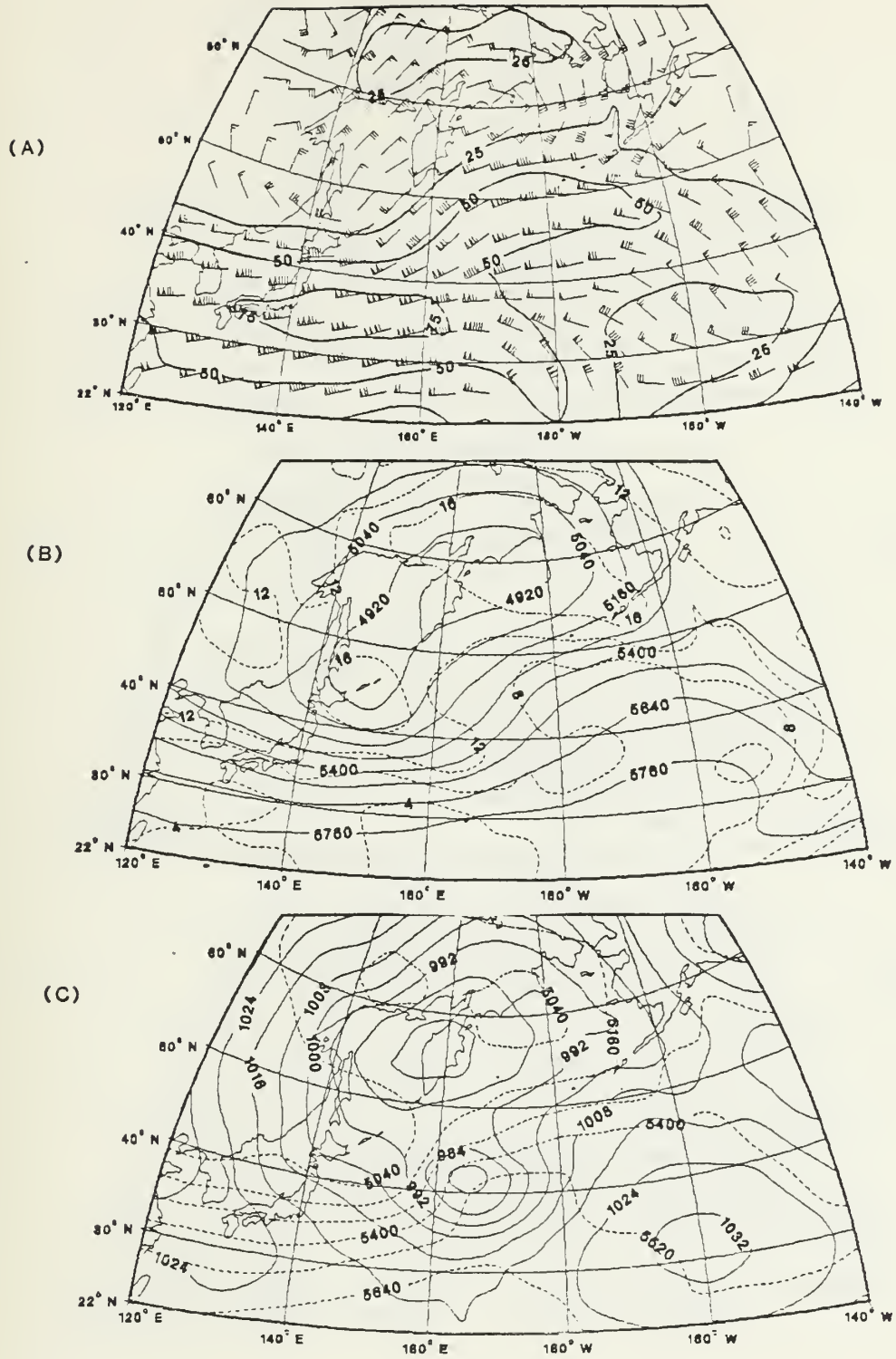

Figure 10. As in Figure 2 except for SAT Prognosis 0000 GMT 14 January

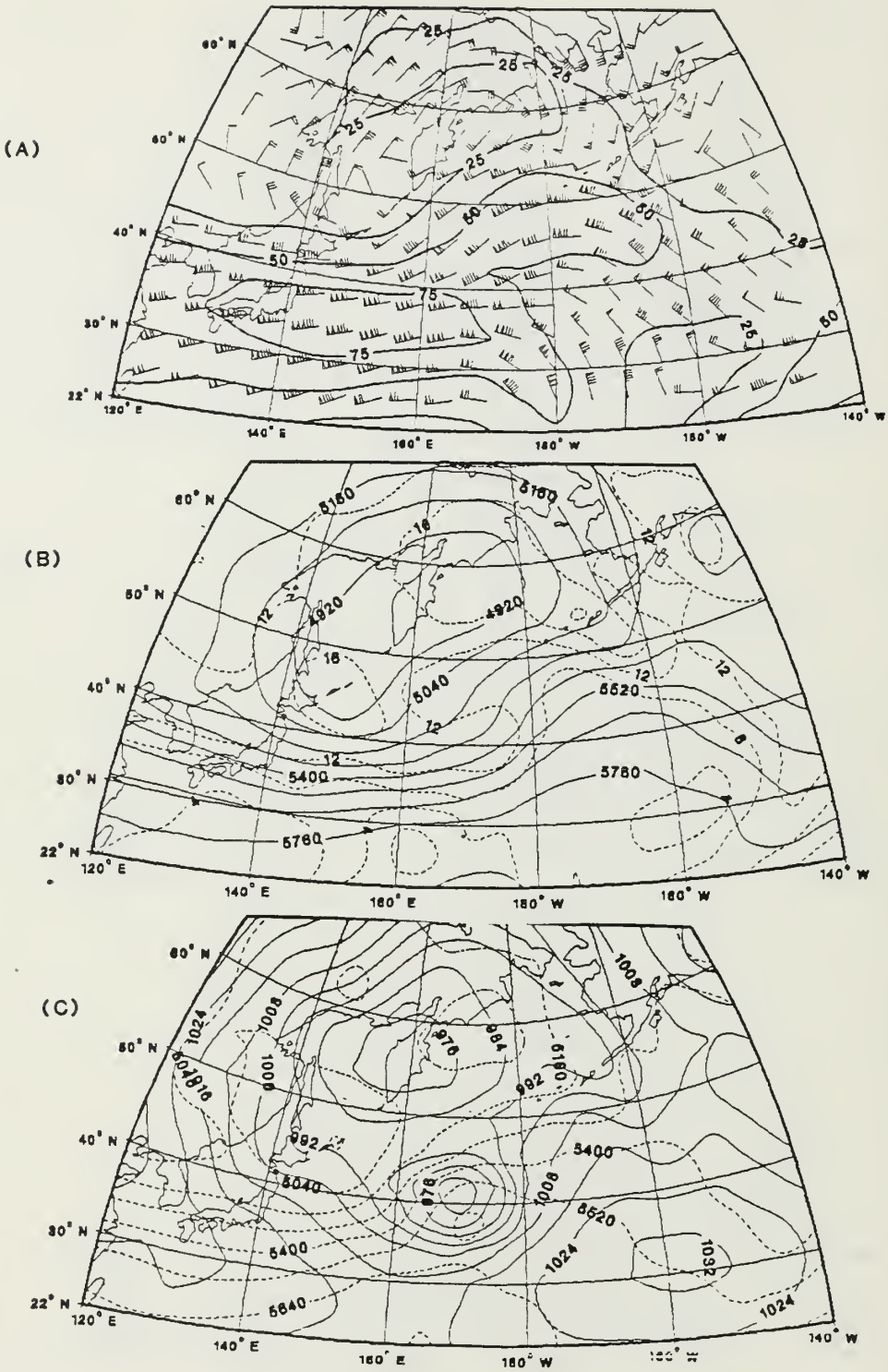

Figure 11. As in Figure 2 except for NOSAT Prognosis 0000 GMT 14 January

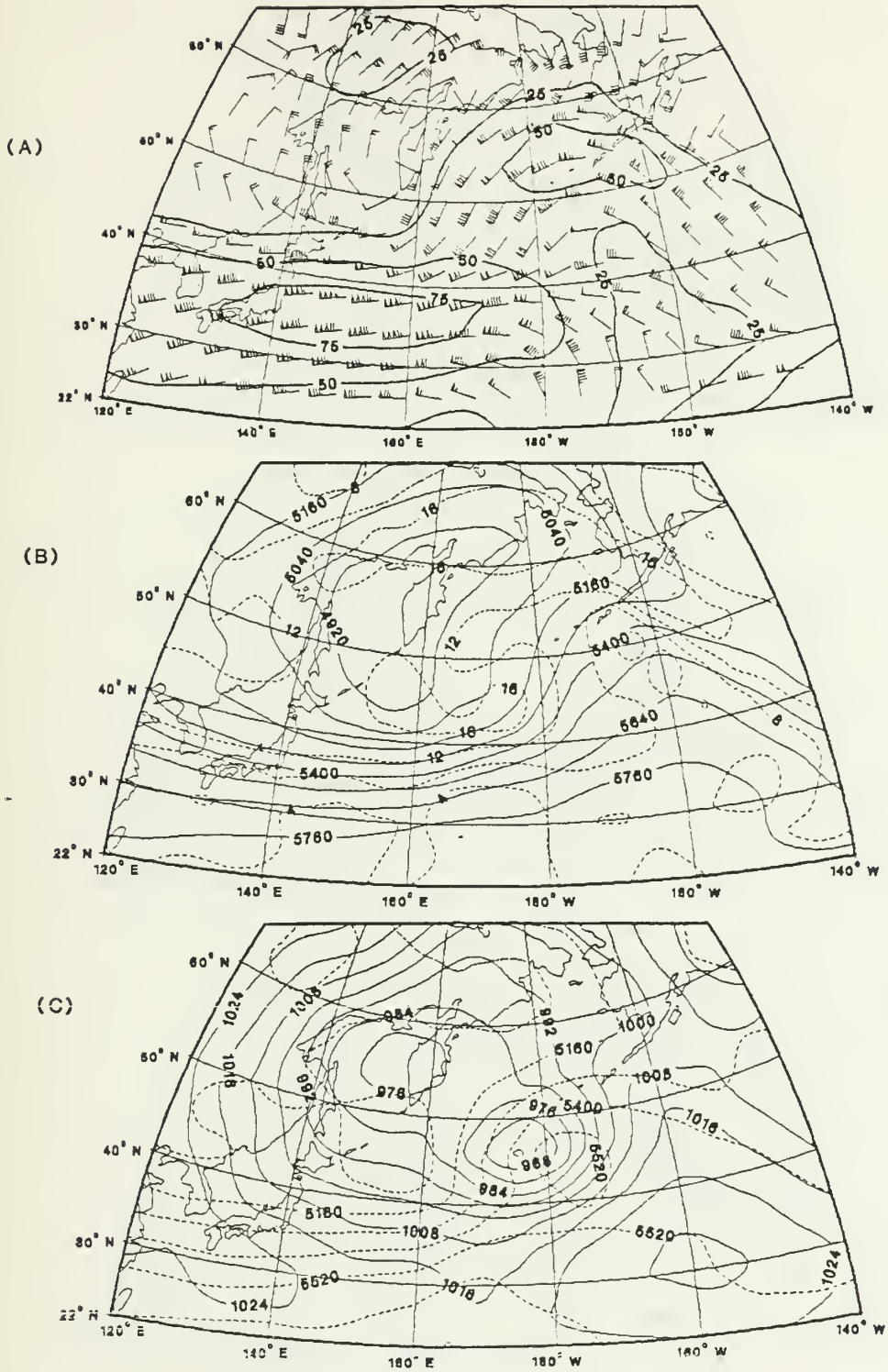

Figure 12. As in Figure 2 except for SAT Prognosis 1200 GMT 14 January

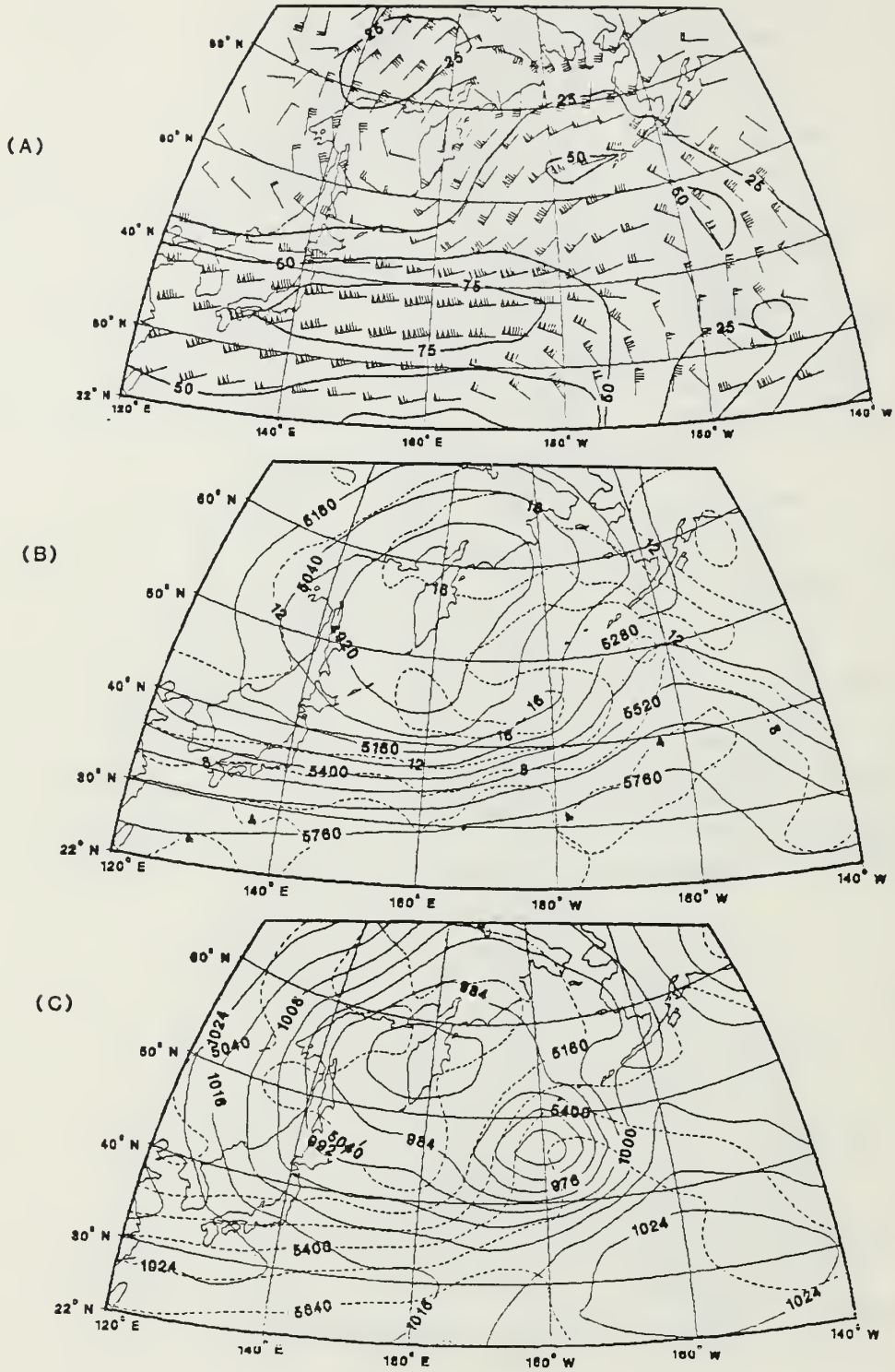

Figure 13. As in Figure 2 except for NOSAT Prognosis 1200 GMT 14 January

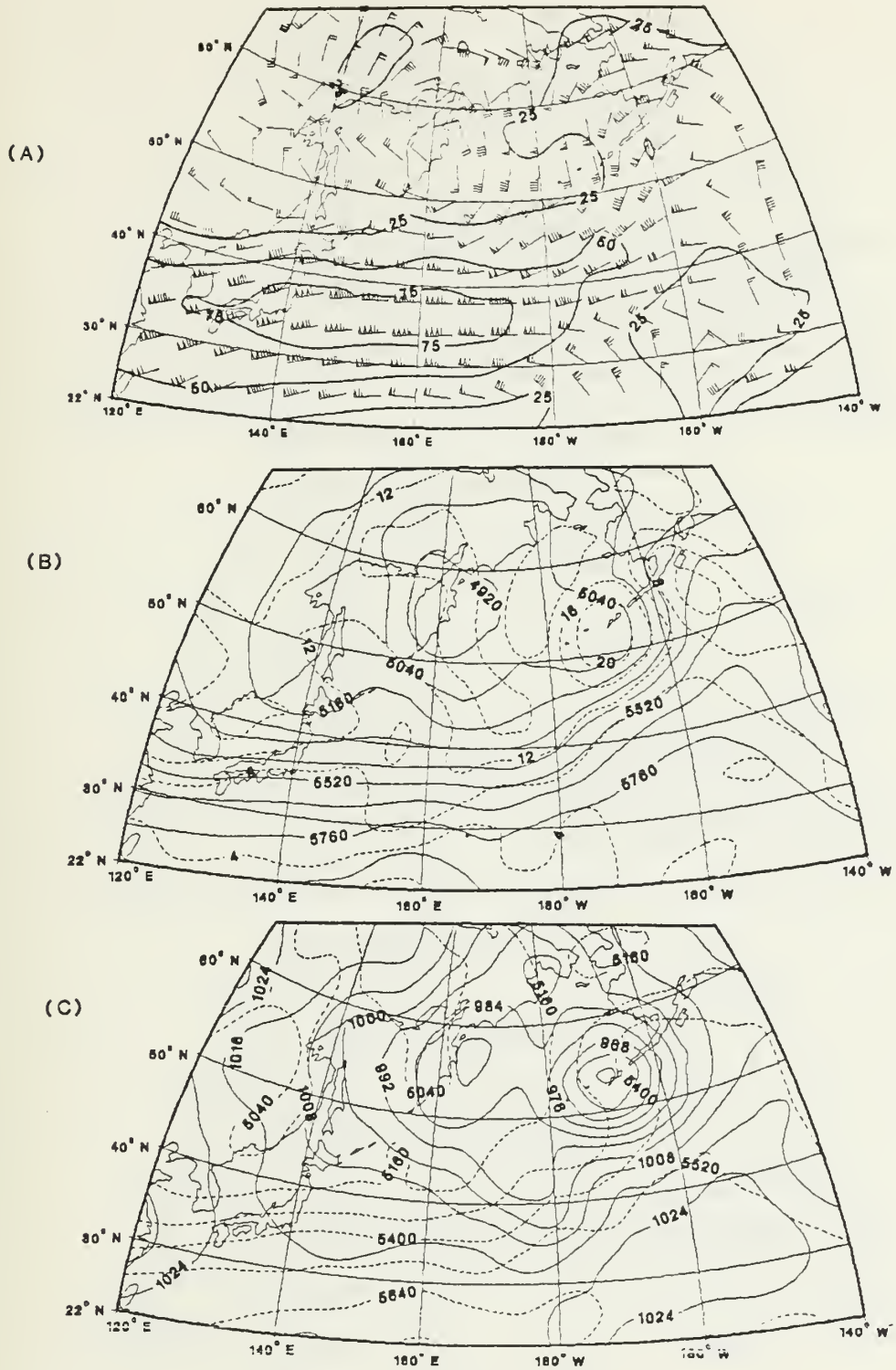

Figure 14. As in Figure 2 except for GLAS Analysis 0000 GMT 15 January

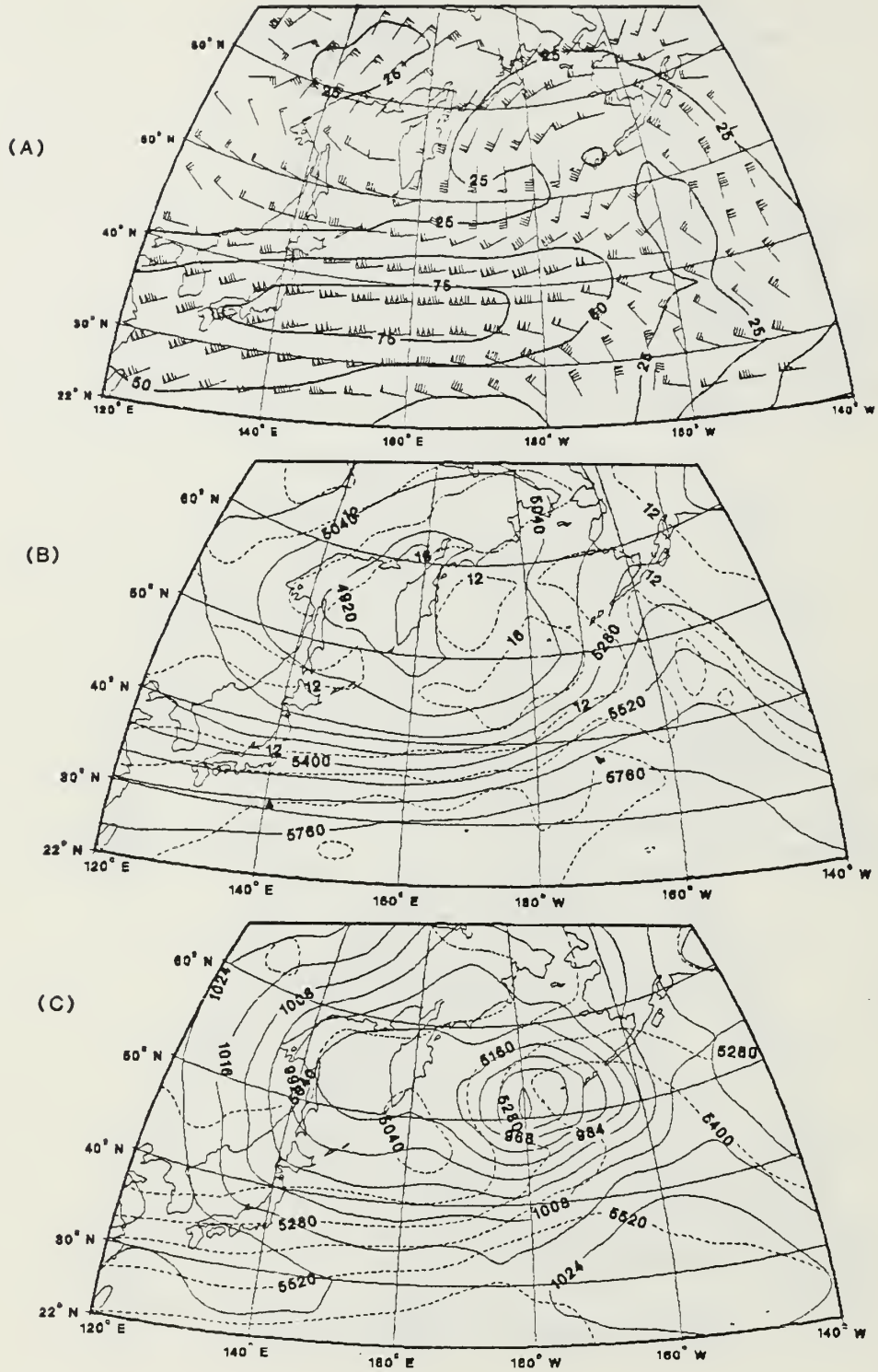

Figure 15. As in Figure 2 except for SAT Prognosis 0000 GMT 15 January

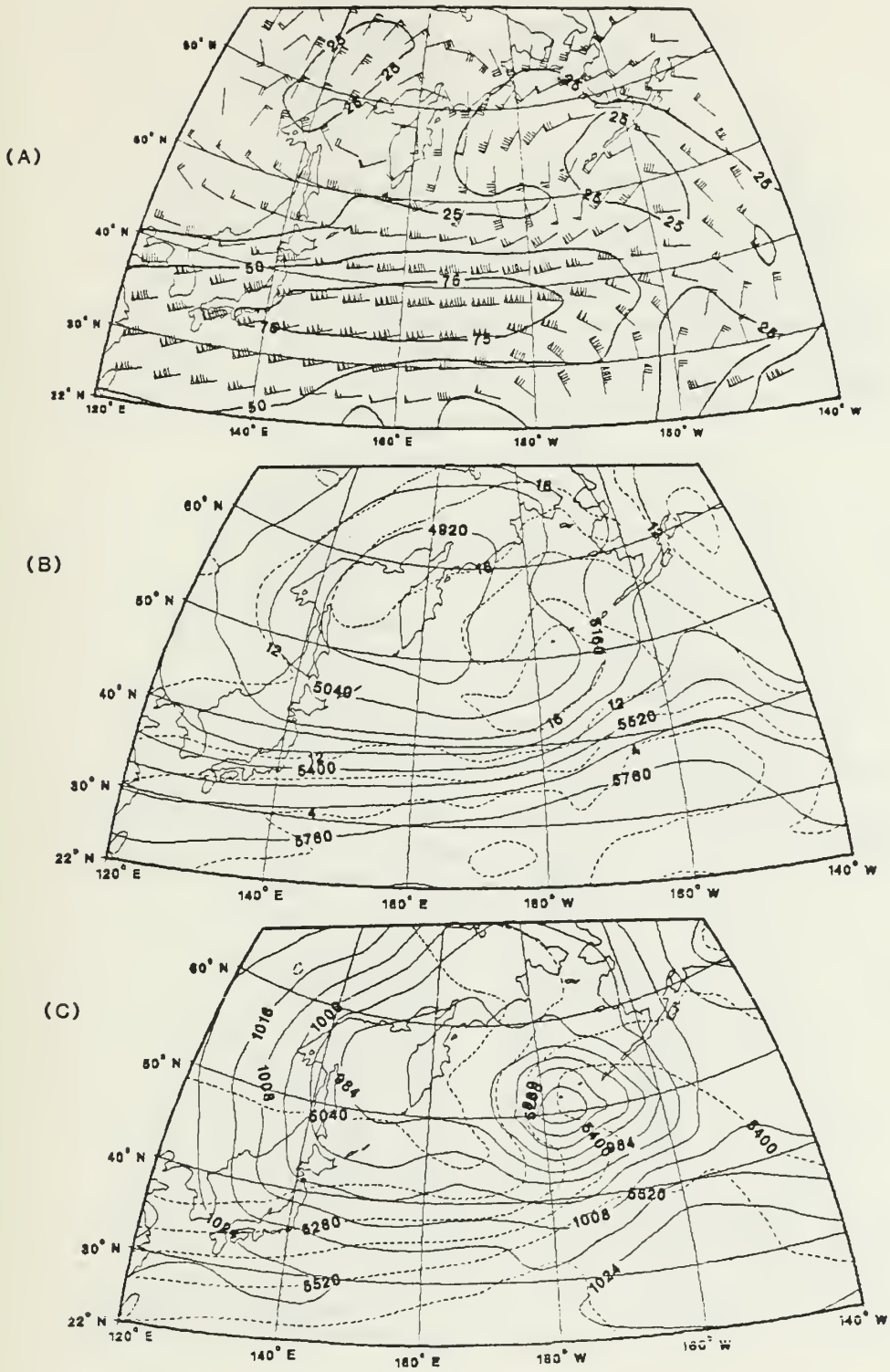

Figure 16. As in Figure 2 except for NOSAT Prognosis 0000 GMT 15 January

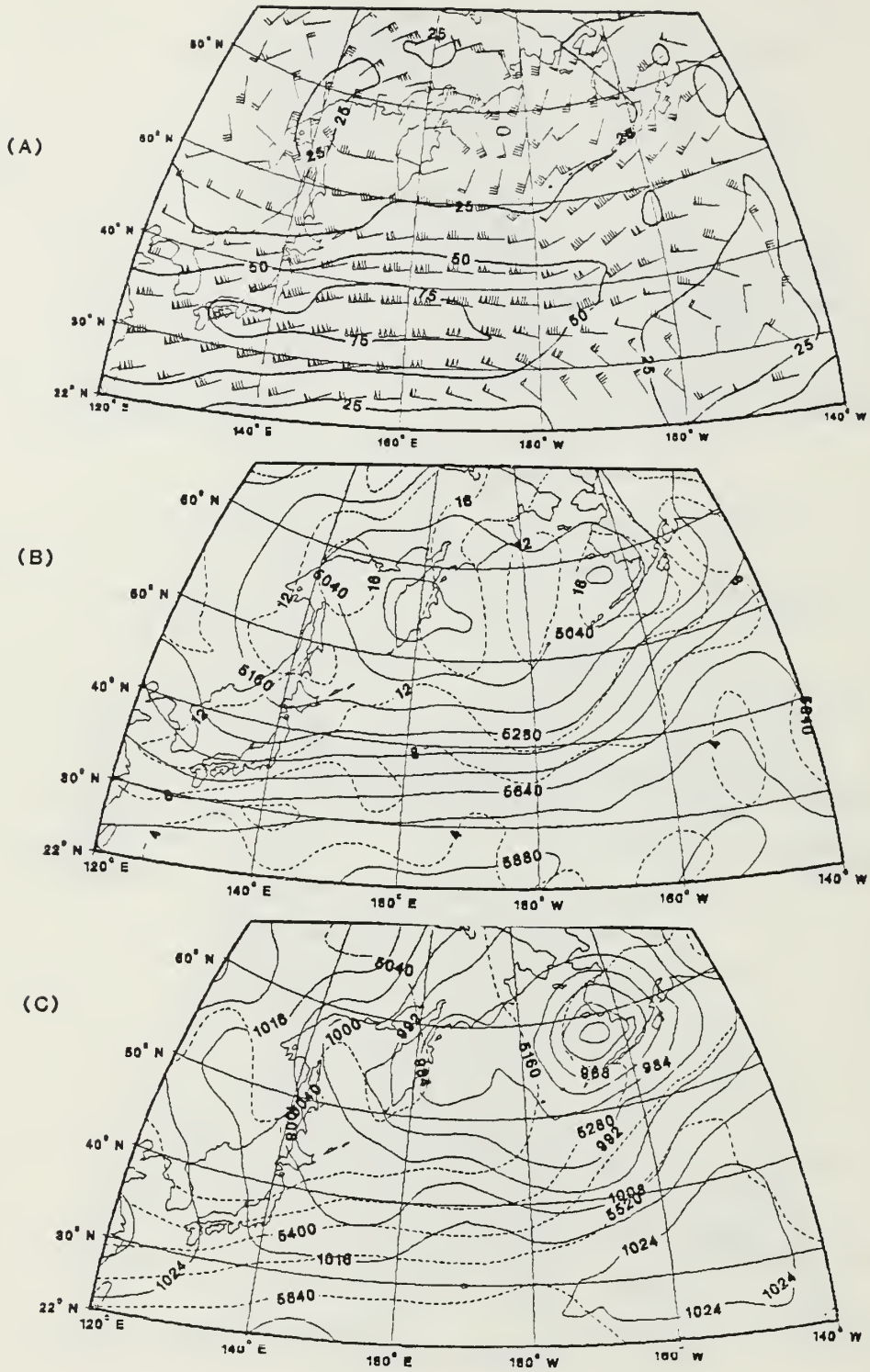

Figure 17. As in Figure 2 except for GLAS Analysis 1200 GMT 15 January

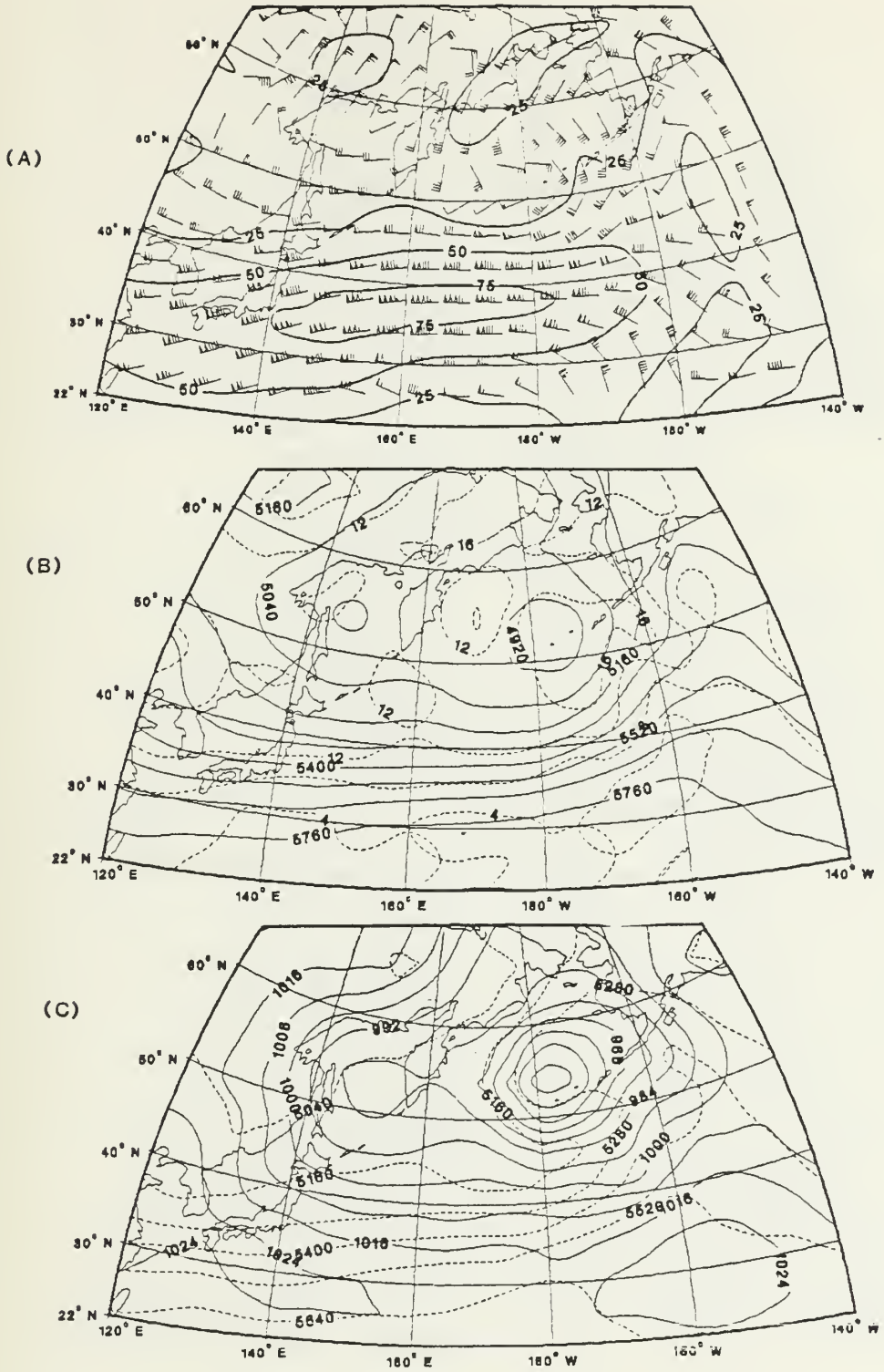

Figure 18. As in Figure 2 except for SAT Prognosis 1200 GMT 15 January

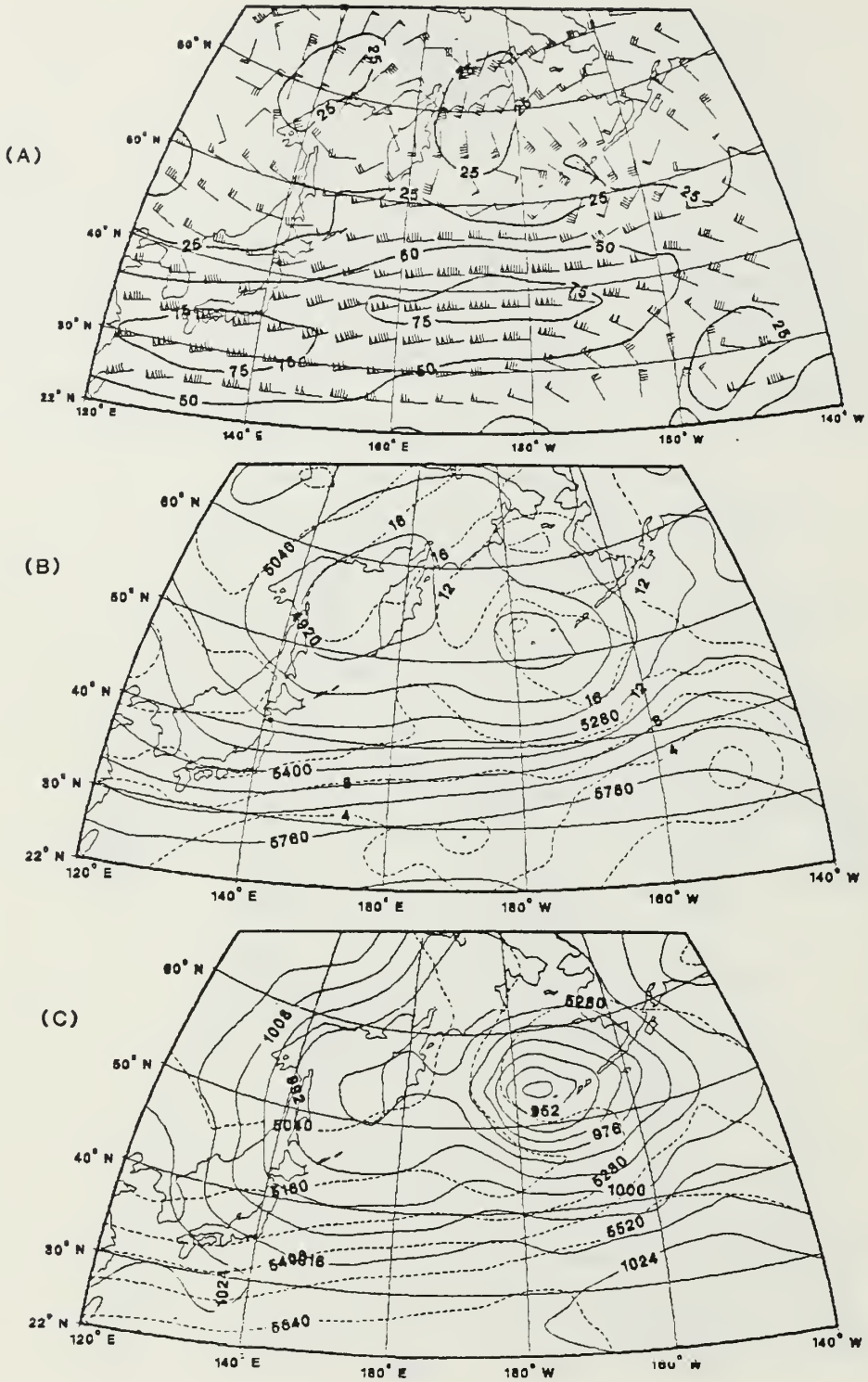

Figure 19. As in Figure 2 except for NOSAT Prognosis 1200 GMT 15 January

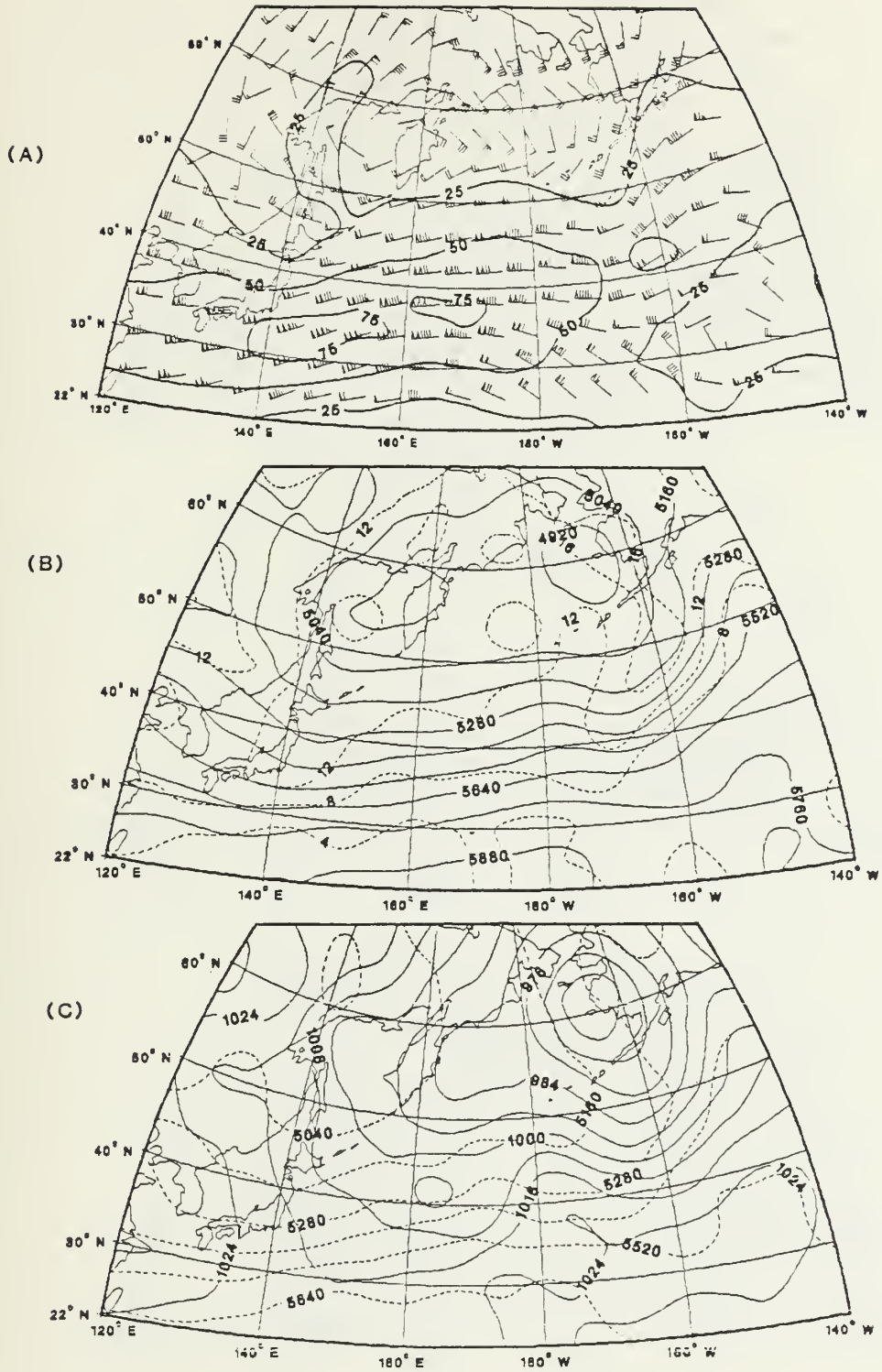

Figure 20. As in Figure 2 except for GLAS Analysis 0000 GMT 16 January

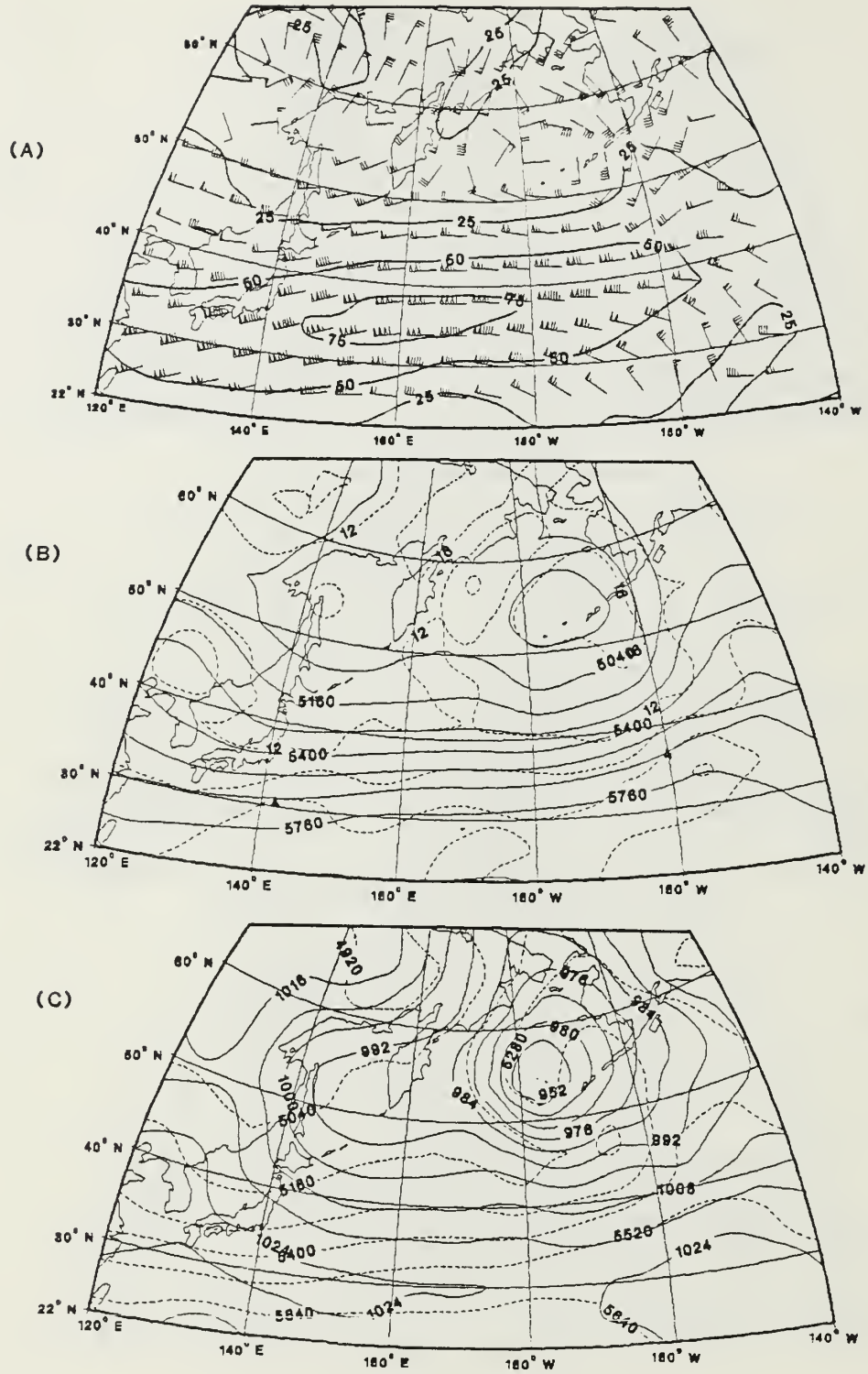

Figure 21. As in Figure 2 except for SAT Prognosis 0000 GMT 16 January

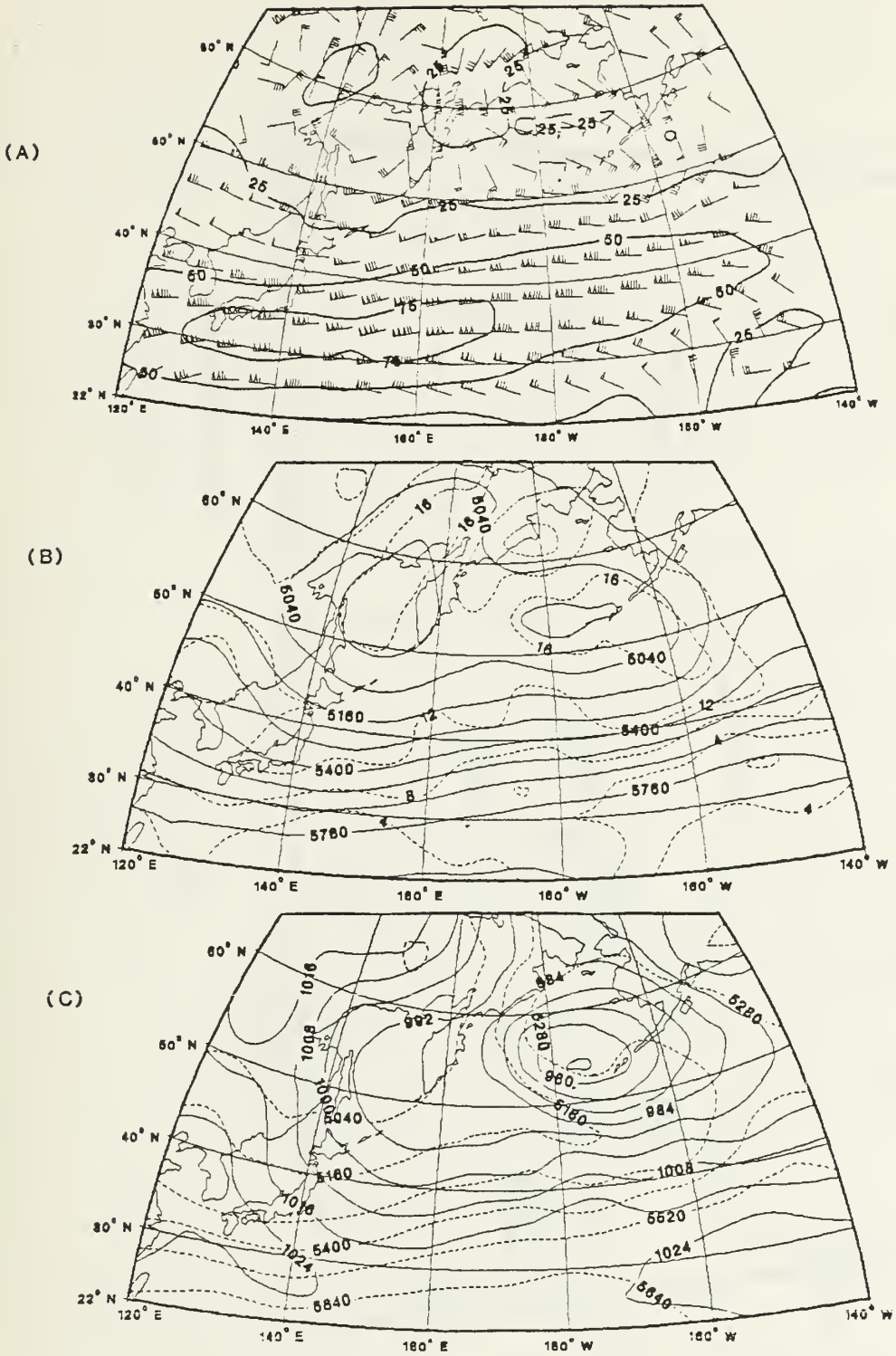

Figure 22. As in Figure 2 except for NOSAT Prognosis 0000 GMT 16 January

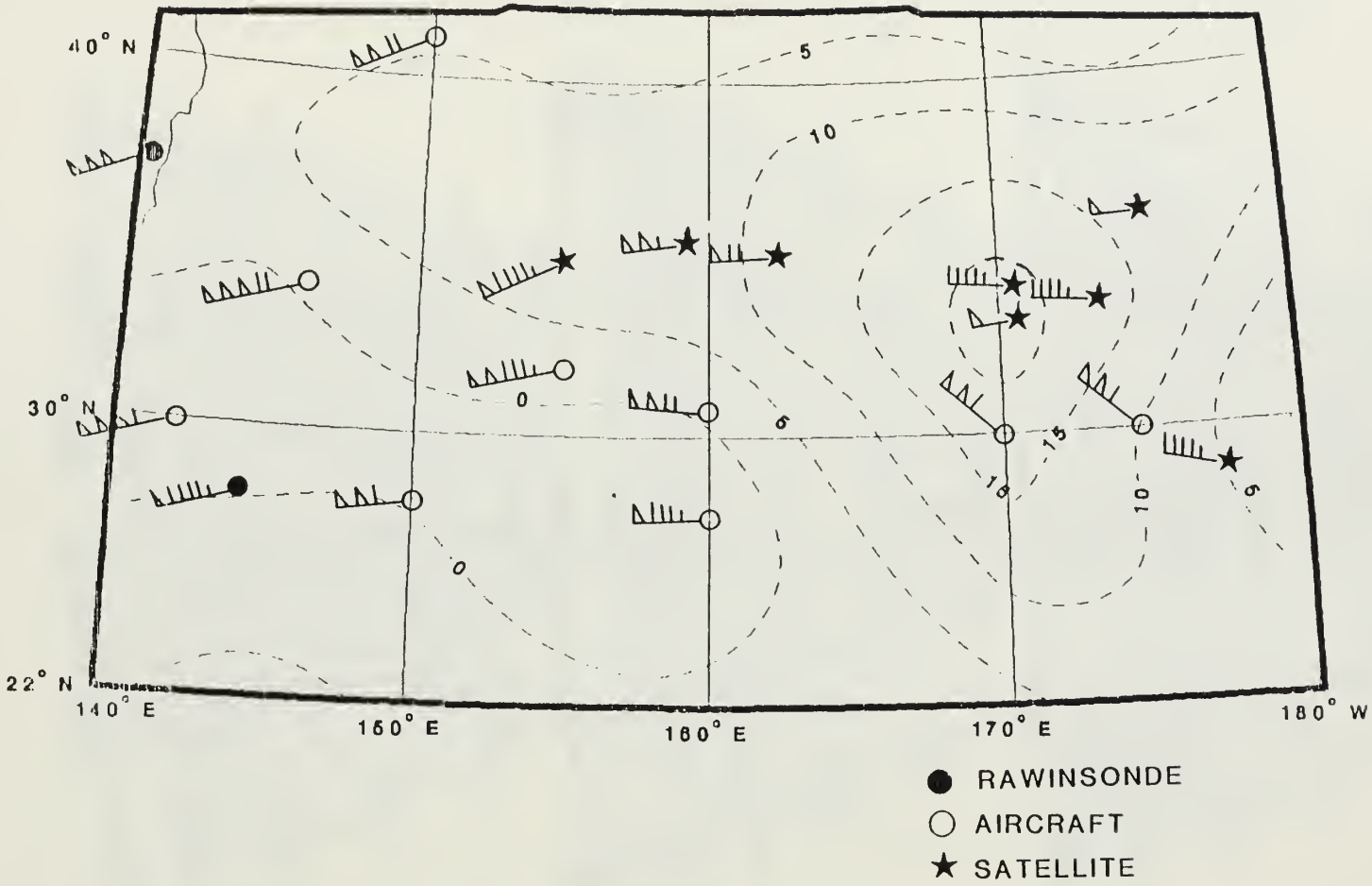

Figure 23. NOSAT-SAT 250 mb Isotach Difference (Dashed) in m/s Superposed on Observed Wind Reports for 00 GMT 13 January

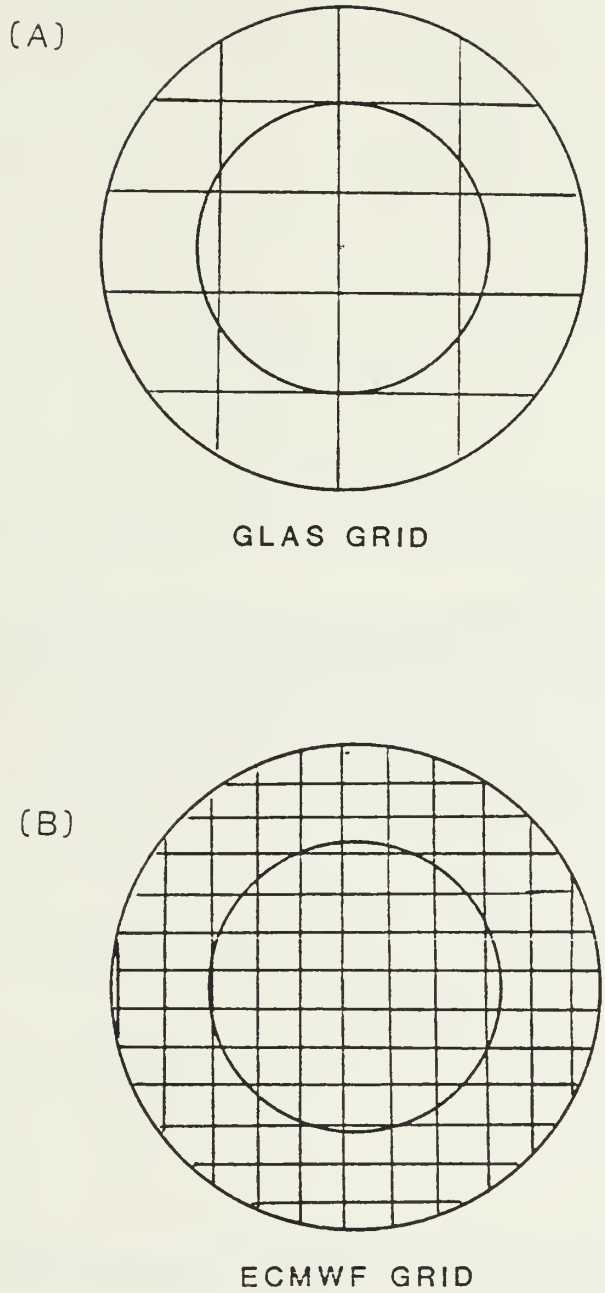

Figure 24. Analyses Grids Superposed over Radius 6 and 10 Degree Budget Volumes (A) GLAS Analysis Grid (4 × 5 Degrees) (B) ECMWF Analysis (1.875 × 1.875 Degrees).

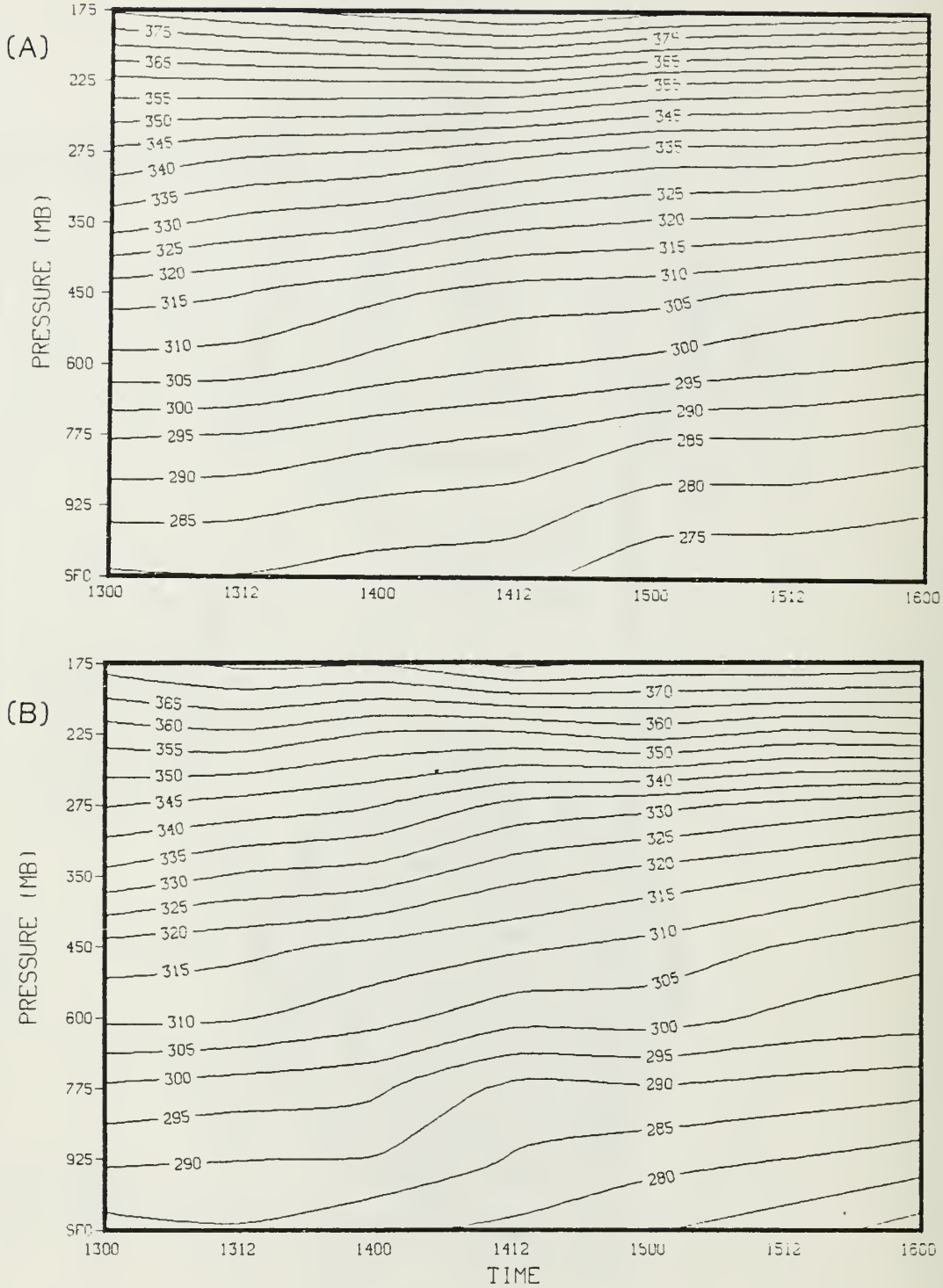

Figure 25. Analyses Area-Averaged Potential Temperature Time Sections (A) GLAS (B) ECMWF. Values are in Degrees Kelvin. Time 1300 Refers to 00 GMT 13 January.

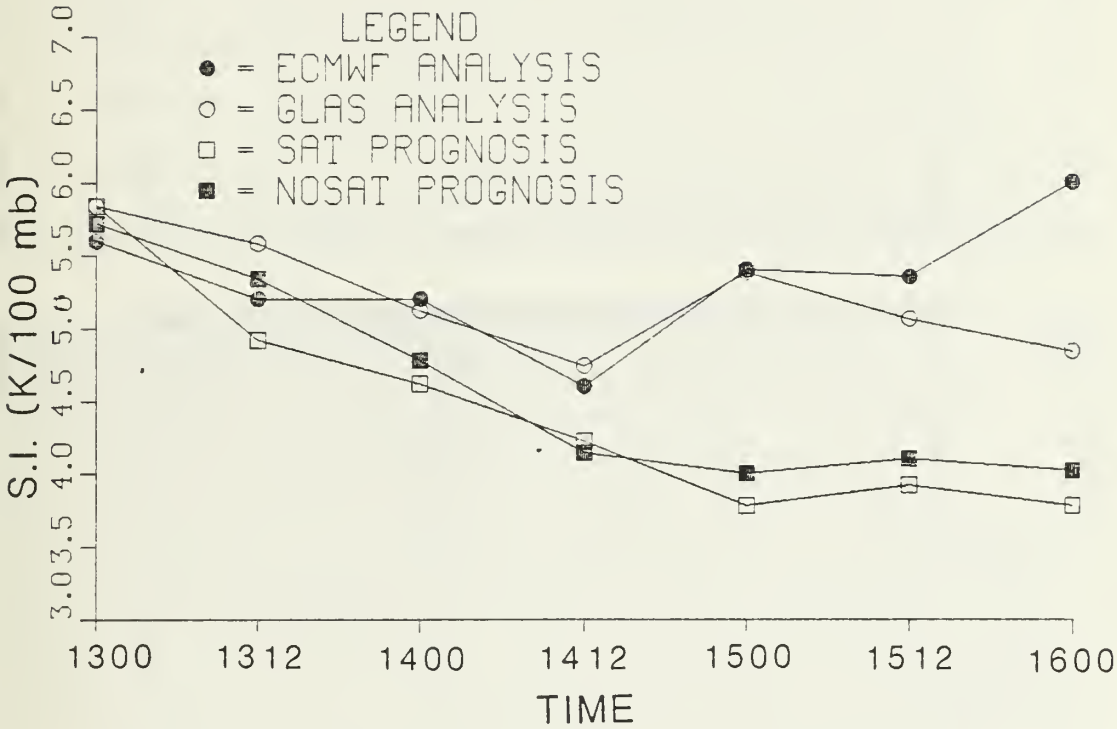

Figure 26. Stability Index. Values in Degrees Kelvin/ 100 mb. Time 1300 Refers to 00 GMT 13 January.

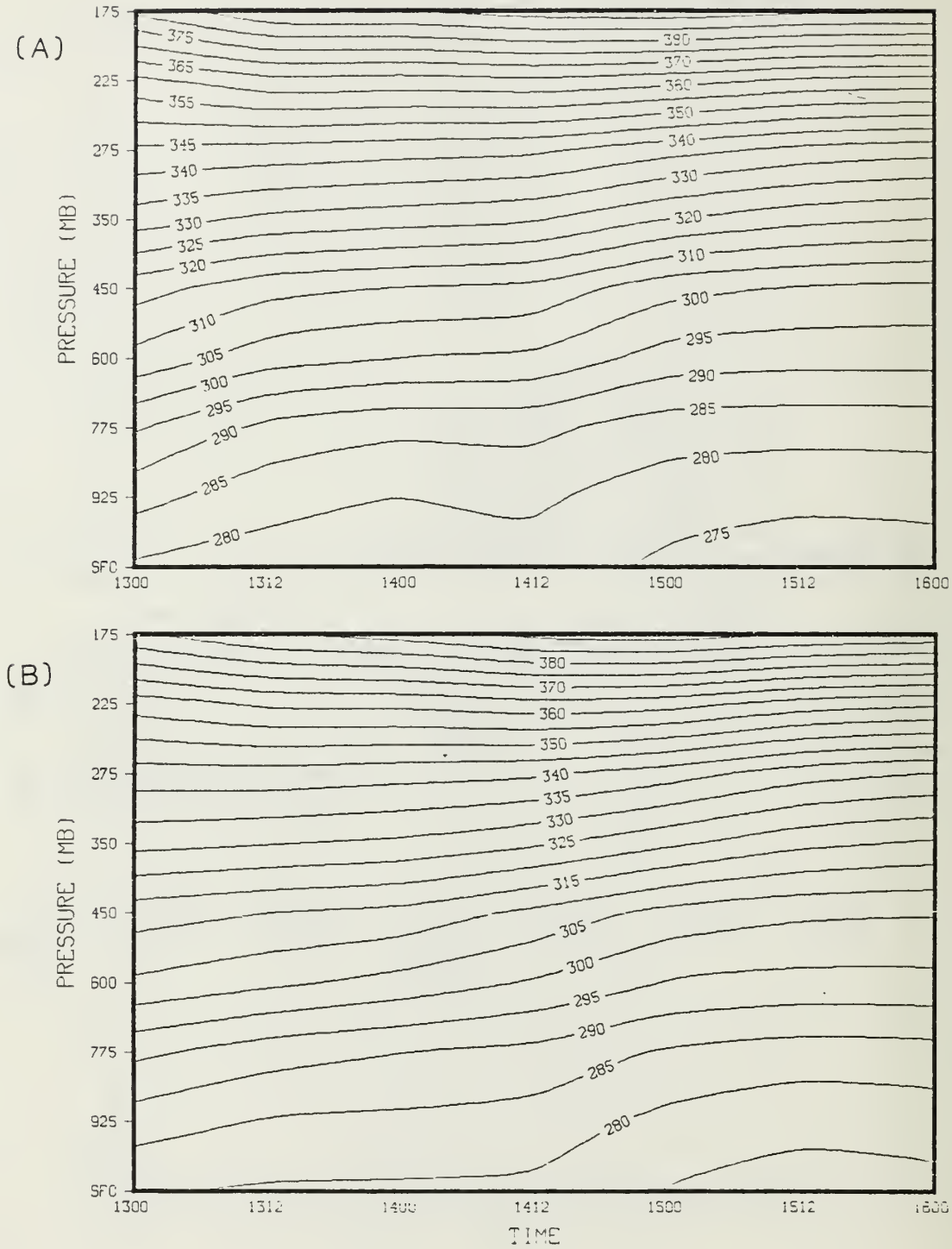

Figure 27. Prognoses Area-Averaged Potential Temperature Time Sections (A) SAT (B) NOSAT. As in Figure 25.

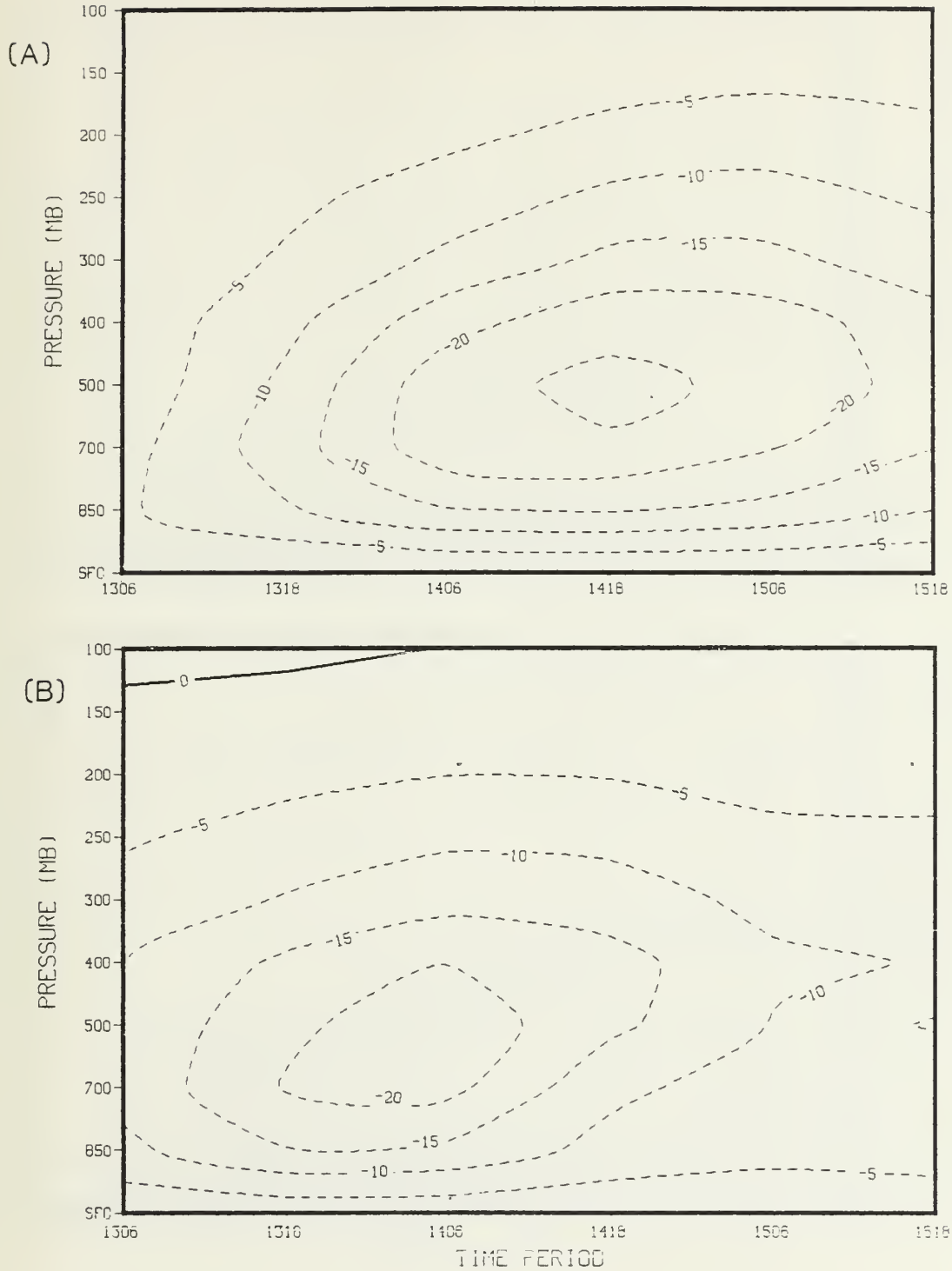

Figure 28. Analyses Kinematic Vertical Velocities (A) GLAS (B) ECMWF. Units are in mb/1000-sec. Time 1300 Refers to 00 GMT 13 January.

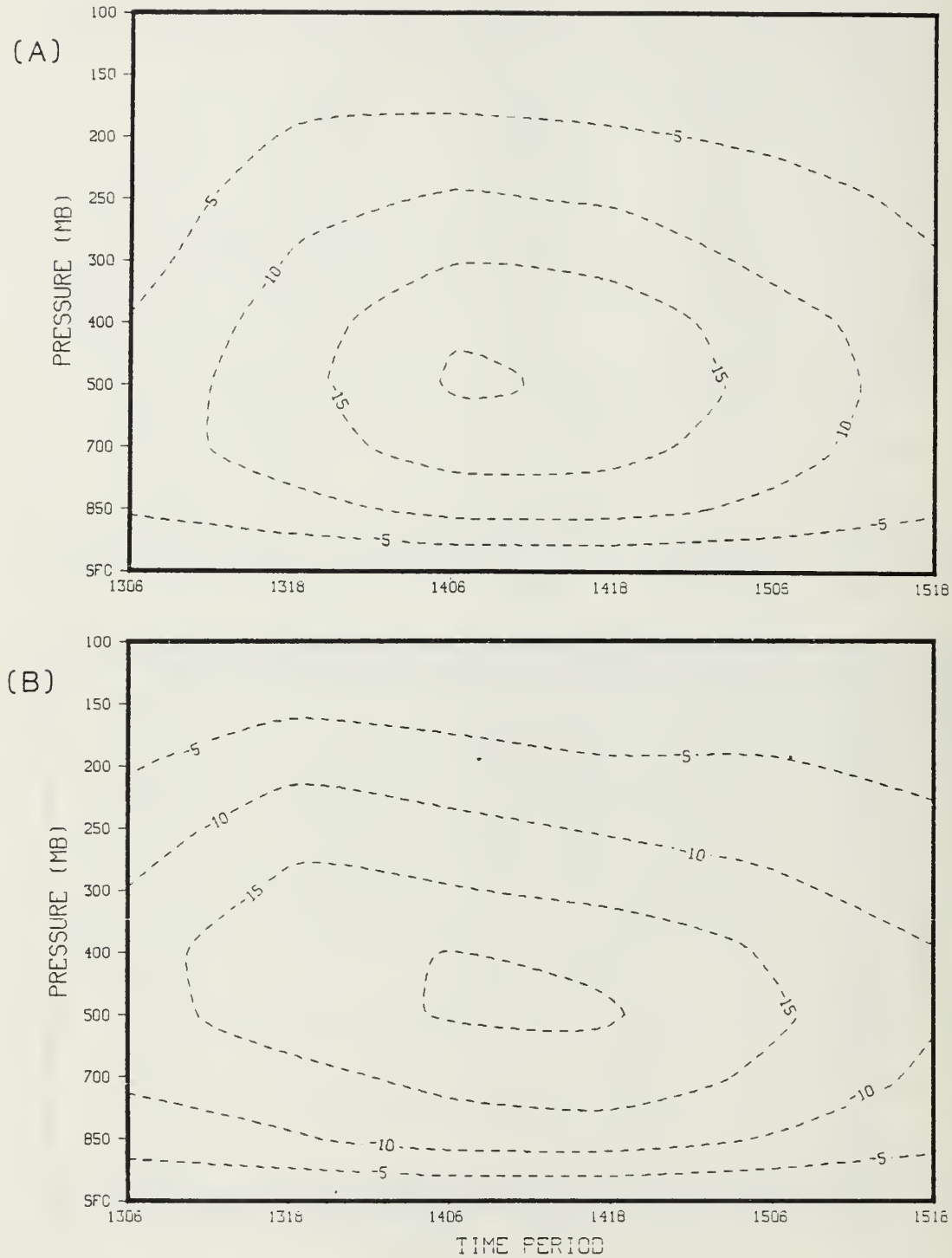

Figure 29. Prognoses Kinematic Vertical Velocities (A) SAT (B) NOSAT. As in Figure 28.

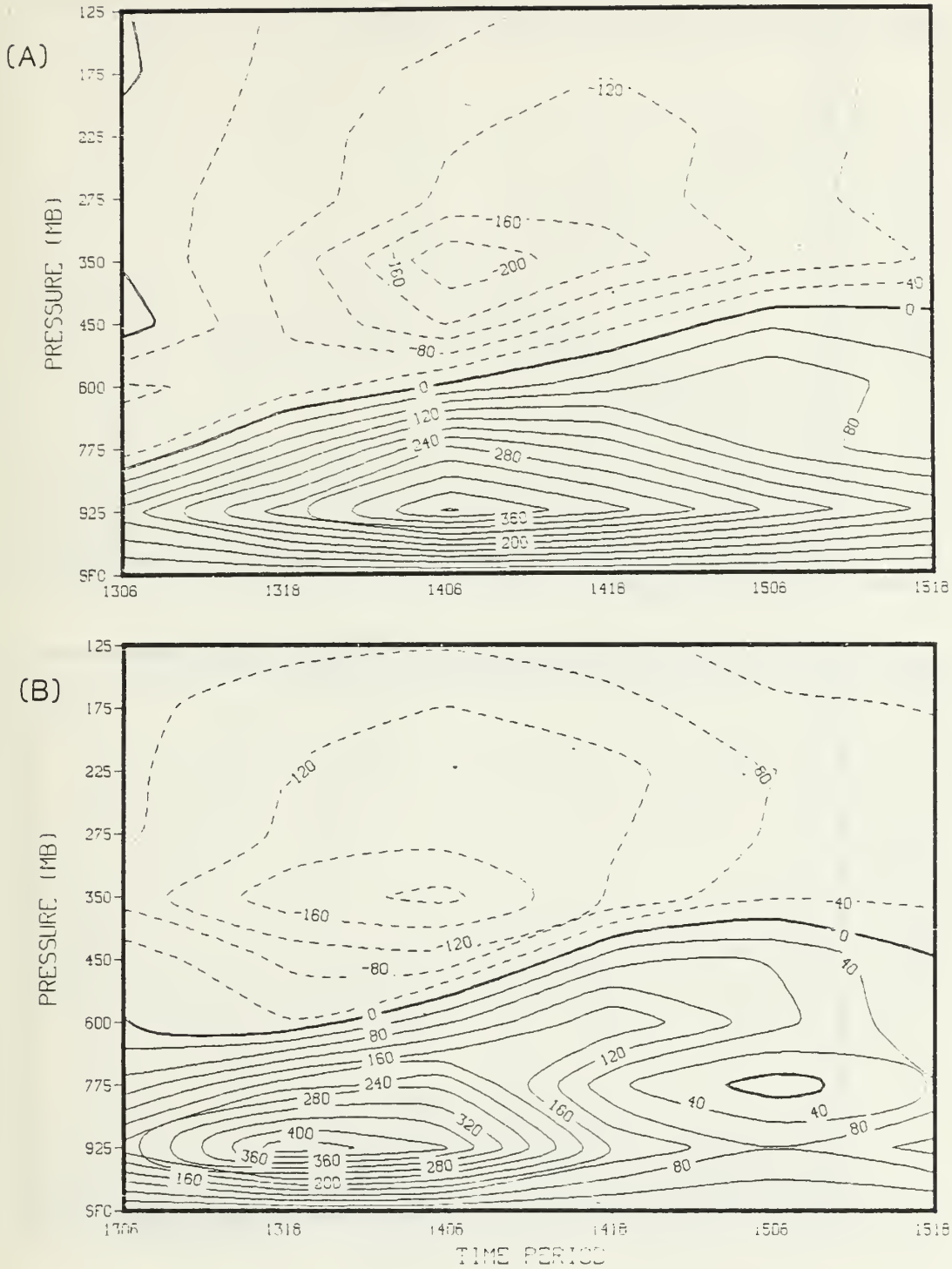

Figure 30. Analyses Corrected Lateral Mass Transport Time Sections (A) GLAS (B) ECMWF. Contour Interval is 40 X (10**11). Negative Values (DASHED) Indicate Flux out of the Volume. Units are in gm/sec-100 mb. Period 1306 Refers to 00-12 GMT 13 January.

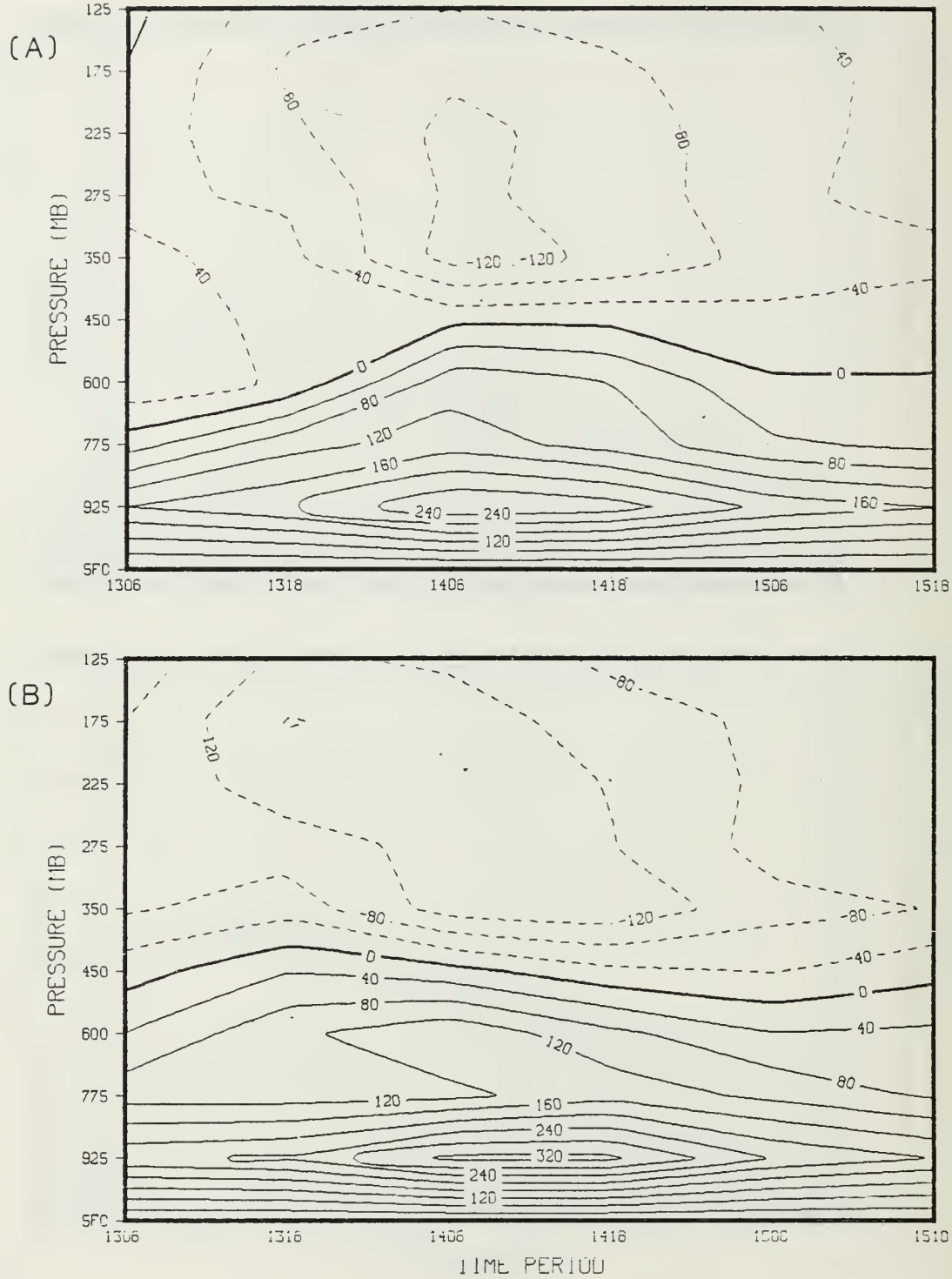

Figure 31. Prognoses Corrected Lateral Mass Transport Time Sections (A) SAT (B) NOSAT. As in Figure 30.

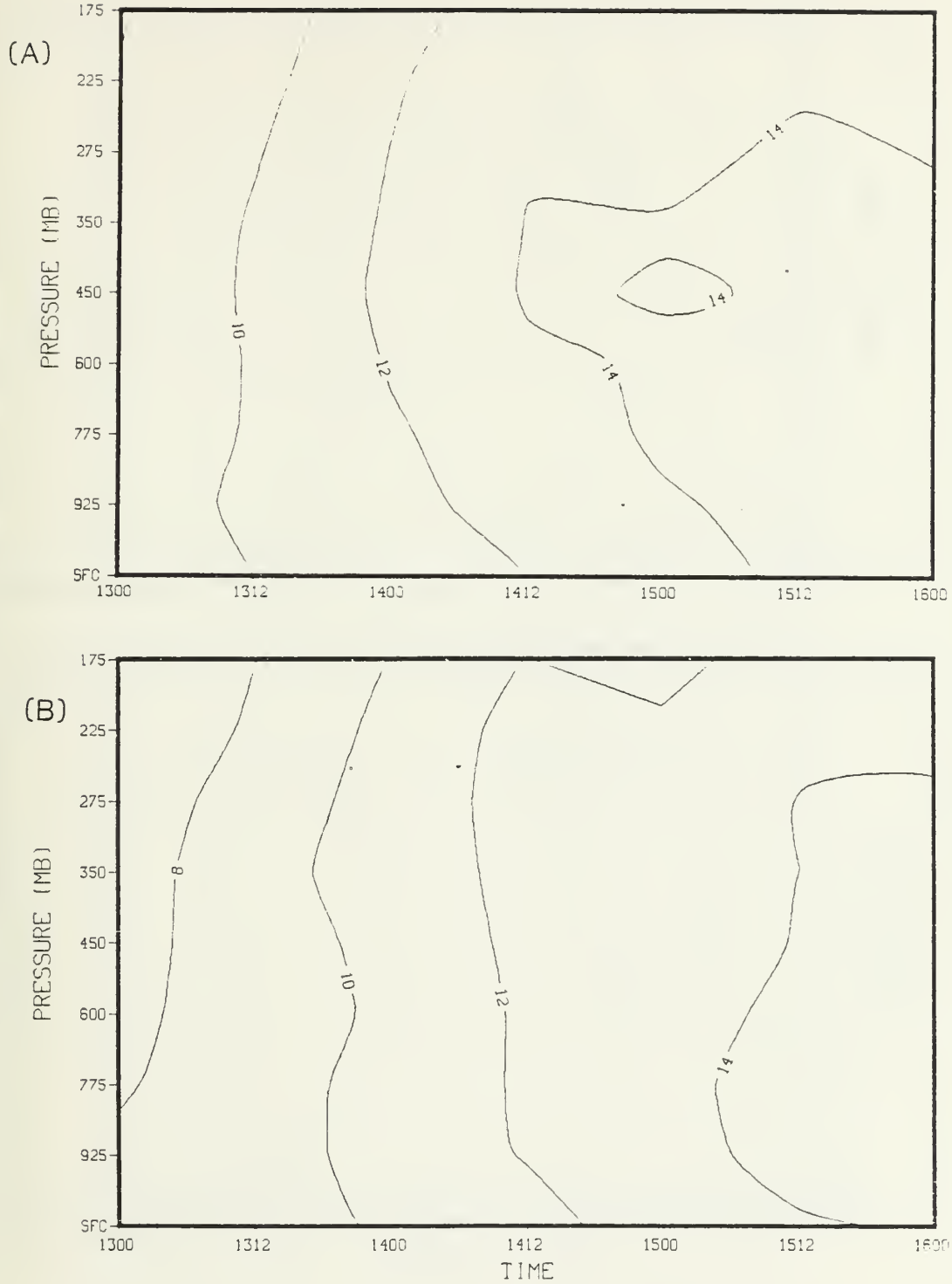

Figure 32. Analyses Area-Averaged Absolute Vorticity Vertical Time Sections (A) GLAS (B) ECMWF. Time 1300 Refers to 00 GMT 13 January. Units are 10**-5/sec.

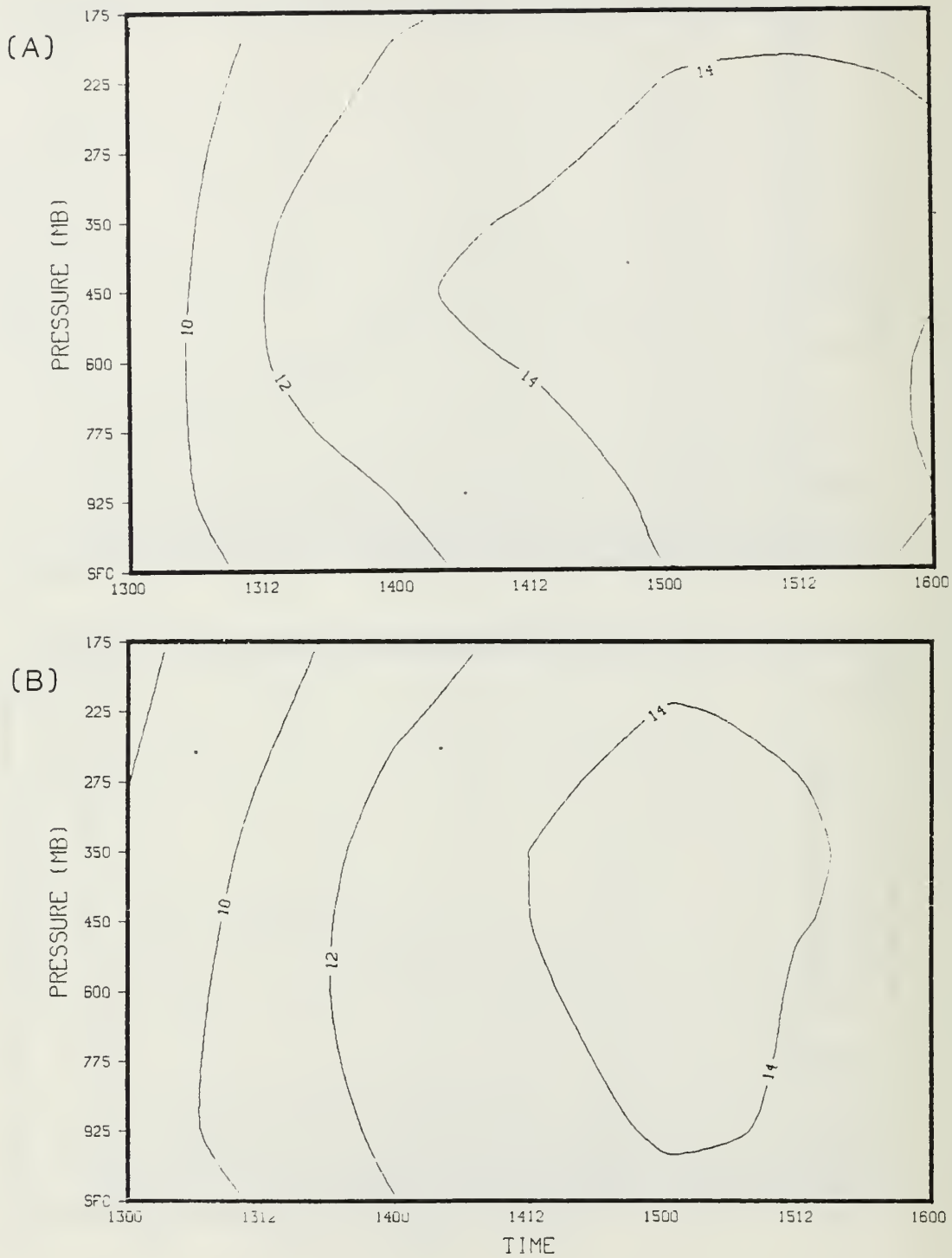

Figure 33. Prognoses Area-Averaged Absolute Vorticity Vertical Time Sections (A) SAT (B) NOSAT. As in Figure 32.

Figure 34. Analyses Absolute Vorticity Vertical Time-Tendency Sections (A) GLAS (B) ECMWF. Units are 10**-10/(sec**2). Solid Contours Reflect Vorticity Increases.

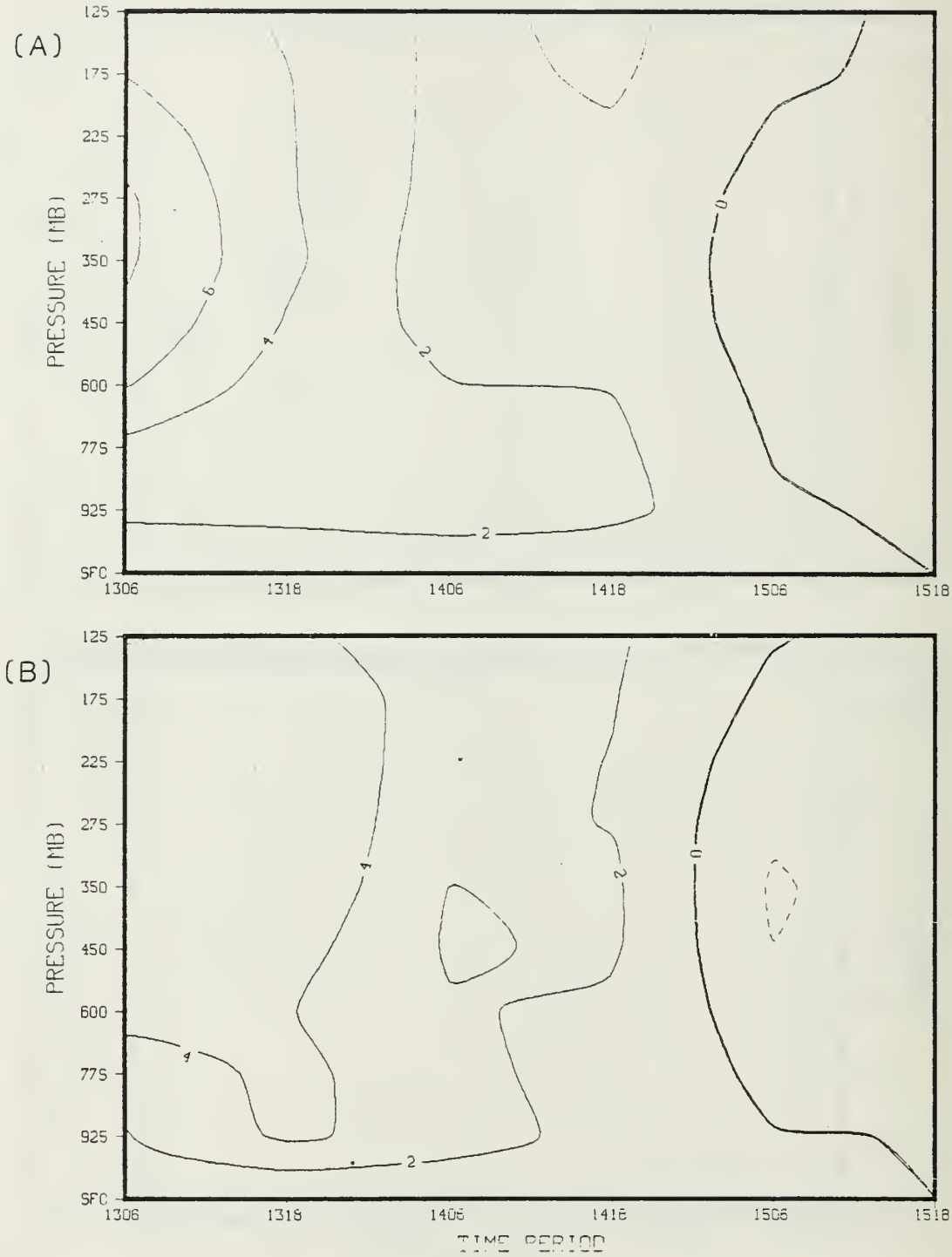

Figure 35. Prognoses Absolute Vorticity Vertical Time-Tendency Sections (A) SAT (B) NOSAT. As in Figure 34.

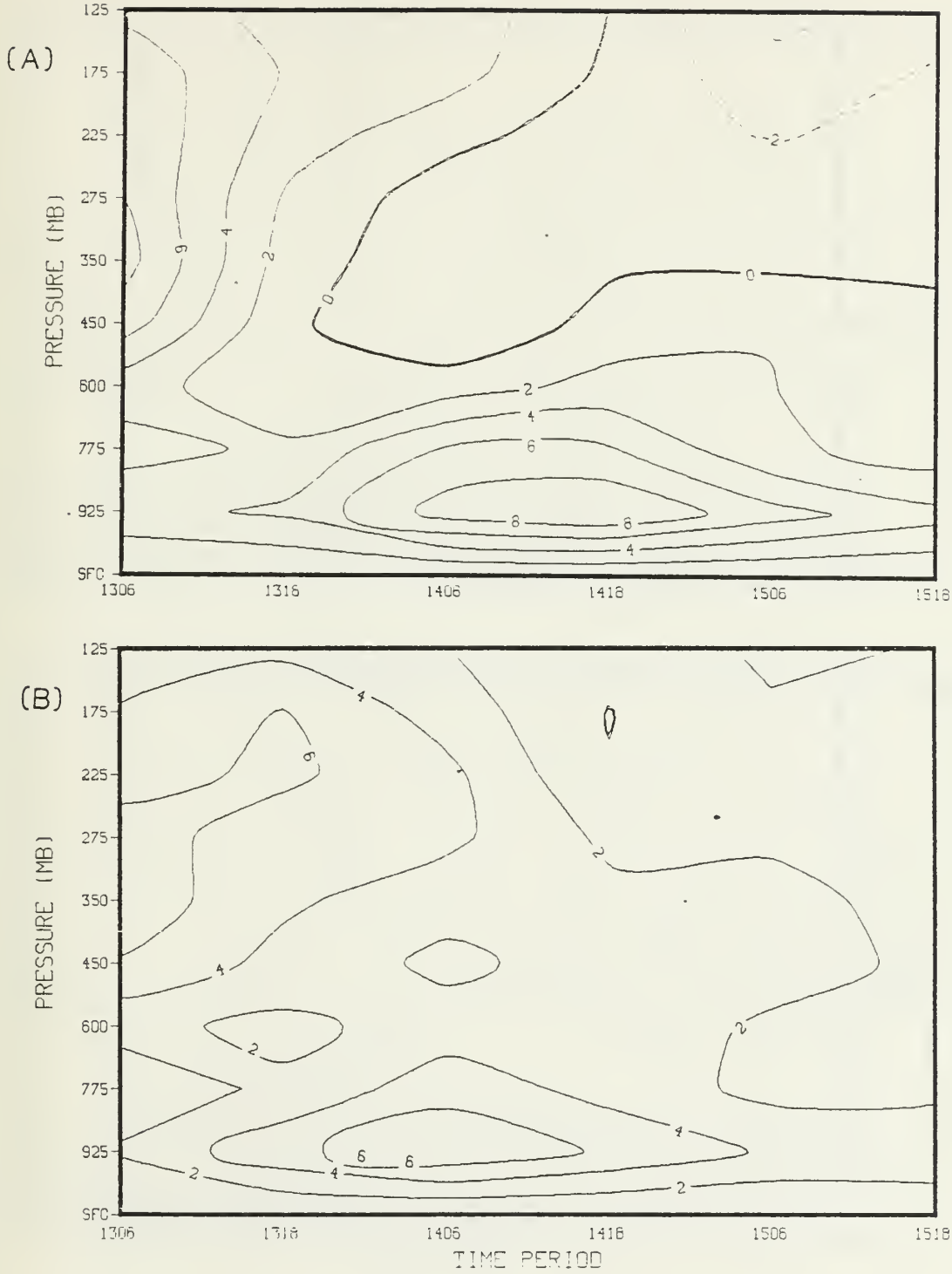

Figure 36. Analyses Lateral Vorticity Transport (A) GLAS (B) ECMWF. As in Figure 34.

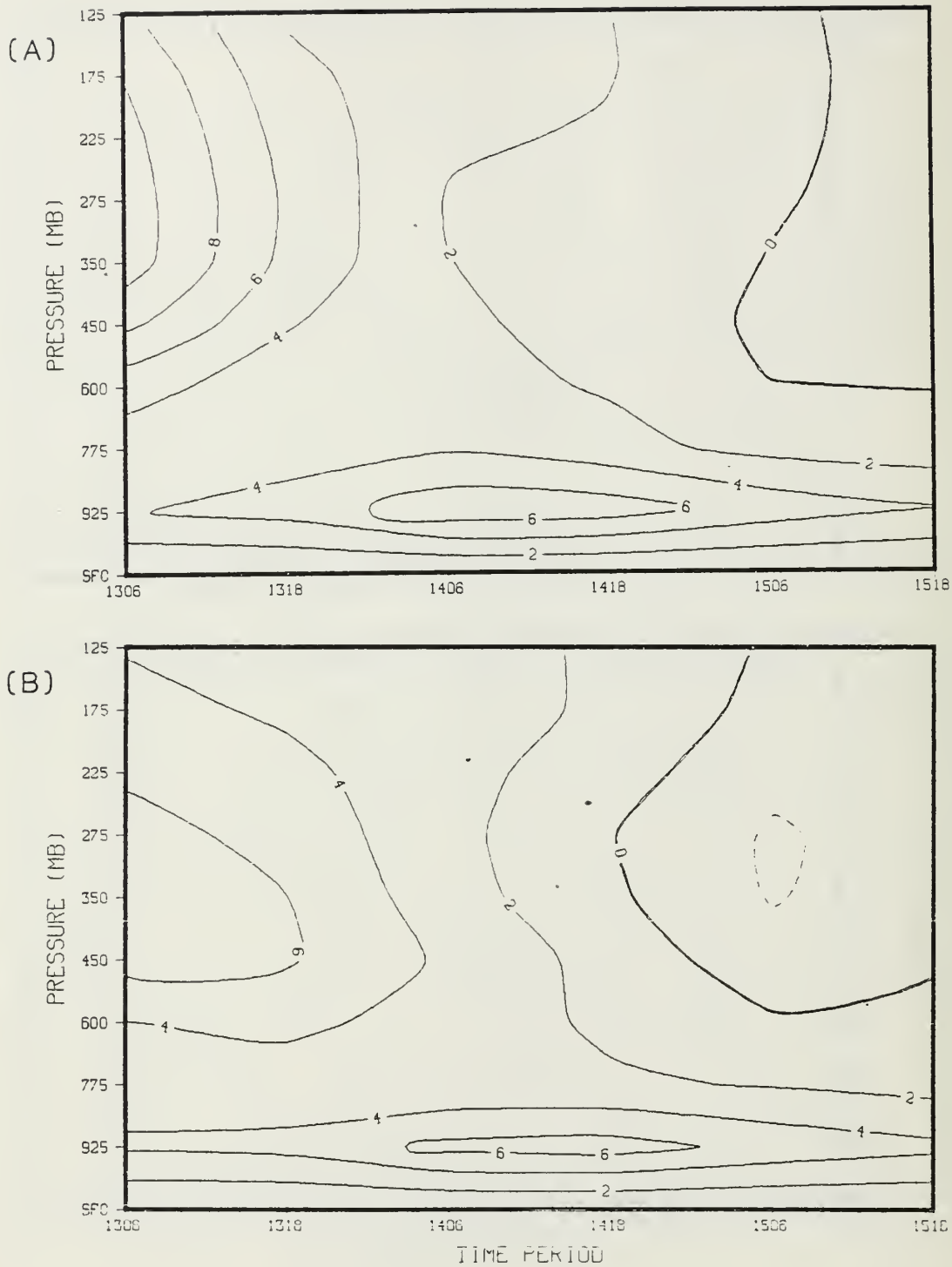

Figure 37. Prognoses Lateral Vorticity Transport (A) SAT (B) NOSAT. As in Figure 34.

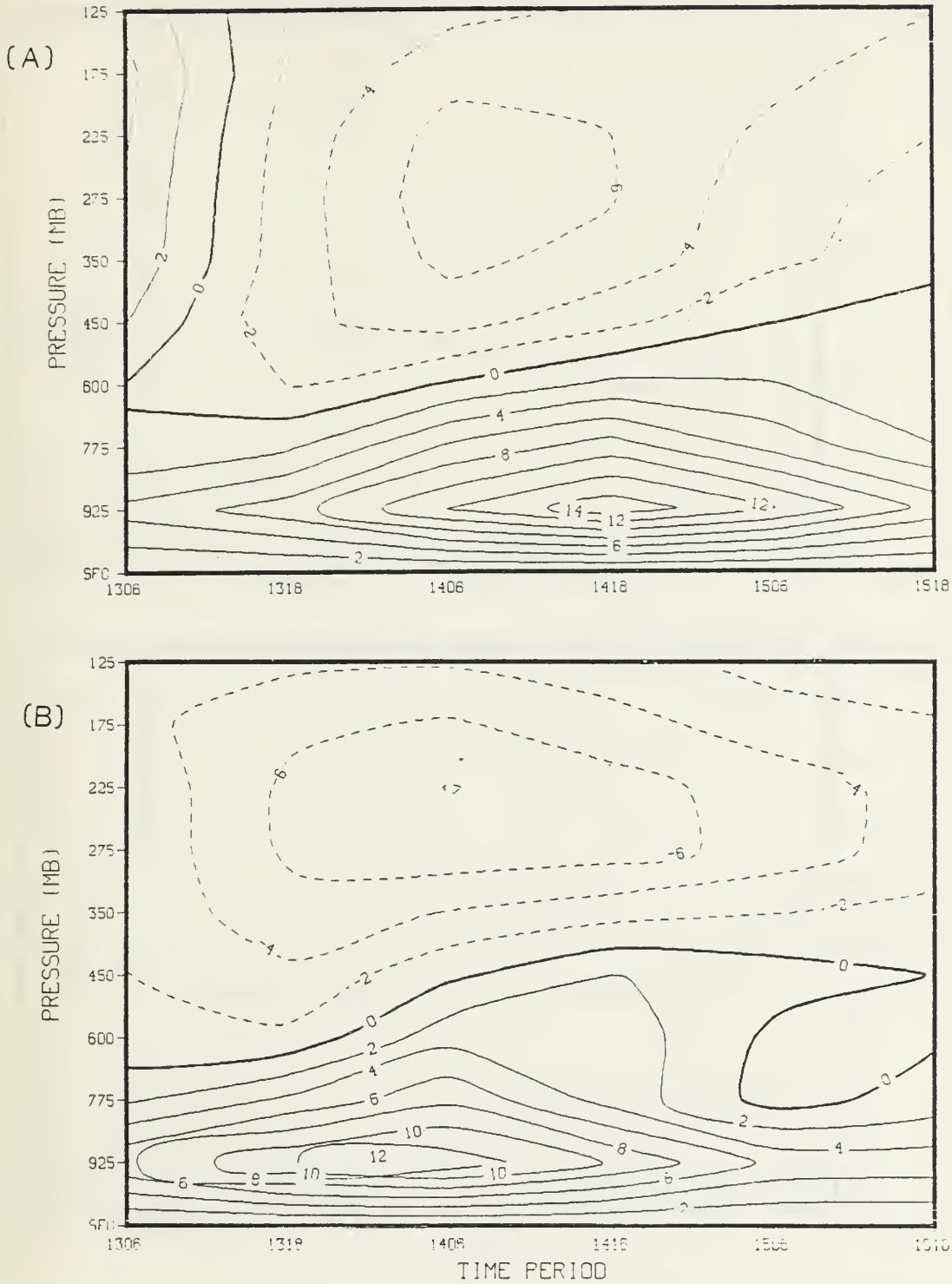

Figure 38. Analyses Lateral Vorticity Divergence (A) GLAS (B) ECMWF. As in Figure 34.

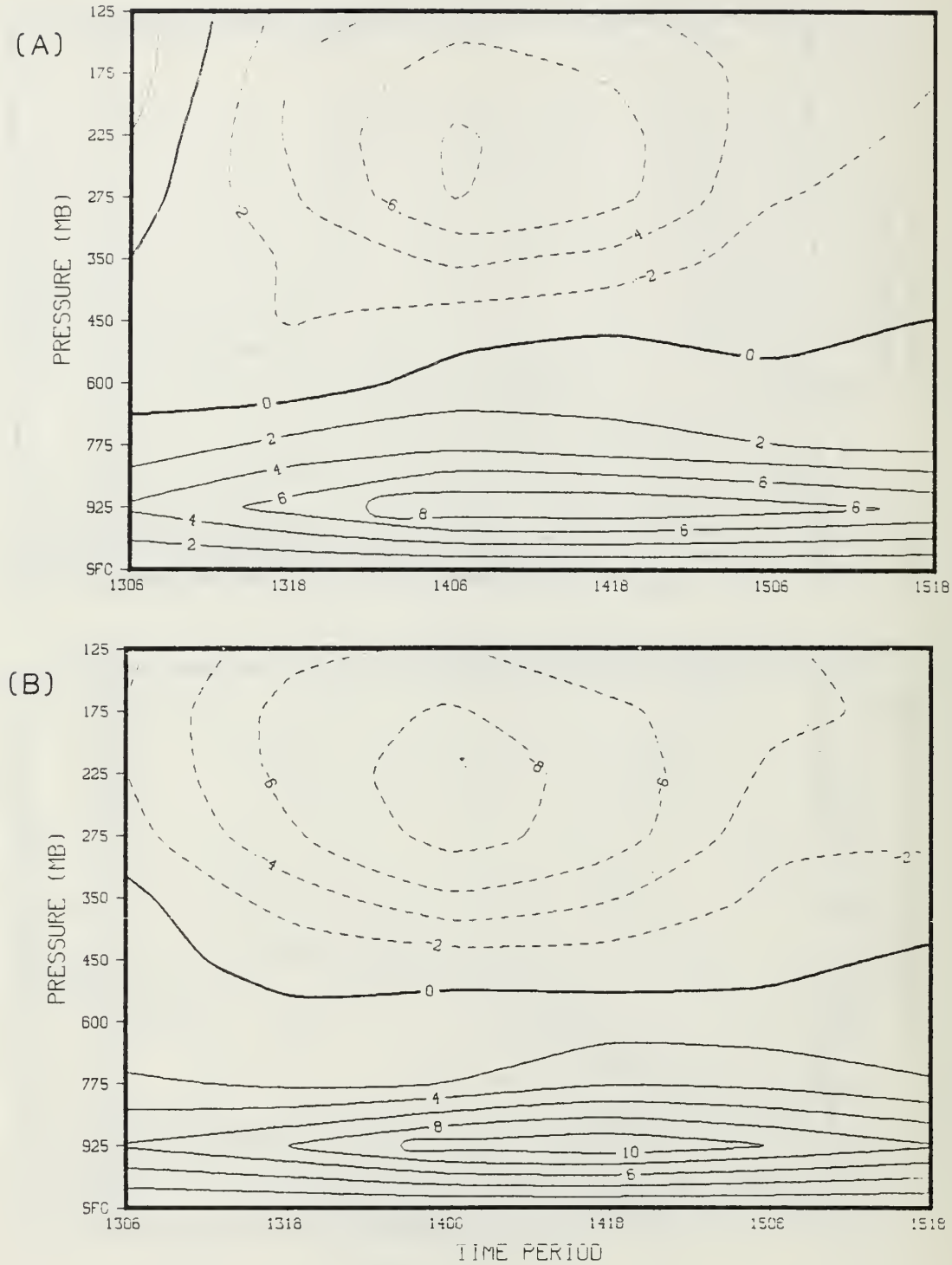

Figure 39. Prognoses Lateral Vorticity Divergence (A) SAT (B) NOSAT. As in Figure 34.

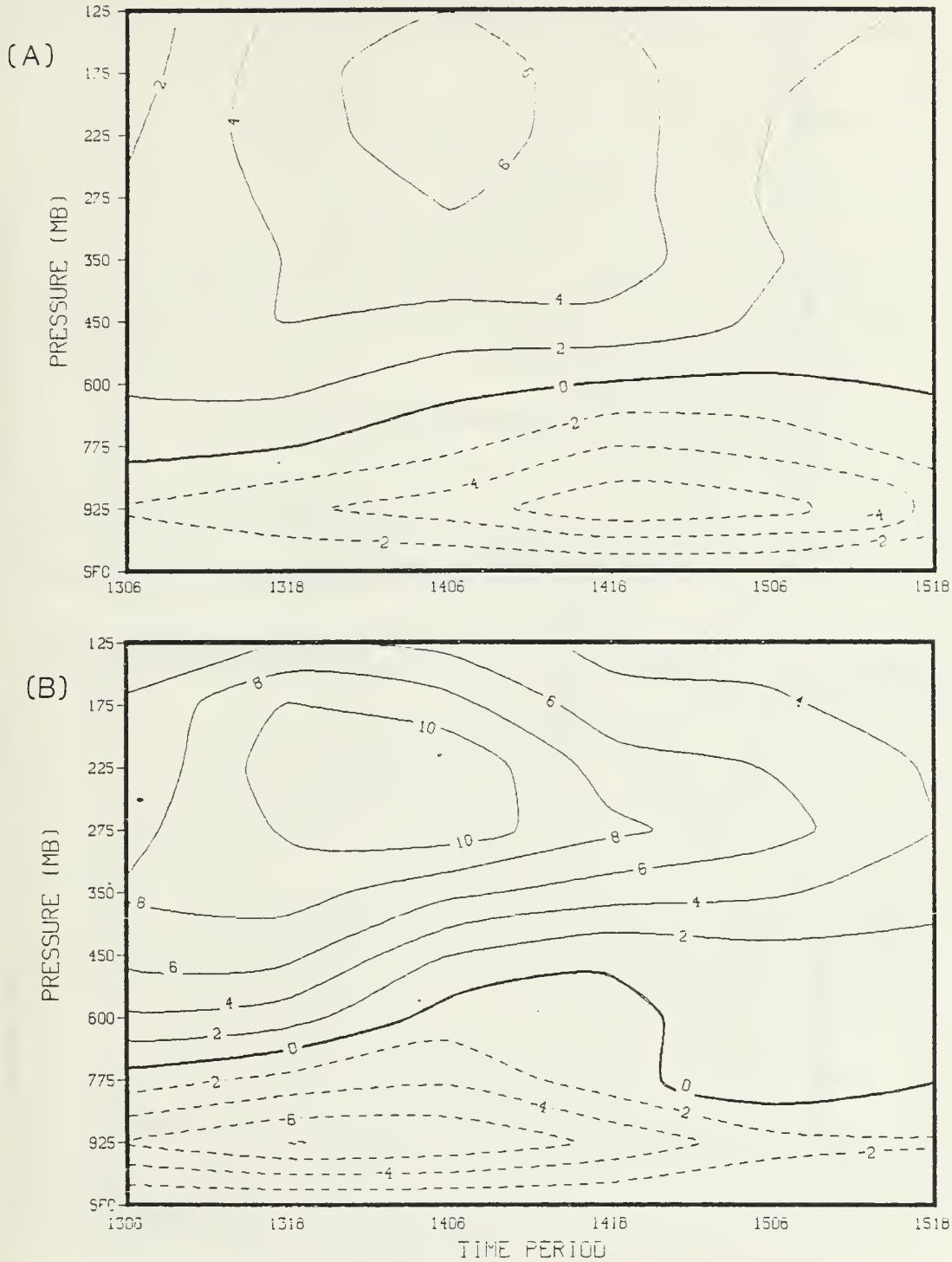

Figure 40. Analyses Lateral Vorticity Advection (A) GLAS (B) ECMWF. As in Figure 34.

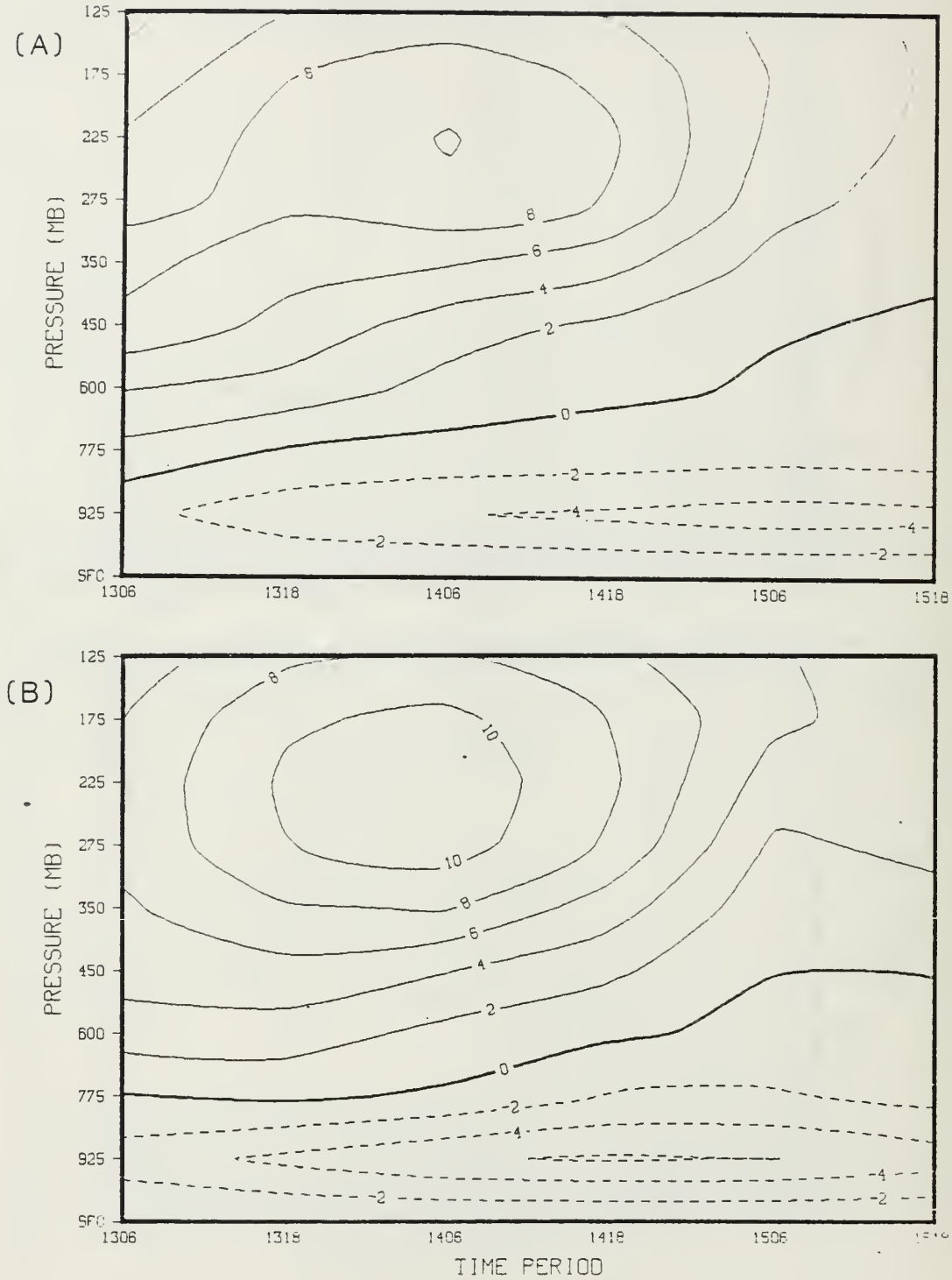

Figure 41. Prognoses Lateral Vorticity Advection (A) SAT (B) NOSAT. As in Figure 34.

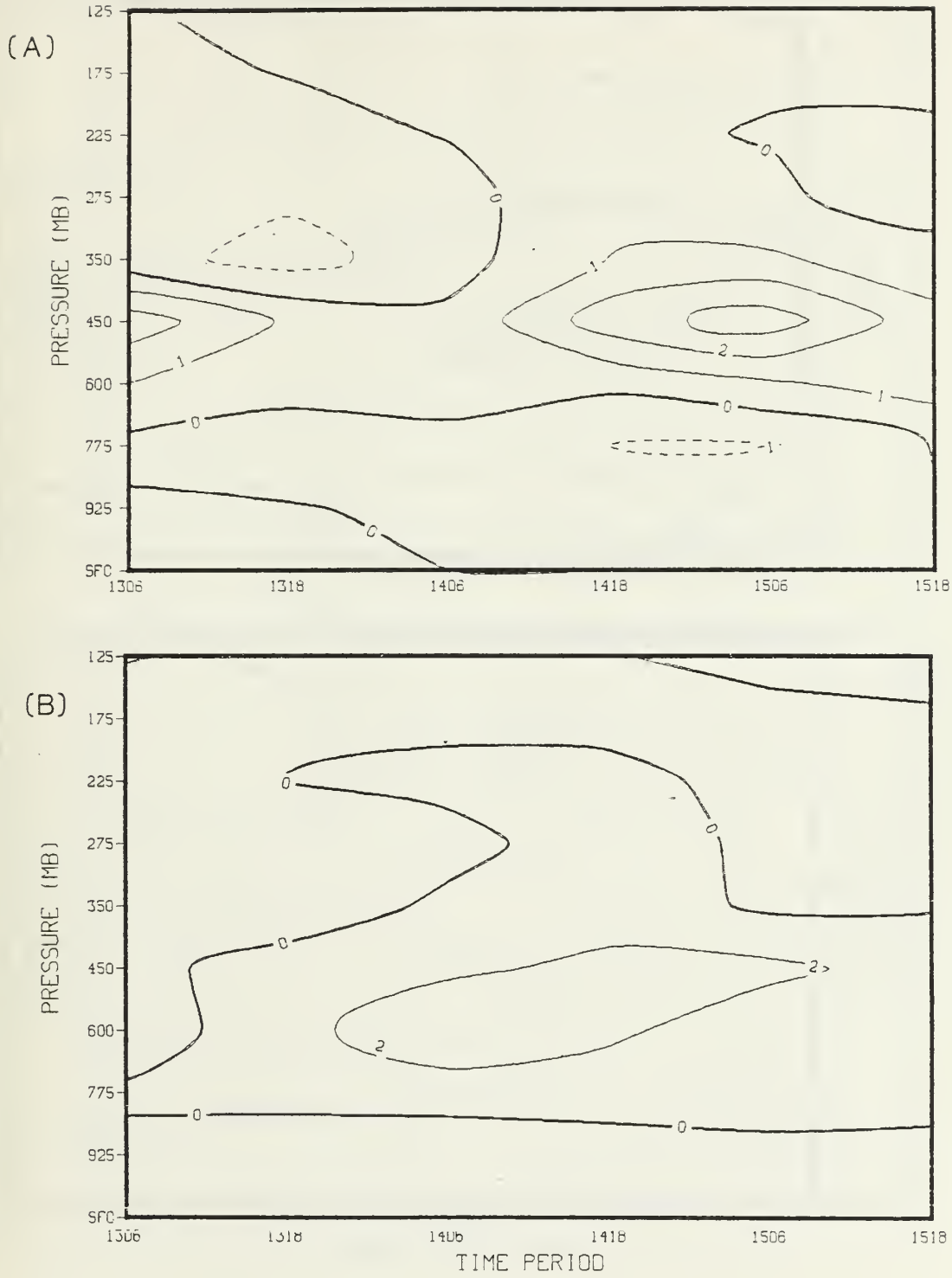

Figure 42. Analyses Vertical Vorticity Advection (A) GLAS (B) ECMWF. As in Figure 34.

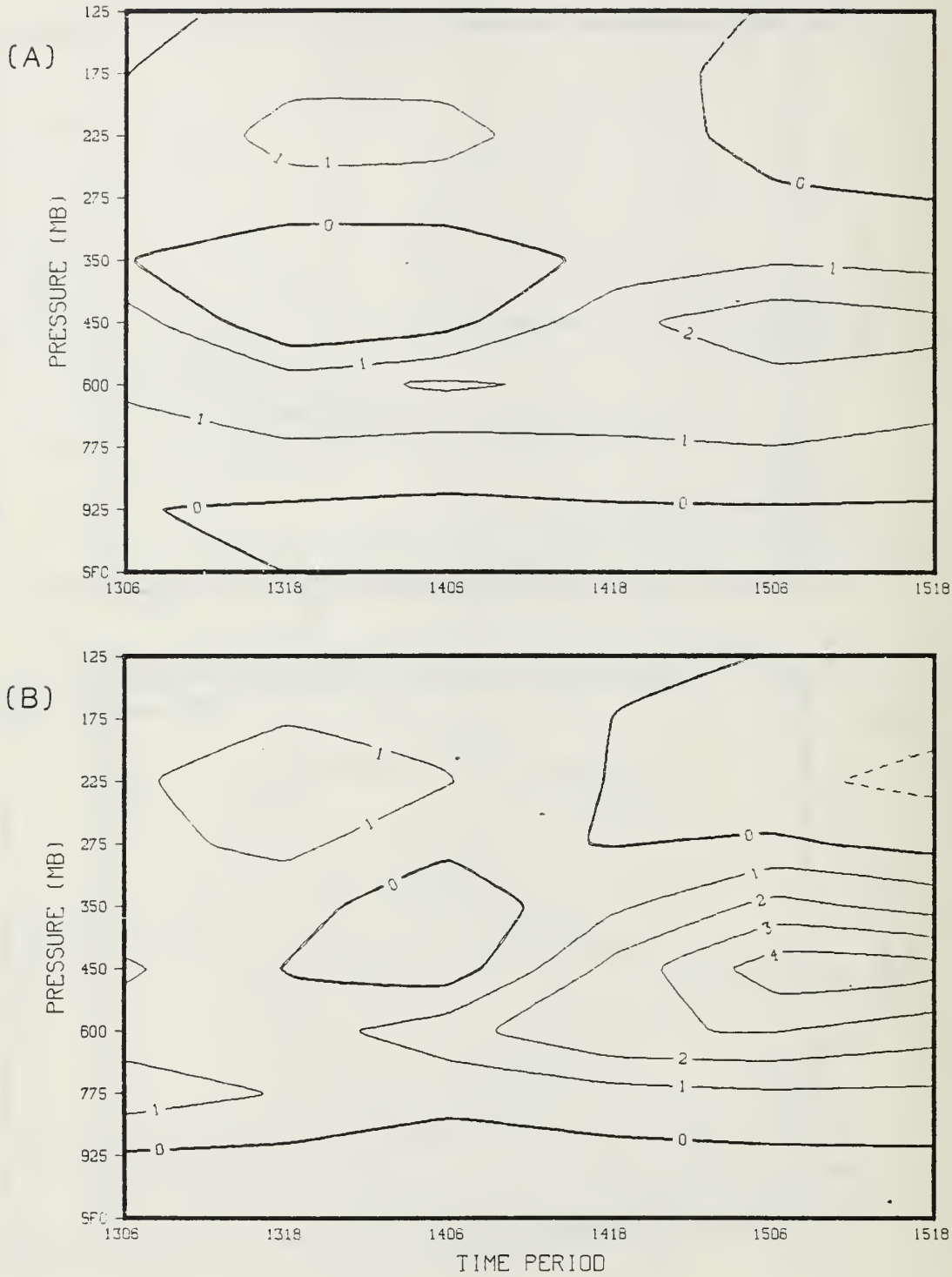

Figure 43. Prognoses Vertical Vorticity Advection (A) SAT (B) NOSAT. As in Figure 34.

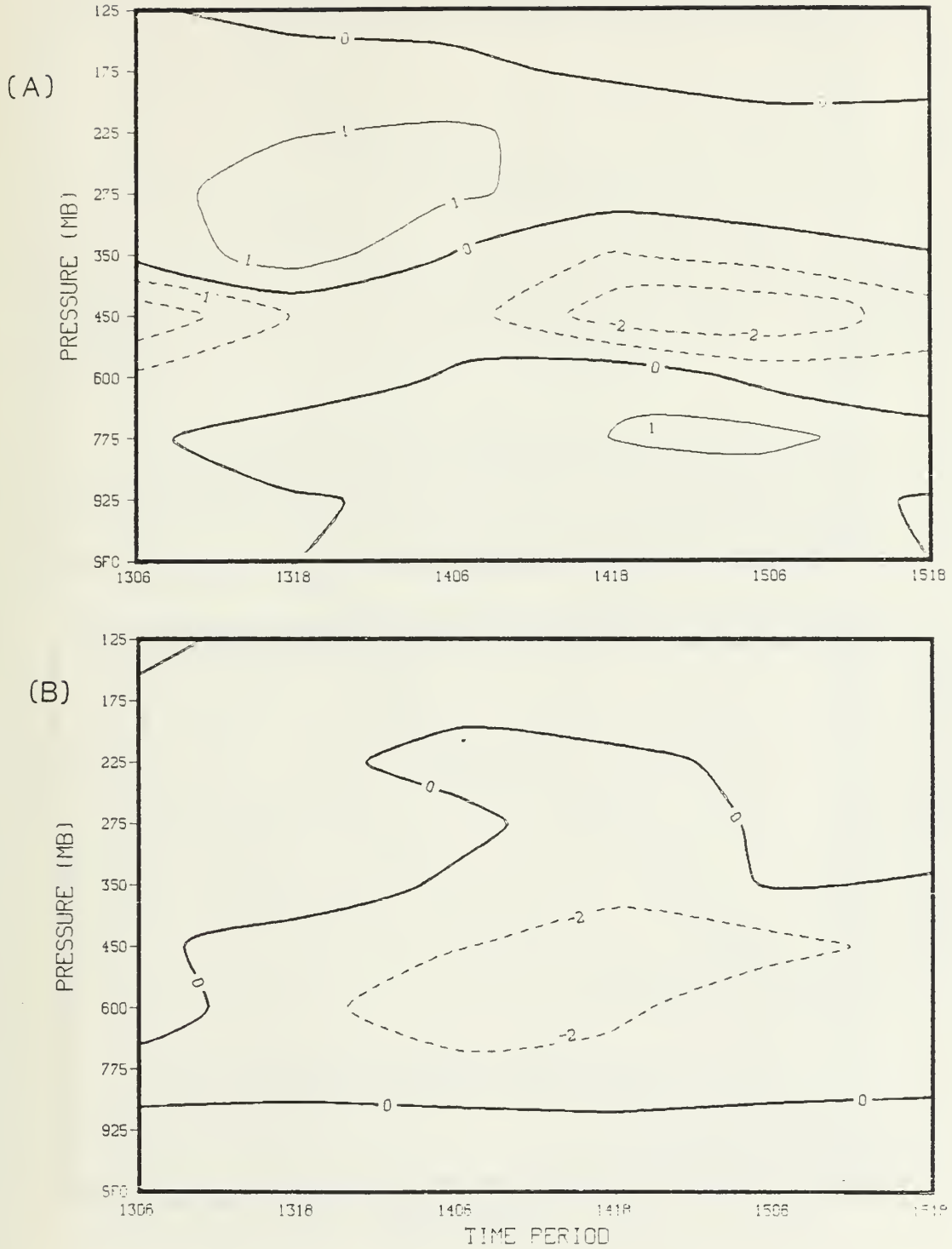

Figure 44. Analyses Tilting Term (A) GLAS (B) ECMWF. As in Figure 34.

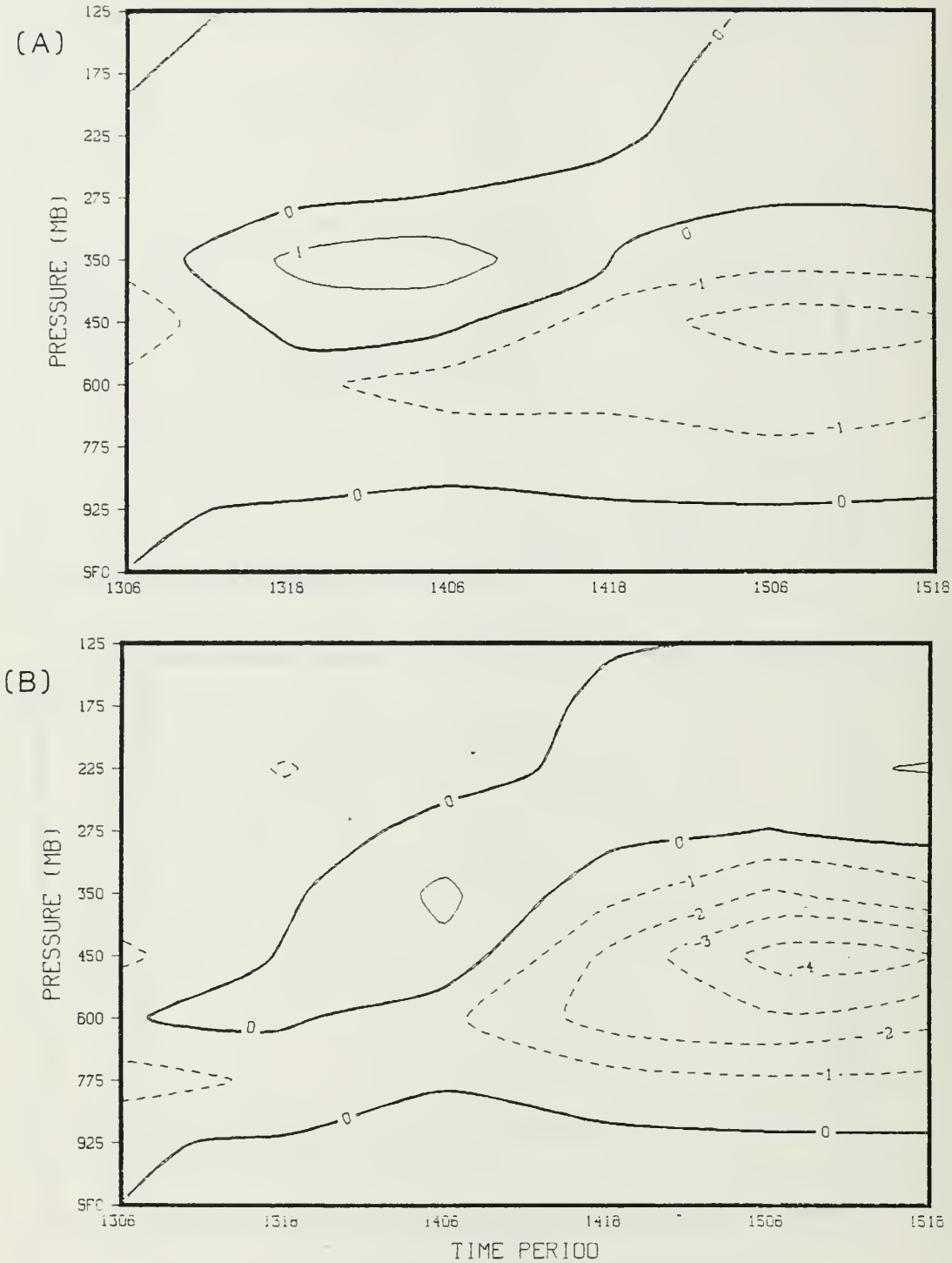

Figure 45. Prognoses Tilting Term (A) SAT (B) NOSAT. As in Figure 34.

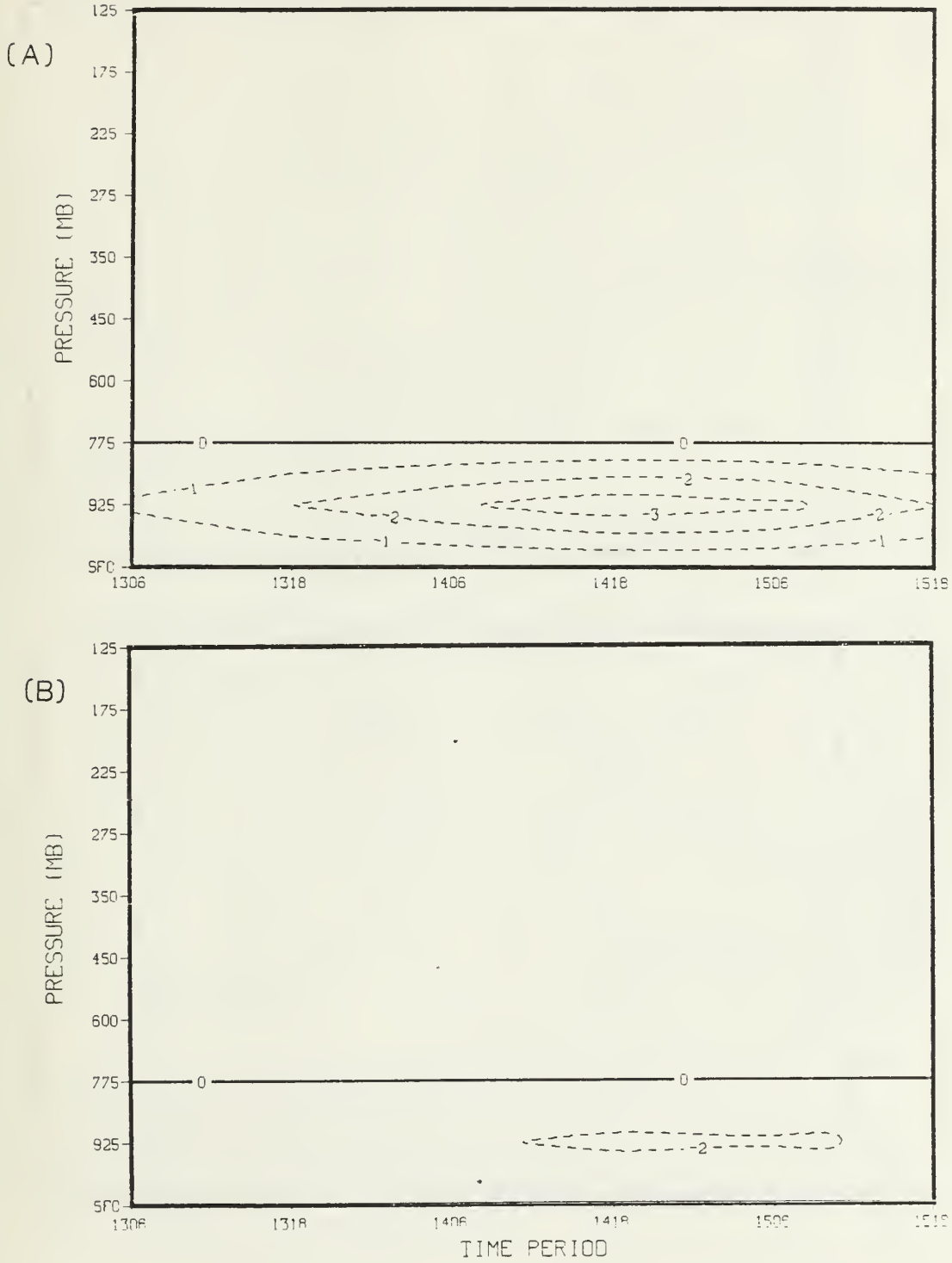

Figure 46. Analyses Frictional Dissipation (A) GLAS (B) ECMWF. As in Figure 34.

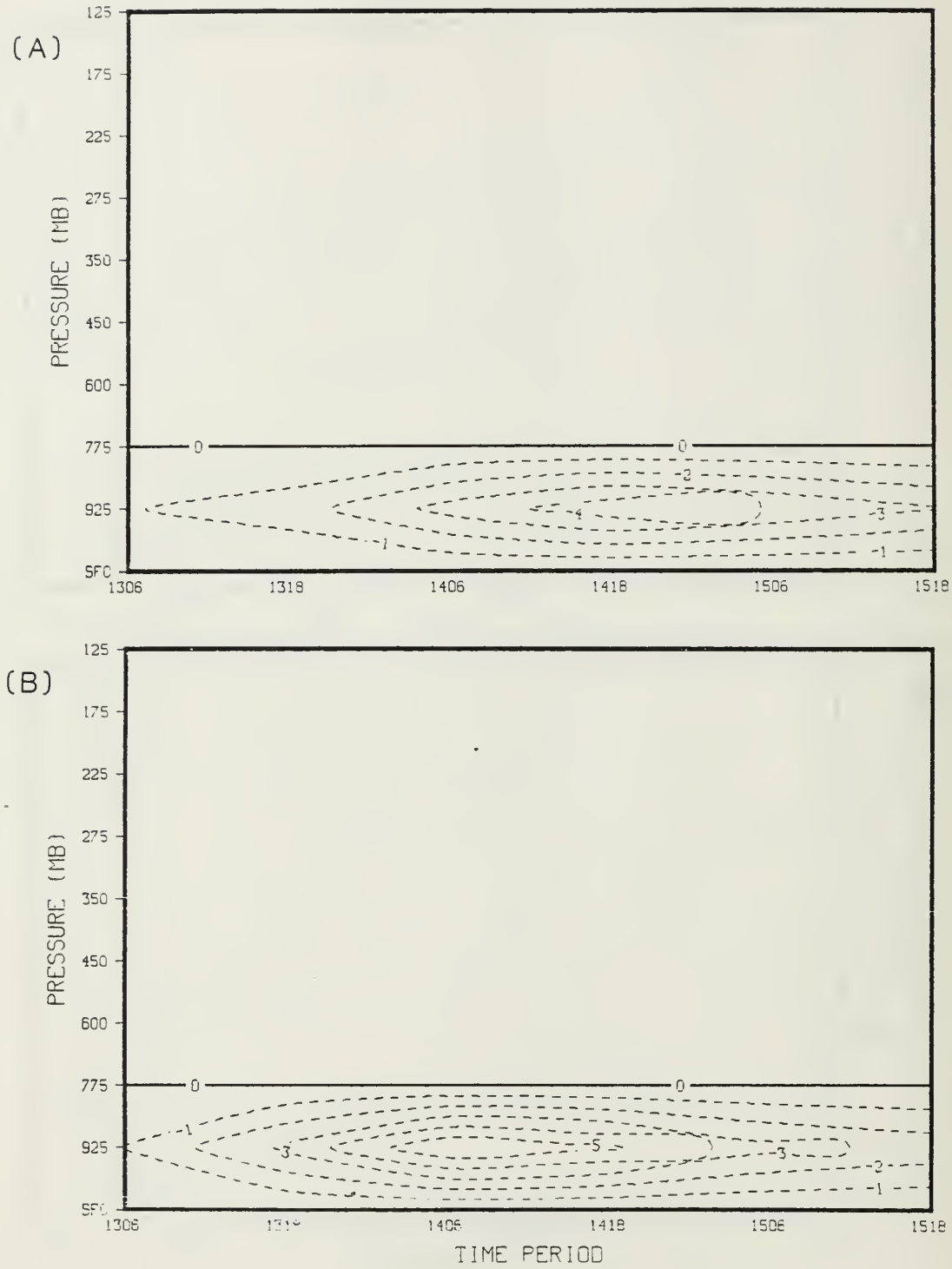

Figure 47. Prognoses Frictional Dissipation. (A) SAT (B) NOSAT. As in Figure 34.

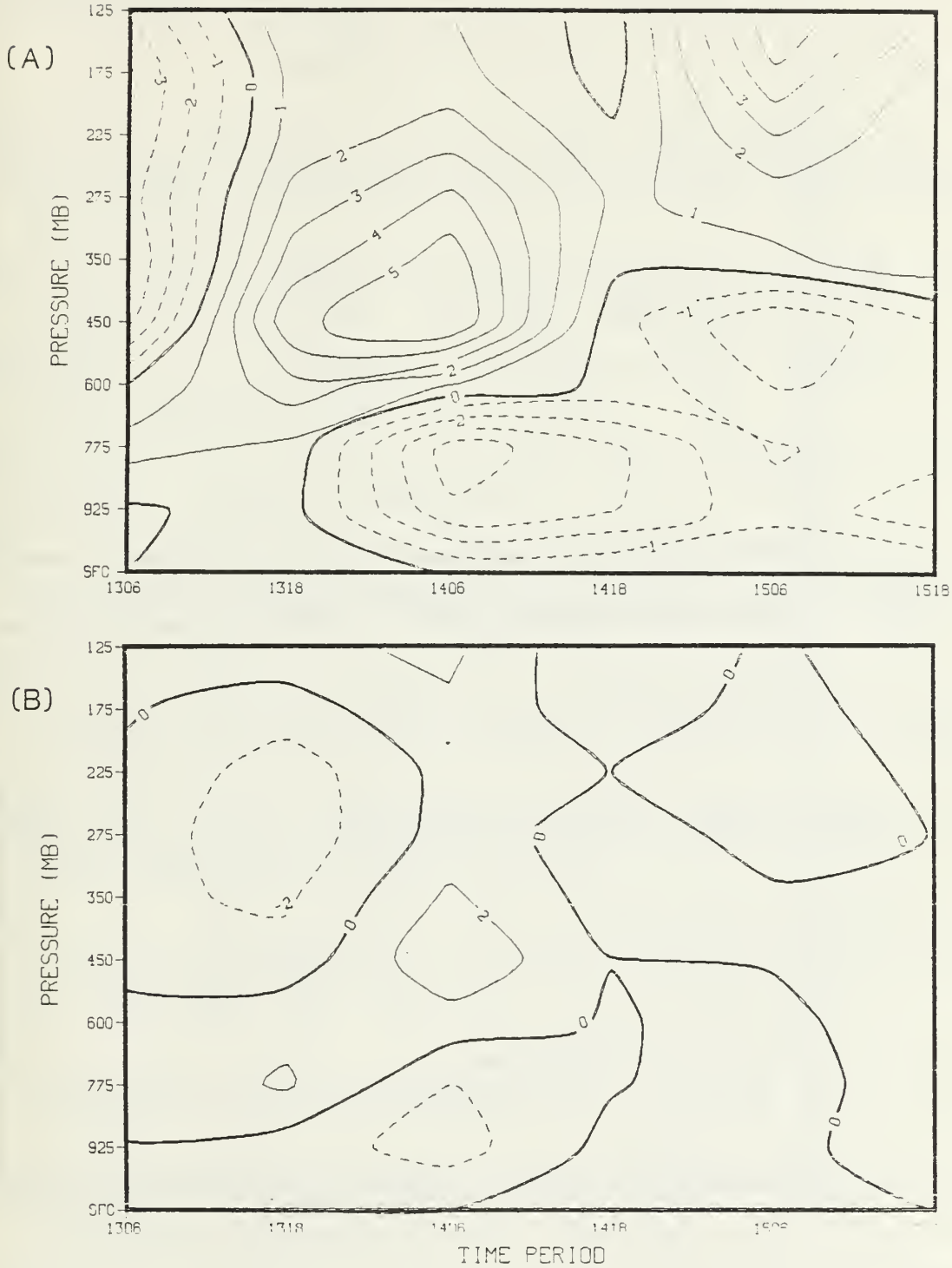

Figure 48. Analyses Budget Residuals (A) GLAS (B) ECMWF. As in Figure 34. Positive Values Indicate Vorticity Excess. Negative Values Indicate Vorticity Deficits.

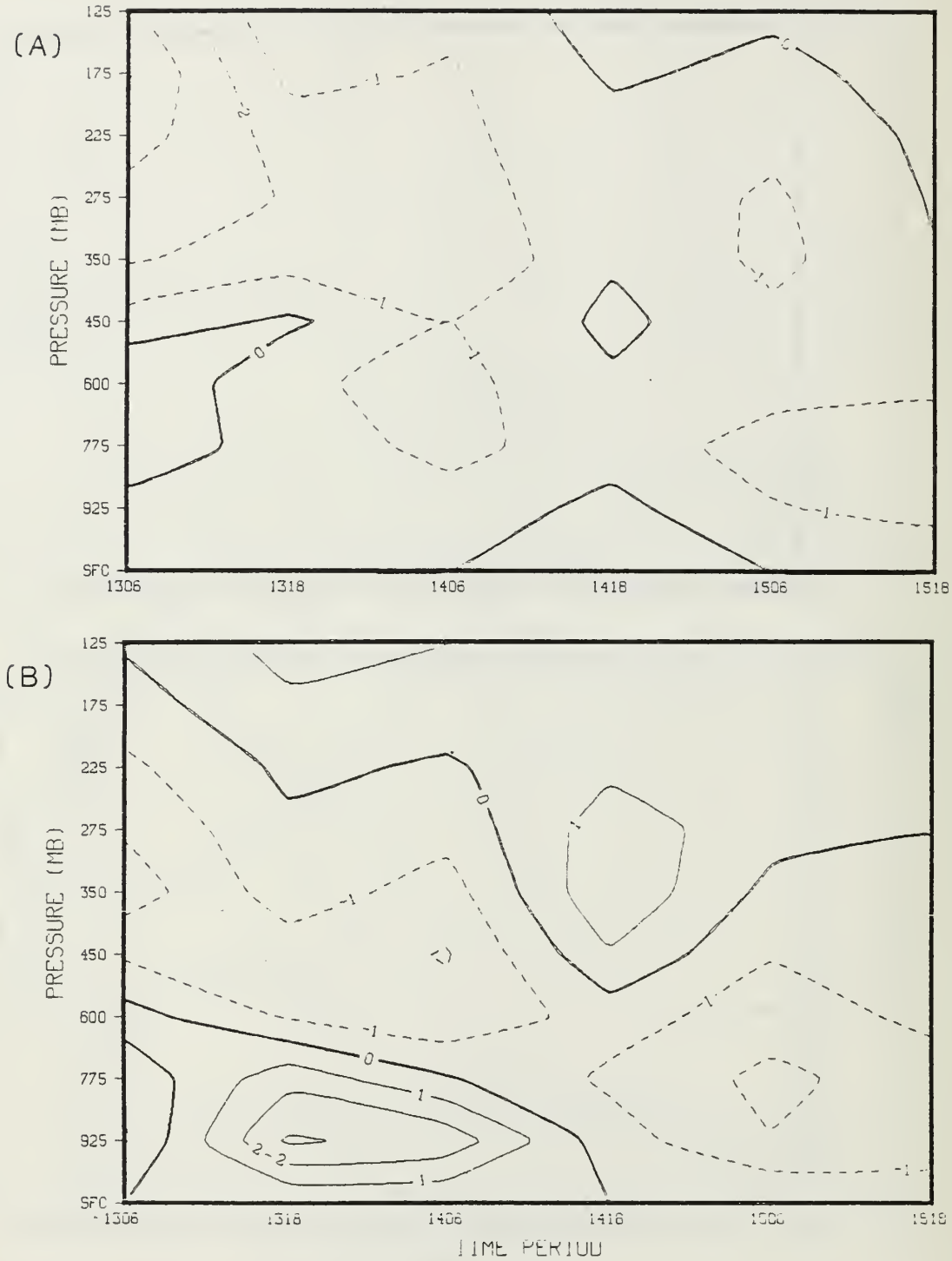

Figure 49. Prognoses Budget Residuals (A) SAT (B) NOSAT. As in Figure 34. Positive Values Indicate Vorticity Excess. Negative Values Indicate Vorticity Deficits.

LIST OF REFERENCES

Baker, W., D. Edelmann, H. Carus, 1981: The GLAS editing procedures for the FGGE level-IIb data collected during SOP-1 and 2. NASA Tech. Memo 83811, Goddard Space Flight Center, 21 pp.

Baker, W.: 1983. Objective analysis and assimilation of observational data from FGGE. Mon. Wea. Rev., 111, 328-342.

Bengtsson, I., M. Kanamitsu, P. Kallberg, and S. Uppala, 1982: FGGE 4-dimensional data assimilation at ECMWF. Bull. Am. Meteor. Soc., 63, 29-43.

Bergthorsson, P., and B. Doos, 1955: Numerical weather map analysis. Tellus, 7, 329-340.

Calland, W.E., 1983: Quasi-Lagrangial Diagnostics Applied to an Extratropical Explosive Cyclogenesis in the North Pacific. M.S. Thesis, Naval Postgraduate School, 153 pp.

Chen, T.J.G. and L.F. Bosart, 1979: A quasi-Lagrangian vorticity budget of composite cyclone-anticyclone couplets accompanying North American polar air outbreaks. J. Atmos. Sci., 185-194.

Conant, P.R., 1982: A Study of East-Coast Cyclogenesis Employing Quasi-Lagrangian Diagnostics. M.S. Thesis, Naval Postgraduate School, 102 pp.

Dimego, G.J. and L.F. Bosart, 1982: The transformation of tropical storm Agnes into an extratropical cyclone. Part II: Moisture, vorticity and kinetic energy budgets. Mon. Wea. Rev., 110, 385-411.

Haltiner, G.J., and R.T. Williams, 1980: Numerical Weather Prediction and Dynamic Meteorology. 2nd ed. John Wiley & Sons, 477 pp.

Johnson, D.R., and W.K. Downey, 1975a: Azimuthally averaged transport and budget equations for storms: quasi-Lagrangian diagnostics 1. Mon. Wea. Rev., 103, 967-979.

Johnson, D.R., and W.K. Downey, 1975b: The absolute angular momentum of storms: quasi-Lagrangian diagnostics 2. Mon. Wea. Rev., 103, 1063-1076.

Johnson, D.R., and W.K. Downey, 1976: The absolute angular momentum of an extratropical cyclone: quasi-Lagrangian diagnostics 3. Mon. Wea. Rev., 104, 3-14.

Kung, E.C., and W.E. Baker, 1975: Energy transformation in middle latitude disturbances. Quart. J. Roy. Meteor. Soc., 101, 793-815.

Lemoyne, J., 1982: The Ocean Ranger's night of death. Newsweek. Nr. 1, 99, 48.

Marine Weather Review, 1979: Mariners Weather Log, 23, No. 2, NOAA, 136-140.

McPherson, R.D., 1984: Cloud-drift wind estimates during FGGE. NMC Office Note 288, National Meteorological Center, 19 pp.

O'Brien, J.J., 1970: Alternative solutions to the classical vertical velocity problem. J. Appl. Meteor., 2, 197-203.

Roman, D., 1981: Application of Quasi-Lagrangian Diagnostics and FGGE Data in a Study of East-coast Cyclogenesis. M.S. Thesis, Naval Postgraduate School, 93 pp.

Sandgathe, S.A., 1981: A Numerical Study of the Role of Air-sea Fluxes in Extratropical Cyclogenesis. Ph. D. Thesis, Department of Meteorology, Naval Postgraduate School, 134 pp.

Sanders, F., and J.R. Gyakum, 1980: Synoptic-dynamic climatology of the "bomb." Mon. Wea. Rev., 108, 1589-1606.

Wash, C.H., 1978: Diagnostics of Observed and Numerically Simulated Extratropical Cyclones. Ph. D. Thesis, Department of Meteorology, University of Wisconsin, 215 pp.

INITIAL DISTRIBUTION LIST

		No. Copies
1.	Defense Technical Information Center Cameron Station Alexandria, Virginia 22314	2
2.	Library, Code 0142 Naval Postgraduate School Monterey, CA 93943	2
3.	Dr. Wayman Baker, Code 911 NASA/GSFC Greenbelt, MD 20771	1
4.	Dr. Robert Curren NASA Headquarters, Independence Avenue Washington, D.C. 20546	1
5.	Meteorology Reference Center, Code 63 Department of Meteorology Naval Postgraduate School Monterey, CA 93943	1
6.	Professor Robert J. Renard, Code 63Rd Chairman, Department of Meteorology Naval Postgraduate School Monterey, CA 93943	1
7.	Professor Christopher N.K. Mooers, Code 68Mr Department of Oceanography Naval Postgraduate School Monterey, CA 93943	1
8.	Professor Carlyle H. Wash, Code 63Cw Department of Meteorology Naval Postgraduate School Monterey, CA 93943	9
9.	Professor Russell L. Elsberry, Code 63Es Department of Meteorology Naval Postgraduate School Monterey, CA 93943	1
10.	Lcdr. Kenneth A. Ebersole 4531 E. Fedora Fresno, CA 93726	1

11. Director 1
Naval Oceanography Division
Naval Observatory
34th and Massachusetts Avenue NW
Washington, DC 20390

12. Commander 1
Naval Oceanography Command
NSTL Station
Bay St. Louis, MS 39522

13. Commanding Officer 1
Naval Oceanographic Office
NSTL Station
Bay St. Louis, MS 39522

14. Commanding Officer 1
Fleet Numerical Oceanography Center
Monterey, CA 93940

15. Commanding Officer 1
Naval Ocean Research and
Development Activity
NSTL Station
Bay St. Louis, MS 39522

16. Commanding Officer 1
Naval Environmental Prediction
Research Facility
Monterey, CA 93940

17. Chairman, Oceanography Department 1
U.S. Naval Academy
Annapolis, MD 21402

18. Chief of Naval Research 1
800 N. Quincy Street
Arlington, VA 22217

19. Office of Naval Research (Code 480) 1
Naval Ocean Research and
Development Activity
NSTL Station
Bay St. Louis, MS 39522

20. Commander 1
Oceanographic Systems Pacific
Box 1390
Pearl Harbor, HI 96860

1 3 3 7 5

211494

Thesis
E1543 Ebersole
c.1 Diagnostic verification of the GLAS general circulation model as applied to a case of extratropical maritime explosive cyclogenesis.

211494

Thesis
E1543 Ebersole
c.1 Diagnostic verification of the GLAS general circulation model as applied to a case of extratropical maritime explosive cyclogenesis.

thesE1543
Diagnostic verification of the GLAS gene
3 2768 001 90293 5
DUDLEY KNOX LIBRARY